2002-01-01

Optical and Magnetic Behaviour of Low Dimensional Structures

Francis Pedreschi
Technological University Dublin

Recommended Citation

Pedreschi, F. (2002). *Optical and magnetic behaviour of low dimensional structures*. Doctoral thesis. Technological University Dublin. doi:10.21427/D7Q60S

Optical and Magnetic Behaviour of Low Dimensional Structures

Francis Pedreschi B.Sc.(App.Sci.)

A thesis submitted to

Dublin Institute of Technology

For the award of

Ph.D.

Supervised by:

Dr J.D. O'Mahony

School of Physics/FOCAS

September 2002

Abstract

Low dimensional structures can exhibit unusual properties due to the quantum confinement of electrons. This may manifest itself in any effects that depend on electron behaviour. In this study, the optical and magnetic properties in particular of two types of low dimensional structures are examined.

Quantum wires are structures that have macroscopic length scales along one dimension and nanometre length scales in the others. Two Indium induced reconstructions of Silicon surfaces were grown and examined to determine if quantum confinement, a necessary requirement for a quantum wire, did exist for their structures. A UHV compatible Reflectance Anisotropy Spectroscopy (RAS) instrument, that measures the difference in reflectivity of linearly polarised light along orthogonal surface directions, was constructed for this purpose. The Si(111)4x1-In and Si(001)4x3-In systems were studied. Studies revealed an optical anisotropy of 1.65% for Si(111)4x1-In which, considering the result is from a layer just a monolayer in thickness, is very high for a metal-semiconductor system and may be indicative of confinement. Si(111)4x3-In revealed a smaller but still considerable anisotropy of 0.5%. The wires were also studied with Scanning Tunnelling Microscopy (STM) in an effort to conclusively determine the structure. The results gave strong evidence in support of the structural model proposed by Bunk, et al. Scanning-tunnelling spectroscopy provided information on surface states which agree qualitatively with photoemission data.

Metallic nanoparticles have been attracting considerable interest due to their novel optical and magnetic properties and as potential components in 'spintronic' devices. Iron and cobalt particles were examined by preparing films on Silicon or Graphite (HOPG) substrates. The films were characterised using Atomic Force Microscopy and STM to determine particle coverage, density and distribution. The particles internal composition was examined using Mössbauer spectroscopy and XPS. The films were then examined using a variation of the RAS technique, Magneto Optical Kerr Effect (MOKE) and its time resolved counterpart TRMOKE. Both give an indication of a materials magnetisation by responding to differences in electron spin population. These results were compared to those obtained from SQUID magnetometry. It seems that for monolayers of particles in this size regime, i.e.

~10nm, the optical techniques do not have the required sensitivity to detect a magnetic response, despite their surface specificity. Hence the results at least help to place a lower limit on the techniques' sensitivity. Iron particles were also examined using Magnetic Force Microscopy, which demonstrated a stronger response over a single particle than a particle cluster. A computational model was generated to explain this interesting effect. This verified the hypothesis that dipolar interactions between the neighbouring particles in a cluster were sufficiently strong to prevent the tip from aligning the particles magnetic moments. In the absence of these interactions, as is the case with an isolated particle, the tip can align the moment.

Declaration

I certify that this thesis which I now submit for examination for the award of Ph.D., is entirely my own work and has not been taken from the work of others save and to the extent that such work has been cited and acknowledged within the text of my work.

This thesis was prepared according to the regulations for postgraduate study by research of the Dublin Institute of Technology and has not been submitted in whole or in part for an award in any other Institute or University.

The Institute has permission to keep, to lend or to copy this thesis in whole or in part, on condition that any such use of the material of the thesis be duly acknowledged.

Signature _____

Date _____

Acknowledgements

Sincerest thanks to my supervisor Des O'Mahony, for his interest in and help throughout the project. Thanks are also due to DIT, FOCAS and Enterprise Ireland for funding this project.

Thanks are also due to the following people from the various institutes and groups I have been privileged to work with during this thesis:

Sandhya Chandola, John McGilp and Joe McCauley, from Trinity College Dublin, for support and equipment for the RAS experiments.

John Power, Peter Weightman, Ben Sheridan and Paul Unsworth, at the IRCSS in Liverpool, provided facilities to perform the initial RAS experiments in '98 and '99 and were available with help and ideas during both visits.

Tony Cafolla and Darren Carty, Dublin City University, made their STM available for the In-Si experiments and worked very unsociable hours to keep the instrument in top condition.

Kees Flipse, Paul Koller, Georghi (George) Tanasa, Jason Jennette, Oleg Kurnosikov, Bert Koopmans, Bart Smits, Kin Ha, Maarten van Kampen, Csaba Josza, Dominic Bruls, Jurgen Kohlhepp, Paul Koenraad and Coen Swüste, from Technische Universiteit Eindhoven, who assisted both in performing experiments and analysing results for the magnetic nanoparticle experiments. The Mössbauer Group at the Interfaculty Reactor Institute from Technische Universiteit Delft, for performing the Mössbauer experiments. Thanks also to Karen Butter, from Utrecht, who made the colloidal iron particles as part of her PhD work.

Thanks to S. Sun and C. Murray from the Thomas J. Watson Research Centre for supplying the cobalt nanoparticle samples.

The technical staff in DIT, especially James Callis and Joe Keogh, provided invaluable help with equipment and (numerous) IT and electronics problems.

Thanks additionally to Feidhlim, Gordon, Alan, Caroline, Jennifer, Eamonn and Alan in DIT and Jean Michel and Juan in TUE for all the help and social occasions going back many years.

Finally, thanks to anyone else who helped in any way, however large or small, to Sarah and to my family for all of their help and support.

Table of Acronyms.

AFM	Atomic Force Microscopy
ARPES	Angle Resolved Photo-Emission Spectroscopy
CDW	Charge Density Wave
CLPS	Core Level Photoelectron Spectroscopy
HOPG	Highly Ordered Pyrolytic Graphite
HREELS	High Resolution Electron Energy Loss Spectroscopy
ICISS	Impact Collision Ion Scattering Spectroscopy
IPES	Inverse Photo-Emission Spectroscopy
LDOS	Local Density of States
LEED	Low Energy Electron Diffraction
MFM	Magnetic Force Microscopy
MOKE	Magneto-Optical Kerr Effect
PAC	Perturbed $\gamma\gamma$ Angular Correlation
PEM	Photoelastic Modulator
PMT	PhotoMultiplier Tube
RAS	Reflectance Anisotropy Spectroscopy
RHEED	Reflection High Energy Electron Diffraction.
SQUID	Superconducting Quantum Interference Device
STM	Scanning Tunnelling Microscopy
STS	Scanning Tunnelling Spectroscopy
SXRD	Surface X-Ray Diffraction
TRMOKE	Time Resolved Magneto-Optical Kerr Effect
XPS	X-Ray Photoelectron Spectroscopy
XRD	X-Ray Diffraction

Contents

Appendices

Chapter 1

Introduction

1.1 Low Dimensional Systems

Solid state physics research has become increasingly interested in the area of low dimensional physics.[1] On nanometre dimension scales unusual changes or enhancements in a material's properties can be observed,[2,3] and these can be controlled to degrees not possible before. This makes them suitable for inclusion in the production of electronic devices. The importance of surface effects in device performance has long been realised, and the control of device properties is normally achieved here by the adsorption of different materials onto the surface, in addition to doping the bulk material with impurities. However, while this allows a measure of property control it does not unlock the potential of fully customisable materials.

The possibility of developing tailor-made materials may be achievable through the use of low dimensional systems. The unusual properties of such systems arise due to the dominance of surface effects and especially due to quantum confinement effects.[4,5,6] By varying structure sizes, it is possible to control the density of states of such materials, giving more control over their behaviour.

An example of a device that makes use of quantum confinement is the quantum cascade (QC) laser,[7] a system consisting of arrays of 2 dimensional quantum wells. The energy levels of the lasing system can be varied by changing the thickness of the quantum wells, and the levels have less dispersion than those of bulk materials. This results in a laser whose output frequency can be tailored to a required value and at the same time produces optical power more efficiently than a conventional semiconductor laser. Advances in manufacturing techniques have made it easier to study these systems and have increased their technological relevance.

To further investigate the unusual behaviour of these types of materials, this work examines two classes of low dimensional structure:

(i) Quantum wires, which are quasi one-dimensional structures that allow free electron motion along the macroscopic dimension which may extend for microns, but confines them in a potential barrier along the quantum scale dimensions, which are on the nanometre scale. These are increasingly relevant to the semiconductor industry due to improvements in lithography technology, which will see the production of devices using 90nm processes in 2003 and further reductions thereafter.

(ii) Quantum dots. These are quasi-zero-dimensional structures with length scale on the nanometre range in all dimensions. They can represent a state of matter between bulk and atomic, the degree of which will depend on the particle size, and can exhibit many unusual properties. They have potential for use as high density magnetic storage devices and as prototype components for quantum computers.

These systems will now be described in greater detail.

1.2 Quantum Wires: One-Dimensional Structures.

Quantum wires are quasi one-dimensional metallic structures, resembling conventional wires in structure but with lateral wire dimensions on a nanometre scale. A team led by B.J. van Wees at Philips Research Laboratories, Eindhoven, and T.U. Delft in the Netherlands produced one of the first effective quantum wire systems in 1988.[8]

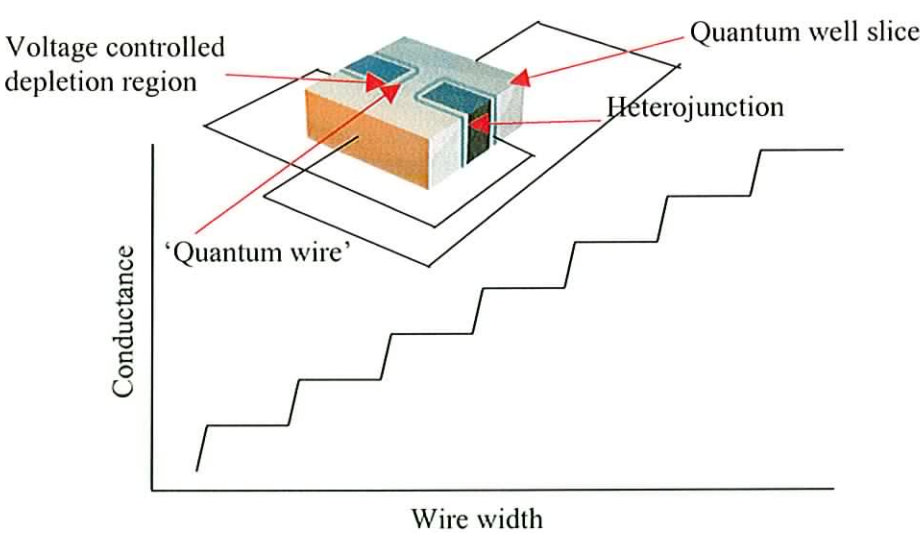

Figure 1.1: Representation of the van Wees, et. al., experiment showing quantised conductance.

This involved creating the heterojunction structure shown in figure 1.1, and using a voltage to control a depletion region, similar to the action of a Field Effect Transistor (FET).

By varying the voltage, they could control the width of the wire, or 'Split Gate', as it was called. Some unusual behaviour was found, the primary being the fact that the conductance was quantised, depending on the width of the wire. This is shown in figure 1.1 This behaviour was explained by Rolf Landauer of IBM's Thomas J. Watson research centre in terms of a quantum confinement model, where the width of the wire has to support half wavelength multiples of the electron wavelength.[9]

Despite this success, effective quantum wire systems have been difficult to create. One of the primary requirements is that the electrons are confined to the wire and cannot tunnel into adjacent structures. Although structurally similar to quantum wells, it seems that this quantum confinement is more difficult to attain in these systems. Two categories of wire have been tried as shown in figure 1.2: the nanocontact type, which is formed by stretching a neck formed between two touching materials, or a deposition type, which may be formed using standard surface processing techniques.

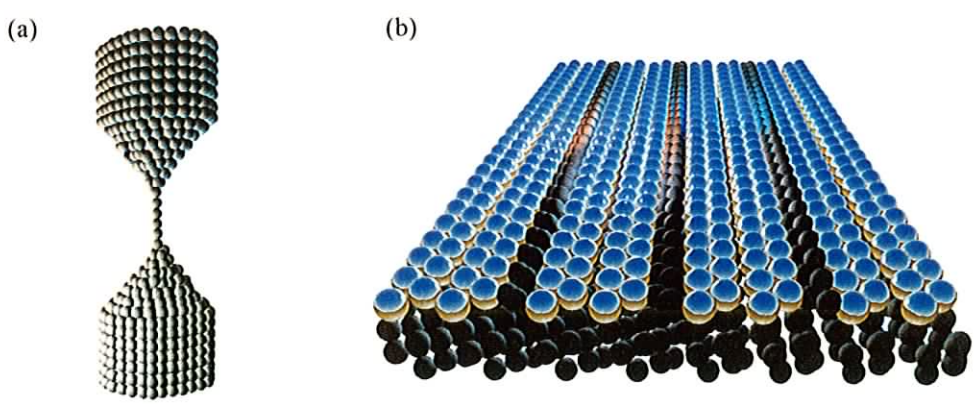

Figure 1.2: Representation of two types of quantum wire structure, (a) nanocontact and (b) deposition type.

In nanocontact wires confinement is not normally problematical due to the presence of an effective vacuum at the surface. For arrays on surfaces or buried structures, materials with specific bandgaps between the conduction and valence bands, normally larger than that of the wire material, are required to create an effective confining potential. The carrier density in the wires also needs to be kept

relatively low so that the electrons occupy states which are low in energy compared to the confining potential: this reduces the probability of tunnelling between wires. As well as having adequate lateral confinement, a quantum wire must also be metallic. This can also cause difficulties, because 1-D systems tend to undergo a reorganisation known as the Peierls distortion,[10,11] which is caused by thermally induced fluctuations of the atoms or molecules positions. This can take one of two forms:

(i) Positional, where alternate atoms or molecules in the chain are displaced without rotation from their equilibrium positions, figure 1.3. This causes a modification of the transfer integral that causes a gap in the band at the Fermi level.

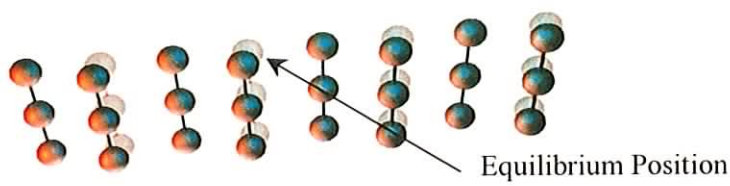

Figure 1.3: An example of the positional Peierls instability. Equilibrium position is shown semi-transparent.

(ii) Orientational, where alternate molecules in an array of centrosymmetric molecules may rotate to different orientation but their centres remain fixed, figure 1.4. This does not modify the transfer integral but the change in symmetry means that the alternate molecules no longer necessarily have the same energy levels. A band gap at the Fermi level may also arise due to this effect.

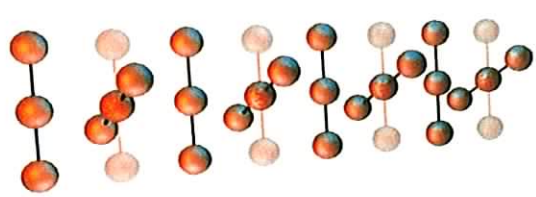

Figure 1.4: Examples of the orientational Peierls instability, which shows molecules rotated from their equilibrium positions.

These band gaps can make naturally occurring 1-D metallic systems hard to find.

Aside from the scientific interest in quantum wire systems, they are also important to the microchip fabrication industry. Current technology is progressing towards and beyond 90nm technology. This is normally the size of the interconnecting wires, rather than the transistors themselves. An example of such a structure is shown in figure 1.5. If these devices continue to shrink, and the industry is determined that they will,[12] the ultimate evolution will be molecular electronics, and if the device density that such structures will allow is to be obtained, the interconnects between molecular transistors will have to be of quantum wire dimensions. This will involve arrays of parallel quantum conductors, and the difficulties of inhibiting tunnelling between wires, longer range Coulomb drag interactions and operation using low carrier densities will have to be overcome.

For this study deposition type wires were used. Specifically, the deposition of Indium onto Silicon (111) substrates has been shown to generate wire like structures that are visible on STM images.[13] Due to the narrow dimensions (<2nm) of these structures they are potential candidate quantum wire structures. Because of their small size the wires are sensitive to atmospheric contaminants and are produced under UHV conditions and are not stable in air, even after the manufacturing process is complete.

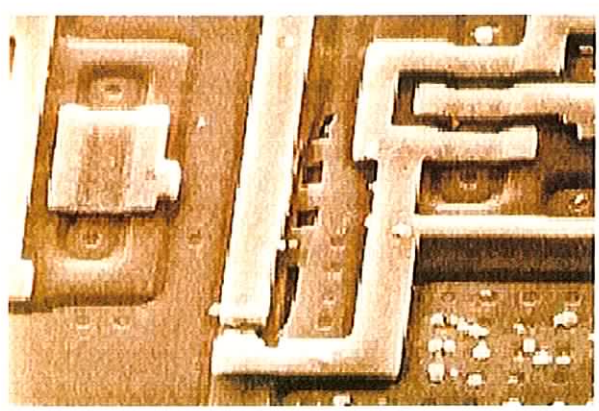

Figure 1.5: Image of a microchip produced by lithography. The smallest feature, i.e. wire width, is approximately 130nm in current manufacturing processes.[14]

1.3 Quantum Dots: Zero-Dimensional Nanoparticles

Quasi zero dimensional structures consist of nanometre sized clusters of material.[15] They may be created in a variety of ways, such as forcing the controlled growth of islands on a surface or in colloidal reaction chambers.

They may in the simplest case be approximated by the quantum mechanical particle in a 3-D box problem, and the energy of supported electron states can be varied by changing the particle sizes. The states themselves are also quite narrow. Because of this, they are sometimes referred to as artificial atoms. They have been investigated for use in magnetic, optical and spin electronic ('spintronic') devices, although they have fallen somewhat out of favour for the latter cause, due to the manufacturing difficulties in generating large patterned structures.[16] As low volume test systems and research tools though, they are still extremely valuable. Figure 1.6 shows well ordered hexagonal lattices of cobalt particles.[17]

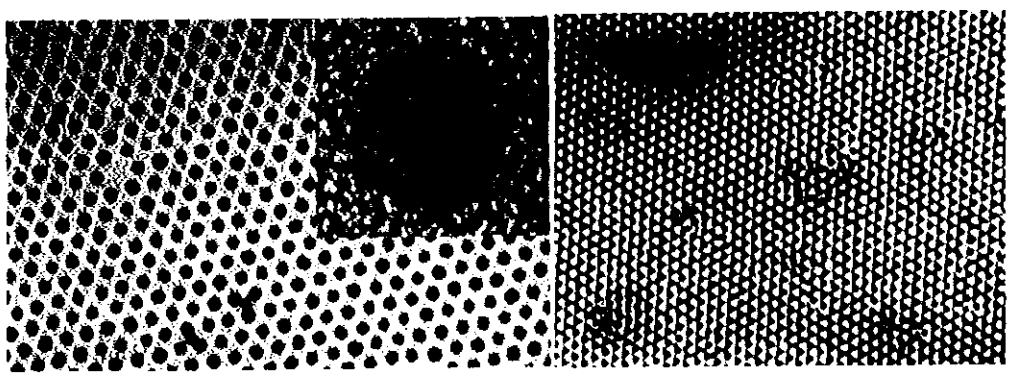

Figure 1.6: TEM images of 10nm diameter cobalt nanoparticles[17] (a) A 2D film (b) A 3d superlattice.

This work concentrates on the magnetic properties of these structures. They can exhibit enhanced magnetism relative to a bulk sample, due to the greater proportion of surface atoms.[18] This results in reduced quenching of the orbital and spin contributions to the angular momentum. This makes them potentially very useful to the magnetic storage industry.[19] A representation of a permanent magnetic storage system is shown in figure 1.7. There are problems though. Due to the small size of the particles, the lifetime during which the moment will remain pinned to a particular orientation can be quite short. In the extreme limit the reduced anisotropy barrier in the material and the absence of domain walls can lead to superparamagnetism, which means that the magnetic moment of the particle is excited into a randomly fluctuating orientation by thermal energy and cannot easily be pinned in one direction.

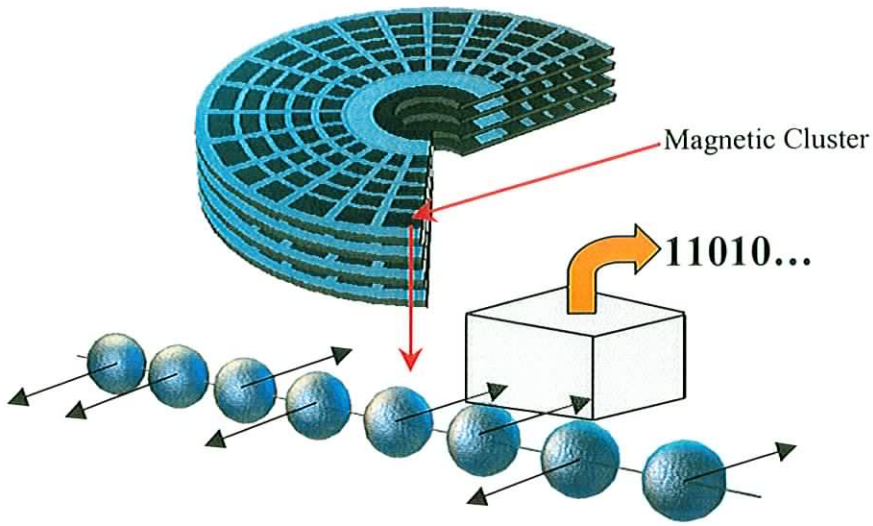

Figure 1.7: A representation of magnetic clusters on a hard disk platter.

It is anticipated by IBM that barring a technology breakthrough this 'superparamagnetic limit' will be reached in commercial storage devices in 2003-2004.[19] This gives the investigations of magnetic particles great relevancy if it is not to become a serious technological and industrial impediment.

An ability to pin the magnetic moment is not the only important consideration. The time it takes for the moment to settle into a new state after it has been forced from one orientation to another is also vital, as this determines the speed of the system. This is important for conventional magnetic storage and for other fast non volatile storage systems that use magnetic effects, such as Magnetic RAM. It is also of considerable scientific interest, as ultra-fast electronic transitions are not well understood and can be quite difficult to probe.

Iron and cobalt particles were used in this study, because the particles are magnetic and were readily available. The iron particles were approximately 10.6nm in diameter and were obtained in solution from the University of Utrecht. They could then be deposited onto substrates for further study. The cobalt particles were obtained from IBM and were already deposited onto HOPG substrates.

1.4 This Thesis.

Optical probes form the centrepiece of this investigation. Three techniques which are broadly similar in experimental configuration can be used to probe all of the effects central to this work, i.e. quantum confinement, and static and dynamic

magnetism. The degree to which a system has quantum confinement may manifest itself in its optical response, if the effect is large enough (or the instrument sensitive enough). A polarised light probe is an obvious candidate for this task, as it should allow directional probing of a material. For this purpose, a Reflectance Anisotropy Spectrometer was constructed. First developed by Aspnes and Studna[20] as a reflection difference technique, it measures the difference in reflectance of two states of near normal incidence linearly polarised light from a surface, which are 90^0 apart in rotation. By aligning the probe axes with the quantum wires, it should be possible to detect differences in reflectance parallel and perpendicular to the wires. The more confined the electrons are in the wires, the greater the reflectance differences that would be expected. Although it would be difficult to find a quantitative relationship between the reflectance and the confinement, RAS has the potential to perform fast investigations of candidate systems, which can then be probed in more detail using other techniques.

The magnetic behaviour of nanoparticles can be probed using a variety of techniques, including Magneto Optical Kerr Effect magnetometry, Time Resolved MOKE, Magnetic Force Microscopy and SQUID magnetometry. MOKE can be constructed by a relatively simple modification of the RA spectrometer and probes a material's magnetisation by measuring the optical response of the uneven electron spin distribution that would be found in a magnetised material. This can examine the time averaged magnetic properties of structures down to a micron in size, depending on light spot focusing. TRMOKE is constructed by changing the optical probe to an ultrafast pulsed laser and by modifying the optical path time dependent information can be obtained. It is a relatively new technique that has yielded some exciting results recently. Collectively they can yield a variety of information about a system.

These techniques were applied, where relevant, to the one- and two- dimensional systems. The 'wires' were studied with STM, to determine structural information, STS to examine energy levels and RAS to investigate the degree of electron confinement. The nanoparticles were studied with Mössbauer spectroscopy and XPS to investigate chemical composition, AFM for information on the particles' assembly into lattices after deposition onto substrates and MOKE, TRMOKE, SQUID and MFM for magnetic properties.

1.5 References

[1] C. Weisbuch, B. Vinter, *Quantum Semiconductor Structures* (Academic Press, Boston, 1991).

[2] e.g. W. P. Halperin, Rev Mod Phys, **58**, 3, (1986)

[3] S. Ciraci, Inder P. Batra, Phys. Rev. B., **33**, 4294, (1986)

[4] T. Wang, T. H. Hsleh, T. W. Chen, J. Appl. Phys., **74**, 1, (1993)

[5] T. Takgahara, K. Takeda, Phys.Rev. B, **46**, 15578, (1992)

[6] J. B. Xia, K. W. Cheah, Phys. Rev. B, **55**, 15668, (1997)

[7] J. Faist, F. Capasso, C. Sirtori, D.L. Sivco, J.N. Baillargeon, A.L. Hutchinson, S.N.G. Chu, A.Y. Cho, Appl. Phys. Lett, **68** 3680 (1996)

[8] B. J. van Wees, H. van Houten, C. W. J. Beenakker, J. G. Williamson, L. P. Kouwenhoven, D. van der Marel, C. T. Foxton, Phys. Rev. Lett, **60**, 848, (1988)

[9] R Landauer, Philos. Mag. **21**, 863, (1970)

[10] L. D. Landau, in *Collected Papers of L. D. Landau* (ed. D. ter Haar) 193–216 (Gordon & Breach, New York, 1965).

[11] R. E. Peierls, *Helv. Phys. Acta Suppl.* 7, S81–S83 (1934).

[12] G. E. Moore, Electronics, **38**, Number 8, 1965

[13] e.g. J. L. Stevens, M.S. Worthington, I, S. T. Tsong, Phys. Rev. B, 47, 1453, (1993)

[14] G. Stinson, B, Magluyan, *Application of Automatic Defect Classification in Photolithography*, Yield management solutions, (2000)

[15] T. Chakraborty, *Quantum Dots : A Survey of the Properties of Artificial Atoms*, 1st ed., Elsevier Science Ltd, 1999

[16] E. Corcoran, G. Zorpette, Scientific American, Special Issue 'The Solid State Century',August 1997, www.sciam.com/specialissues/1097solidstate/1097corcoran.html

[17] S. Sun, C.B. Murray, J. App. Phys., **85**, 4325, (1999)

[18] H. A. Dürr, S. S. Dhesi, E. Dudzik, D. Knabben, G. van der Laan, J. B. Goedkoep, F. U. Hillebrecht, Phys. Rev. B., **59**, R701, (1999)

[19] e.g. http://www.research.ibm.com/journal/rd/443/thompson.html

[20] D. E Aspnes, A. A. Studna, Phys. Rev. Lett. 54 1956 (1985)

Chapter 2

A Brief Introduction to RAS Theory.

This chapter will examine the theoretical background to the RAS technique that is necessary for its successful implementation. It will be developed with respect to the general optical response of a surface. The next chapter will describe the application of this to a practical instrument.

2.1 Surface Optical Response: Interaction of Matter and Light

The optical response of a material refers to the way that it interacts with electromagnetic radiation, and the information that may be obtained by analysing the light after the interaction has taken place. In relation to this work, the surface optical response refers to the behaviour of light after reflection from the surface. Detailed descriptions of reflectance theory and optical responses can be found elsewhere.[1,2,3] The following is a brief summary.

In general, an electromagnetic wave will cause dipoles in any material it interacts with to oscillate. If the electromagnetic wave has angular frequency ω and wavevector **k** then the electric field associated with it can be described by **E**(**k**,ω) and the materials response may be referred to as an oscillating polarisation field, P(ω, 2ω,...) which is described by the following equation

$$\mathbf{P}(\mathbf{k},\omega,2\omega,...) = \varepsilon_0\left[\chi^{(1)}(\mathbf{k},\omega).\mathbf{E}(\mathbf{k},\omega) + \chi^{(2)}(\mathbf{k},\omega,2\omega)\mathbf{E}(\mathbf{k},\omega)\mathbf{E}(\mathbf{k},\omega) + ...\right] \qquad \text{Eq. 2.1}$$

where $\chi^{(i)}$ is the *i*th-order dielectric susceptibility tensor, which describes the material's tendency to polarise in, or its degree of reaction to, the presence of an electric field. Despite the largely monochromatic nature of the incident light, higher harmonics are present in the polarisation field. These are caused by finite photon length, lattice imperfections and other symmetry disruptions that remove isotropy, and

physically represented by χ^n, where n>1, resulting in harmonics of nω. The oscillating dipole will also re-emit light, and this will carry information on the distortions that took place. RAS is a linear techniques, however, and is only concerned with $\chi^{(1)}$, and the higher harmonics can be ignored, as normally, $\chi^1 >> \chi^n$, n>1 if the incident intensity is low, as it is with RAS.

2.2 RAS

RAS stands for Reflection Anisotropy Spectroscopy. It measures the near normal incidence reflectance of linearly polarised light along two orthogonal axes on a surface and determines the difference. The information gained in this fashion may then be used in calculations of the surface dielectric response and to give an insight into some aspects of the behaviour of the surface electrons. Although other optical techniques can also yield useful information about surface electronic structure, RAS has the advantage of being relatively inexpensive and, for cubic crystals, highly surface specific.

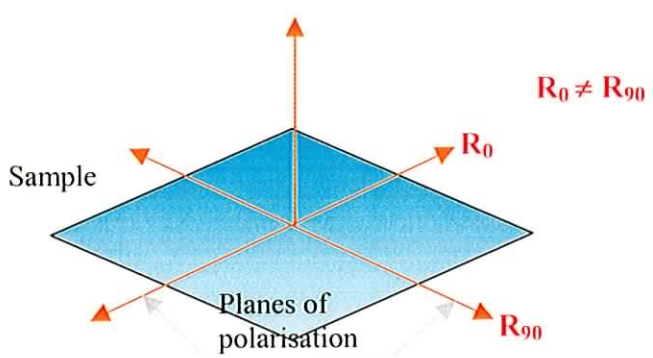

Figure 2.1: RAS geometry on a cubic material, showing the selection of polarisation orientations to negate the bulk response.

It achieves surface specificity through the orthogonal measurements outlined above. If the bulk material being examined has cubic symmetry, its contribution to the reflectance of linearly polarised light along any axis will remain the same under a 90^0 rotation. RAS measures two such reflectances, and subtracts them. The result will therefore have no bulk contribution. On initial inspection, therefore, this would appear

to be useless for examining cubic materials. However, when surface reconstructions are considered, it is found that this is not necessarily the case.

The reconstruction of a surface involves the surface atoms relaxing from the positions they would occupy in the bulk material into new positions, and possibly the addition of new atoms. This minimises the strain on the atoms caused by the unbalanced forces that act on them due to the presence of the surface, thereby minimising the surface energy. In some cases, the surface may have different in-plane symmetry to the bulk material. It is in these cases that RAS becomes a useful technique, as any structural symmetry differences that exist provide the possibility that the electronic structure may demonstrate similarly modified symmetry with respect to the bulk. RAS measurements here will largely negate the bulk contribution, but the surface contribution will remain, and although it will probably be small, RAS may be able to detect it. This condition is likely to arise when materials are absorbed onto a surface, and RAS has a high surface specificity in this case.

2.3 Analysis

RAS is one of a handful of techniques, including photoluminescence, and spectroscopic ellipsometry, that depend on $\chi^{(1)}$. As mentioned earlier, it measures the difference in the near normal incidence (approximately 5^0) reflectance of linearly polarised light along two orthogonal axes of a crystal. The geometry of such an arrangement is shown in figure 2.2.

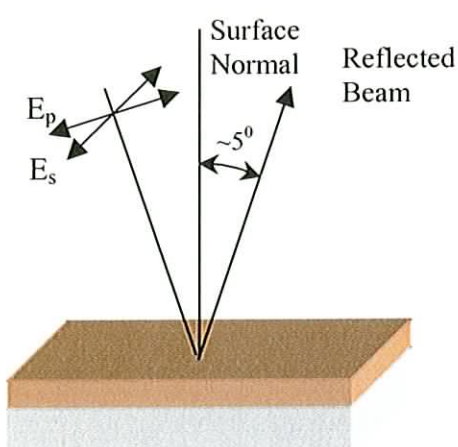

Figure 2.2: Reflection geometry from a three phase system, with an exaggerated representation of the angles of incidence and reflection.

Here, E_p refers to light polarised in the plane of incidence, and E_s to light polarised perpendicular to the plane of incidence. Reflection from such a surface is described by the well-known Fresnel equations, which may be found in most undergraduate optics textbooks, e.g. Hecht.[4]

In a strict sense, a surface that has reconstructed may be considered to be an interface between two crystals with dielectric tensor components ε_{ixx}, ε_{iyy}, and ε_{izz}. ε_{ixx} is the x response of the dielectric tensor to x components of the incident beam in medium i, where i = 1 (surface or thin film) or 2 (substrate or bulk material), and x and y are defined as in the surface plane and z perpendicular to it. If the bulk material or substrate is isotropic, then the tensor components are the same along each material axis. This allows ε_{2jj}, where j = x, y or z, to be replaced by the single component ε_b, the isotropic bulk dielectric constant.

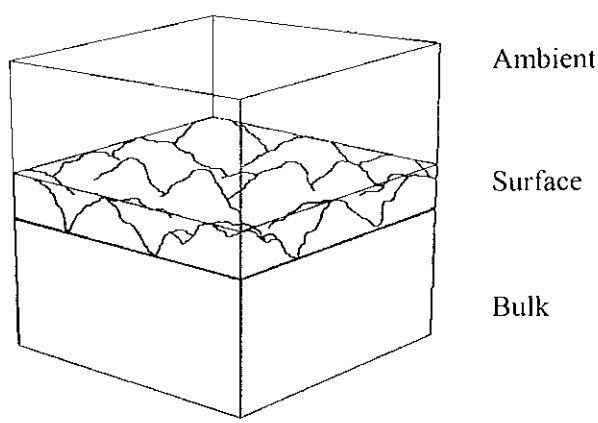

Figure 2.3. Representation of a surface using the three phase model,[5] that may be used in calculating the reflectance of a surface.

The division of the surface into three distinct regions, bulk, thin film and vacuum, is known as the three phase model,[5] figure 2.3. Using this and the Fresnel equations, expressions may be derived for the s and p polarised light from such a surface.[6] As RAS is only concerned with the reflectance of p-polarised light from a p-polarised incident beam, only that equation will be quoted.

$$\frac{r_{pp}(\phi_0,\psi)}{r_{pp}^0} = 1 + \frac{i4\pi d\cos\phi_0}{\lambda(\varepsilon_b - 1)(\varepsilon_b\cos^2\phi_0 - \sin^2\phi_0)}[(\varepsilon_b - \bar{\varepsilon})\varepsilon_b - \left(\left(\frac{\varepsilon_b^2}{\varepsilon_{zz}}\right) - \bar{\varepsilon}\right)\sin^2\phi_0 + \Delta\varepsilon(\varepsilon_b - \sin^2\phi_0)\cos 2\psi] \quad \text{Eq. 2.2}$$

where

$$\bar{\varepsilon} = \frac{\varepsilon_{xx} + \varepsilon_{yy}}{2} \quad \text{and } \Delta\varepsilon = \frac{\varepsilon_{yy} - \varepsilon_{xx}}{2} \quad \text{Eq. 2.3}$$

r^0_{pp}= bulk reflection of p-polarised light from p-polarised incident beam

r_{pp}= surface reflection of p-polarised light from p-polarised incident beam

ϕ_0 =angle of incidence

ψ = azimuthal angle with respect to the place of incidence

r = reflectance

d = depth of material

and ε_{ixx} has been replaced with ε_{xx}, etc.

In the normal incidence case, ϕ_0 is 0 and this equation simplifies to:

$$\frac{r_{pp}(\phi_0,\psi)}{r_{pp}^0} = 1 + \frac{i4\pi d}{\lambda(\varepsilon_b - 1)}[\varepsilon_b - \bar{\varepsilon} + \Delta\varepsilon\cos 2\psi] \quad \text{Eq. 2.4}$$

RAS may be defined as:[7,8]

$$\frac{\Delta r}{r} = 2\frac{r_{pp}(0^0,90^0) - r_{pp}(0^0,0^0)}{r_{pp}(0^0,90^0) + r_{pp}(0^0,0^0)} \quad \text{Eq. 2.5}$$

where Δr is the difference in reflectance between the two axes.

and, if

$$r_{pp}(0^0,90^0) = 1 + \frac{i4\pi d}{\lambda(\varepsilon_b - 1)}[\varepsilon_b - \varepsilon_{yy}]$$

and

$$r_{pp}(0^0,0^0) = 1 + \frac{i4\pi d}{\lambda(\varepsilon_b - 1)}[\varepsilon_b - \varepsilon_{xx}] \quad \text{Eq. 2.6}$$

then substitution into equation 2.5 yields the following expression:

$$\frac{\Delta r}{r} = \frac{i4\pi d}{\lambda}\frac{(\varepsilon_{xx} - \varepsilon_{yy})}{\varepsilon_b - 1} \quad \text{Eq. 2.7}$$

where d is the depth of the surface reconstruction (medium 1) and λ the incident light wavelength. This is not an experimentally usable equation for the RA spectrometer, but it can aid in the calculation of surface dielectric tensor components and a general understanding of the RA response.

2.4 Summary

This chapter has shown the surface response of a system in a RAS configuration. In the next chapter a Jones vector analysis is applied to a practical RAS instrument to determine the detector response to an elliptically polarised surface response.

2.5 References

[1] e.g. H. Bast, et. al, Handbook of Optics, Opt. Soc. Of America, McGraw-Hill, 1995,

[2] R. W. Ditchburn, Light, 2nd ed., Blackie and Son, 1963,

[3] Z. Knittl, Optics of thin films, Wiley, 1976

[4] E. Hecht, Optics, 2nd ed., Addison-Wesley Publishing Co. Inc., 1987

[5] R. M. A. Azzam, N. M. Bashara, Ellipsometry and polarised light, North Holland, Amsterdam, 1977

[6] K. Hingerl, D. E. Aspnes, I. Kamiya, L. T. Florez, Appl. Phys. Lett. 63 885 (1993)

[7] D. E. Aspnes, J.Vac. Sci. Tech. B 3 1498 (1985)

[8] V. L. Berkovitz, I. V. Makarenko, T. A. Minishvili, V. I. Safarov, Solid State Communications **56** 449 (1985)

Chapter 3

The RAS Instrument

This chapter will present a Jones vector analysis of the RAS instrument and mention some important considerations about its construction. The actual construction of the RAS will be dealt with in the next chapter.

3.1 Initial Considerations

The experimental configuration of an RA spectrometer must be considered. A light source with sufficient intensity, spectral range and stability is an obvious first requirement, along with some means of polarising its output and directing it onto a sample. There must be some means of analysing the output. As well as analysing the output on an energy basis (e.g. a monochromator) this must also be capable of analysing along two different surface directions on the target material. Finally, a suitable detection system is required that can separate the small RAS signal from the larger background. These requirements are summarised as follows.

(i) A light source with sufficient intensity to provide an adequate signal after reflection from most surfaces. It must also have appropriate spectral range to allow for a meaningful study of the material. As in all spectroscopic applications, the light source should also have a stable output, with fluctuations over time kept to an minimum.

(ii) As the optical probe is a polarised beam, a polariser is required for the lamp output. Its spectral transmission should match the lamp's spectral profile.

(iii) Depending on the arrangement of the spectrometer and sample, an arrangement of mirrors may be required to direct the light onto the sample. These should not affect the spectral profile and be positioned so that they do not affect the polarisation. This requires that they are not between the polariser-sample and sample-analyser.

(iv) Light analysis requires three components:

(a) A means of analysing along two directions on the surface. The original approach to this was to rotate the sample, but more recent methods use optical means of rotating the direction of the polarised light either before or after reflection. This is accomplished using a PEM, which will be described later.

(b) A second polariser is needed to analyse the reflected beam

(c) A monochromator (or prism, depending on the setup) is used to examine the reflectance throughout the energy range provided by the lamp and optics

(v) A detection system is required which can convert the optical signal into an electrical signal. The most common types are photomultiplier tubes and photodiodes.

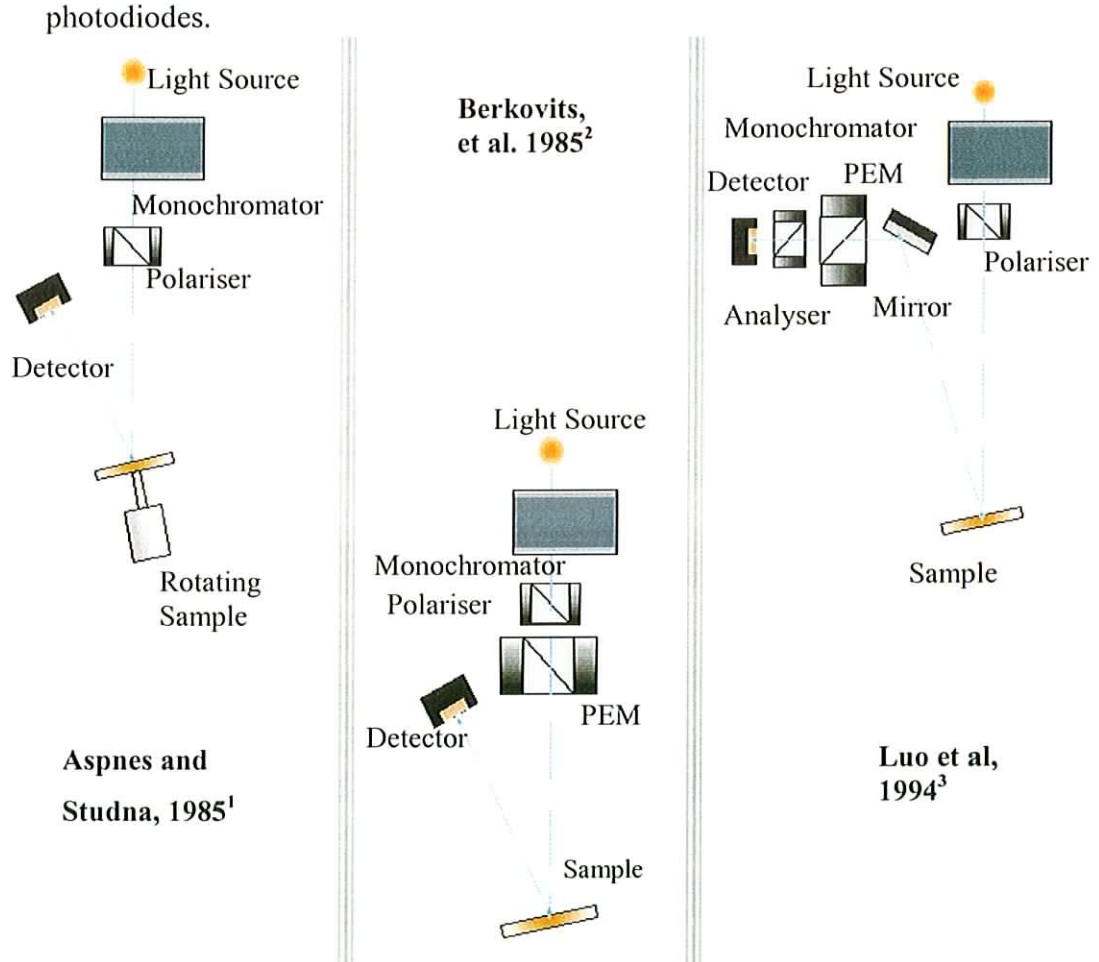

Figure 3.1: Alternative RAS configuration from various sources, showing the different setup possibilities.

(vi) The electrical signal must be collected and analysed by a computer. This requires amplifiers and analogue to digital converters. Requirements here can depend on the selection of the optical components and detection system.

3.2 Instrument Configuration

Several configurations are possible and have been tried by various groups, and each has particular strengths and weaknesses. Some of these are shown in figure 3.1. The setup chosen in this instance is shown in figure 3.2. This is very similar to Luo's setup, with the monochromator placed after the analyser, rather than in front of the lamp. It was chosen for its compactness.

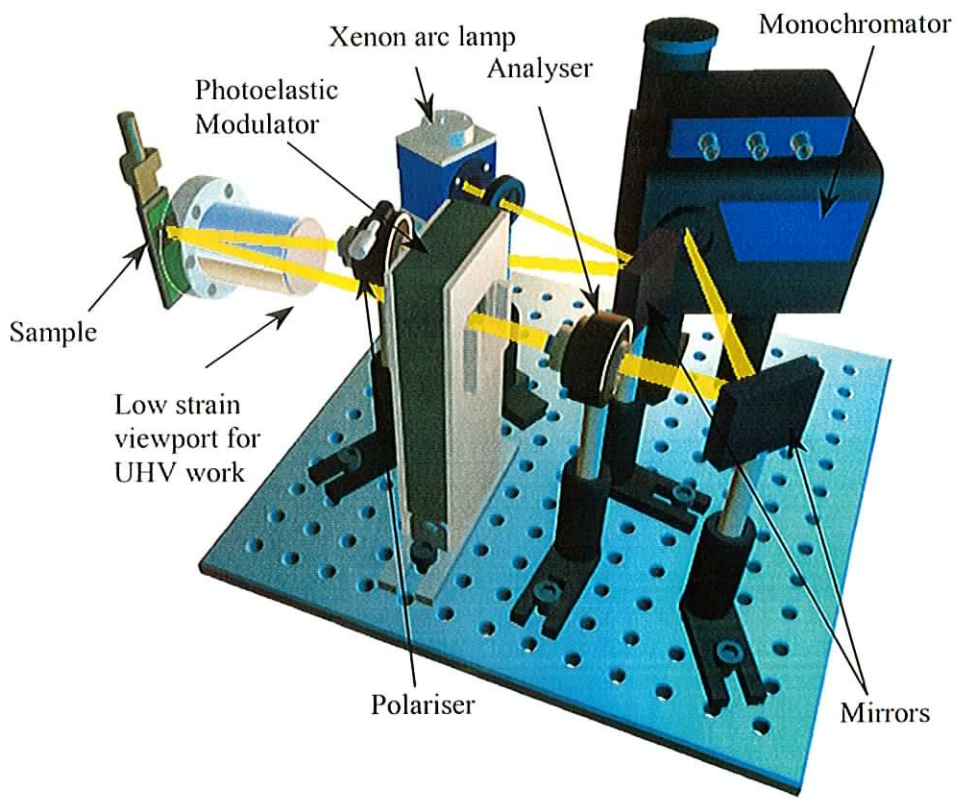

Figure 3.2: The chosen RAS configuration. It closely resembles Luo's set-up, with the monochromator moved behind the analyser rather than in front of the lamp. The light path through the instrument is also shown.

It uses a linear polariser and a high intensity Xenon lamp to generate the incident beam and select the axes to study. This is accomplished as shown in figure 3.3. The components at $\pm 45^0$ will be equal in magnitude.

A PEM is used to analyse the reflected light. It consists of a birefringent crystal driven by an oscillator. The oscillations are applied along one axis only, and therefore one axis is modulated, and the other is not.

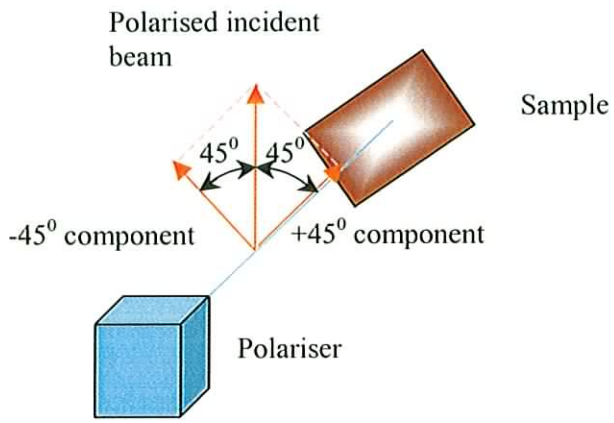

Figure 3.3: A representation of the way the polariser orientation determines the two polarisation axes that are examined.

This results in a sinusoidally varying phase retardation along the modulated axis at the oscillator frequency. With appropriate compression of the crystal, the magnitude of this retardation can be selected. In RAS, if the input polarisation states are correctly aligned with respect to the driven axis, the PEM will have the effect of selecting between two orientations at $\pm 45^0$ to this input.

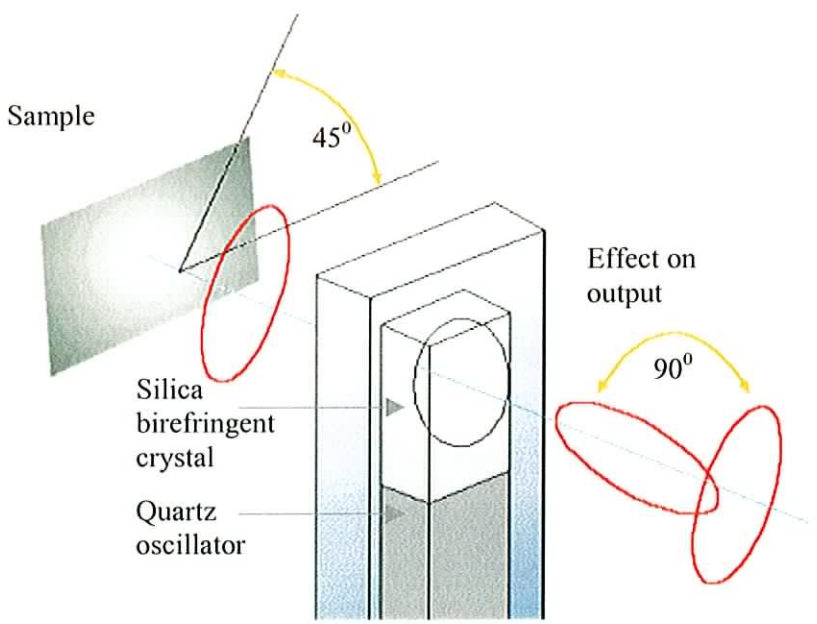

Figure 3.4: An example of how the PEM rotates the polarisation angle of an input beam, in this case through 90^0. This allows an analyser, orientated along the major axis of one of the output ellipses, to alternately see the major and minor axes as the light is rotated.

As these are the analysis directions specified by the polariser, the PEM allows rapid examination of the reflectance along both axes. A linear polariser is placed after the PEM at 45^0. This alternately sees a slice of the ellipse along the major and minor axes, which generates a time varying signal as the PEM rotates the polarisation state of its input beam and is proportional to the difference between the major and minor axes. This is passed into a monochromator for energy discrimination and finally into a photodetector.

To generate an equation for this system, the influence of each component on the light's polarisation state must be considered. The Jones Vector approach is ideally suited to this task. It represents polarised light as a vector, and optical components as 2x2 matrices. Subsequent interactions of the light with the optical components are calculated by multiplying the element matrices and applying the result to the vector. As it can only represent polarised light, only the optical components after the first polariser needs to be considered. On the spectrometer, this consists of the polarisers, and the PEM. In addition, the vacuum chambers viewport (if present) and the sample itself must also be accounted for.

3.3 Jones Vector Analysis of RAS Instrument

Using Jones vector convention, a beam travelling along the z-axis with electric field components E_x and E_y is given by

$$\vec{E} = \begin{pmatrix} E_x \\ E_y \end{pmatrix} \qquad \text{Eq. 3.1}$$

Each of the optical components may be analysed to find the contribution each makes. Beginning with the input polariser, it is responsible for polarising the input beam, and has no operation matrix as such. Ideally then, for x-polarised light, its output would be

$$\vec{E} = \begin{pmatrix} 1 \\ 0 \end{pmatrix} \qquad \text{Eq. 3.2}$$

However, due to imperfections in the polarising crystal and misalignment, this becomes

$$\vec{E} = \begin{pmatrix} 1 \\ ia_p - \Delta P \end{pmatrix} \qquad \text{Eq. 3.3}$$

Where ia_p is due to polariser imperfection and ΔP is the polariser misalignment. The other components may be analysed in a similar fashion. As this has been done elsewhere,[4,5] it is sufficient to summarise the results here. There will be some strain induced birefringence in the chamber window, and this will affect the polarisation state of any polarised incident beam. In matrix form, this may be represented by the following matrix

$$\text{Input window matrix} = \begin{pmatrix} 1+F_{1c} & F_{1s} \\ F_{1s} & 1+F_{1c} \end{pmatrix} \qquad \text{Eq. 3.4}$$

The sample must also affect the polarisation state of the beam, and this is given by

$$\text{Sample Effect} = \begin{pmatrix} \bar{r} & \frac{\Delta r}{2} \\ \frac{\Delta r}{2} & \bar{r} \end{pmatrix} \qquad \text{Eq. 3.5}$$

Where $\bar{r}$ is the average reflectance and Δr is the reflectance difference along the selected axes. As the beam exits the window at a different position to the entry point, a different matrix is needed. It is of the same form as the input matrix, with different terms accounting for the strain difference at the two locations

$$\text{Exit window matrix} = \begin{pmatrix} 1+F_{2c} & F_{2s} \\ F_{2s} & 1+F_{2c} \end{pmatrix} \qquad \text{Eq. 3.6}$$

The PEM sinusoidally retards the phase of any component incident along its modulation axes. Its effect on the polarisation may be represented by

$$\text{PEM matrix} = \begin{pmatrix} e^{i\frac{\varphi}{2}} & \Delta M\left(e^{i\frac{\varphi}{2}} - e^{-i\frac{\varphi}{2}}\right) \\ \Delta M\left(e^{i\frac{\varphi}{2}} - e^{-i\frac{\varphi}{2}}\right) & e^{-i\frac{\varphi}{2}} \end{pmatrix} \qquad \text{Eq. 3.7}$$

where φ is the PEM's retardation and ΔM is its misalignment.

Finally, misalignments and defects in the analyser must also be considered.

$$\text{Analyser} = \begin{pmatrix} 1-\Delta A & 1+\Delta A \\ -ia_a & ia_a \end{pmatrix} \qquad \text{Eq. 3.8}$$

As the photodetector is not sensitive to changes in polarisation the mirror and monochromator do not need to be considered. The total contribution from all components is therefore given by the tensor operation

$$\vec{E}_{res} = (Analyser)(PEM)(Window)(Sample)(Window)\begin{pmatrix} E_{x-Pol} \\ E_{y-Pol} \end{pmatrix} \qquad \text{Eq. 3.9}$$

Or, in full

$$\vec{E}_{res} = \begin{pmatrix} 1-\Delta A & 1+\Delta A \\ -ia_a & ia_a \end{pmatrix} \begin{pmatrix} e^{i\frac{\varphi}{2}} & \Delta M\left(e^{i\frac{\varphi}{2}} - e^{-i\frac{\varphi}{2}}\right) \\ \Delta M\left(e^{i\frac{\varphi}{2}} - e^{-i\frac{\varphi}{2}}\right) & e^{-i\frac{\varphi}{2}} \end{pmatrix} \begin{pmatrix} 1+F_{2c} & F_{2s} \\ F_{2s} & 1+F_{2c} \end{pmatrix}$$

$$\begin{pmatrix} \bar{r} & \frac{\Delta r}{2} \\ \frac{\Delta r}{2} & \bar{r} \end{pmatrix} \begin{pmatrix} 1+F_{1c} & F_{1s} \\ F_{1s} & 1+F_{1c} \end{pmatrix} \begin{pmatrix} 1 \\ ia_p - \Delta P \end{pmatrix} \qquad \text{Eq. 3.10}$$

This operation is straightforward, but quite long, and would require several pages, if not a full chapter, for a complete expansion. This may be found elsewhere.[4,5] However, to summarise, expressions are found for E_x and E_y, and E_x is found to dominate. E_y is therefore neglected and E_x is converted into an intensity by multiplying by its complex conjugate E_x^*. Further manipulation results in an expression that describes a time varying current in the photodetector, which is proportional to the reflectance anisotropy.

$$\frac{\Delta I}{I} = 2\left[-\mathrm{Im}\left(\frac{\Delta r}{r}\right) + \delta_1 \cos 2\gamma_1 + \delta_2 \cos 2\gamma_2 - 2a_p\right] J_1(\delta_{PEM}) \sin \omega t$$
$$+ 2\left[\mathrm{Re}\left(\frac{\Delta r}{r}\right) + 2\Delta P + 2\Delta M\right] J_2(\delta_{PEM}) \cos 2\omega t \qquad \text{Eq. 3.11}$$

where;

I	Photodetector current
ΔI	change in photodetector current
γ_1	azimuthal offset of window strain for incident beam
γ_2	azimuthal offset of window strain for reflected beam.
δ_1,	incident beam window strain retardation
δ_2	reflected beam window strain retardation
δ_{PEM}	PEM retardation
ΔP	misalignment of polariser
ΔM	misalignment of PEM
J_1, J_2	Bessel functions
ω	PEM modulation angular frequency

The terms in this equation reveal many important points about the effective operation of an RA spectrometer which will be examined in the next chapter. Only those which have first order effects are included, as the others are assumed to be negligible on a properly set up system. It also shows on which part of the spectra (real or imaginary) that the effects are strongest, for example, ΔP and ΔM have a substantial effect on the real part, but not on the imaginary (again, to first order). Possibly the most important consequence of the equation is that the *anisotropy is modulated at the PEM frequency*, and *its real and imaginary parts have different frequency dependencies (2ω and ω respectively).* This makes them easily distinguishable by lock-in detection, via f and 2f modes.

Lock-in amplifiers will be described in the next chapter, but a lock-in amplifier would generally be employed in any situation where a sinusoidal signal is to be detected, particularly when this is a modulation used to extract a small signal from a high noise background. RAS is an example of this, and a lock-in amplifier will be found in almost all RAS setups.

3.4 Summary

This chapter has presented and partially derived an equation that may be used in a practical spectrometer. Although there are many consequences of this expression that

may be apparent, they have not been introduced yet. It will be more appropriate to do so in the next chapter, which will detail the design, construction and operation of an RAS spectrometer.

3.5 References

[1] e.g. D. E Aspnes, A. A. Studna, Appl. Phys. Lett. **46**, 1071 (1985)

[2] V. L. Berkovits, L. F. Ivantsov, V. A. Kiselev, I. V. Makarenko, T. A. Minashvili, V. I. Safarov, JETP Lett. **41**, 551 (1985)

[3] J. S. Luo, J. M. Olson, K. A. Bertness, M. E. Raikh, E. V. Tsiper, J. Vac. Sci. Technol. B **12**, 2552 (1994)

[4] D. E. Aspnes, J. P. Harbison, A. A. Studna, L. T. Florez J. Vac. Sci. Tech, A 6 (3) 1327 (1988)

[5] D. E. Aspnes, J. P. Harbison, A. A. Studna, L. T. Florez, Appl. Phys. Lett. 52 (12) 957 (1988)

Chapter 4

RAS Construction and Operation.

This chapter will build on some of basic ideas introduced in the previous chapter and illustrate how they are relevant to the design and operation of an RAS spectrometer. The selection, optimisation and, in some cases, construction of the required components will be shown in detail. The operation of the instrument will be shown and the information it may obtain, with reference to the experimental equation (Eq. 3.11), introduced in the preceding chapter.

4.1 Component Arrangement

The optical arrangement chosen in this case was shown in the previous chapter. It is shown again schematically in figure 4.1.

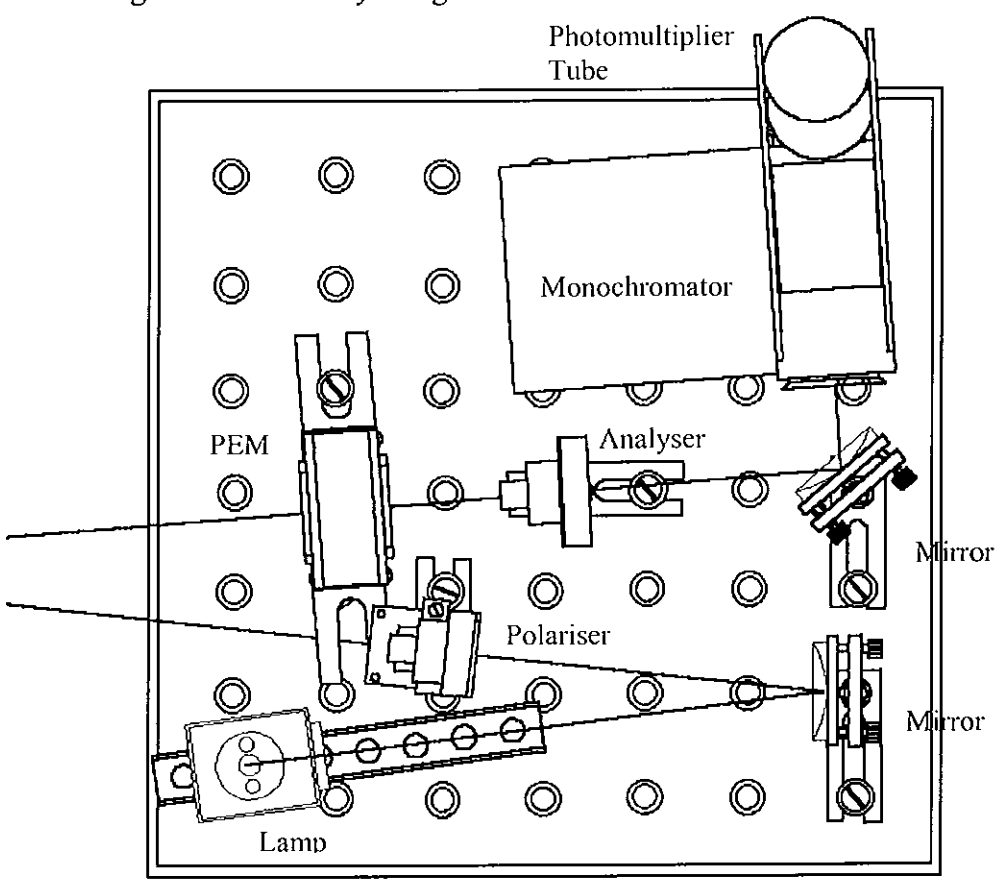

Figure 4.1: A RAS schematic showing the instrument layout on an optical breadboard.

It is possible to see all of the components and the necessary configuration. Each component will now be introduced and examined, with attention paid to requirements and optimisation.

4.2 Component Descriptions

A full list of component suppliers and specifications may be found in Appendix A.

(i) High pressure Xenon lamp. In any optical technique, adequate light intensity is of crucial importance, and RAS is no exception. As the reflectance difference is very small compared to the absolute reflectance, this is an additional problem, as fluctuations in the light source may be contribute significant noise to the RAS signal. The required light source must be of sufficient intensity that the signal is not buried in background noise, and sufficiently stable that it does not contribute to the noise itself. It is also advantageous if the lamp has a small spot size, to enable examination of small samples.

The light source chosen was a high pressure Xenon discharge lamp. It meets all of the above requirements as well or better than the only other real alternative, a tungsten filament lamp. Its only disadvantage is the presence of the high frequency jitter that affects all discharge lamps. In this case, the lamp intensity is sufficiently large that the jitter should never rise above shot noise intensity until the lamp is near the end of its life. Figure 4.2 shows the lamps intensity fluctuation with operating time.[1] In general, the lamp requires a thirty minute warm-up period before it achieves adequate stability.

A continuous mode super quiet Xenon lamp from Hamamatsu (model L2194-02) was allied to a C6979 dropper type power supply. These have been used in previous RAS applications and are known to meet all requirements to an acceptable level.

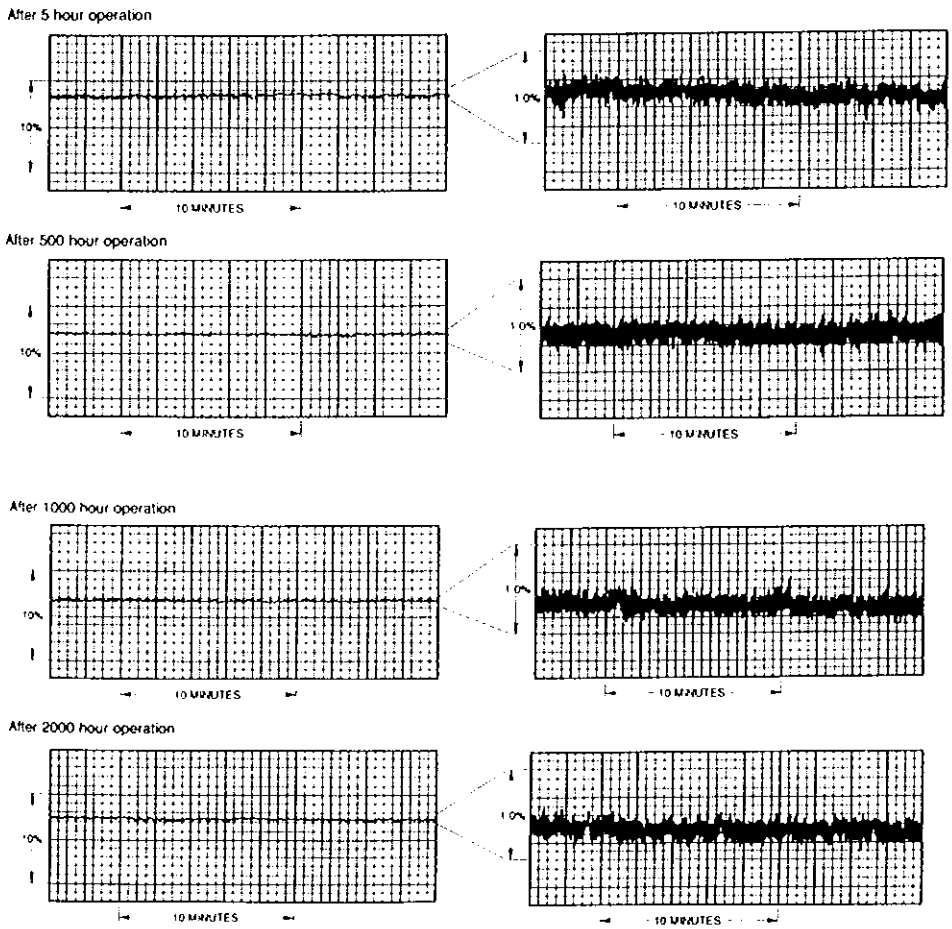

Figure 4.2: Examples of the lamp output stability at various times over its operating lifetime.[1]

(ii) Polariser: These are required to linearly polarise the probe light and specify the axes with regard to which the RA response is being measured, and to analyse the time varying signal produced by the PEM. The axis of polarisation is chosen to be at 45^0 to the axes of interest on the crystal, as shown in the previous chapter. To allow adequate UV transmission, appropriate materials must be used for the polariser crystal and any cement used in the polariser construction.

Both polarisers require rotation during RAS setup and therefore rotational mounts are required. The input polariser, especially, requires precise positioning due to its role as an axis selector. Equation 3.11 shows that inaccuracies in the polariser azimuth can introduce an offset into the real part of the RAS signal. In practice, it is found that rotational accuracy of 30'' or less is required to reduce

this offset to negligible levels.[2] A vernier mount is necessary to achieve this, and one was constructed as shown in figure 4.3

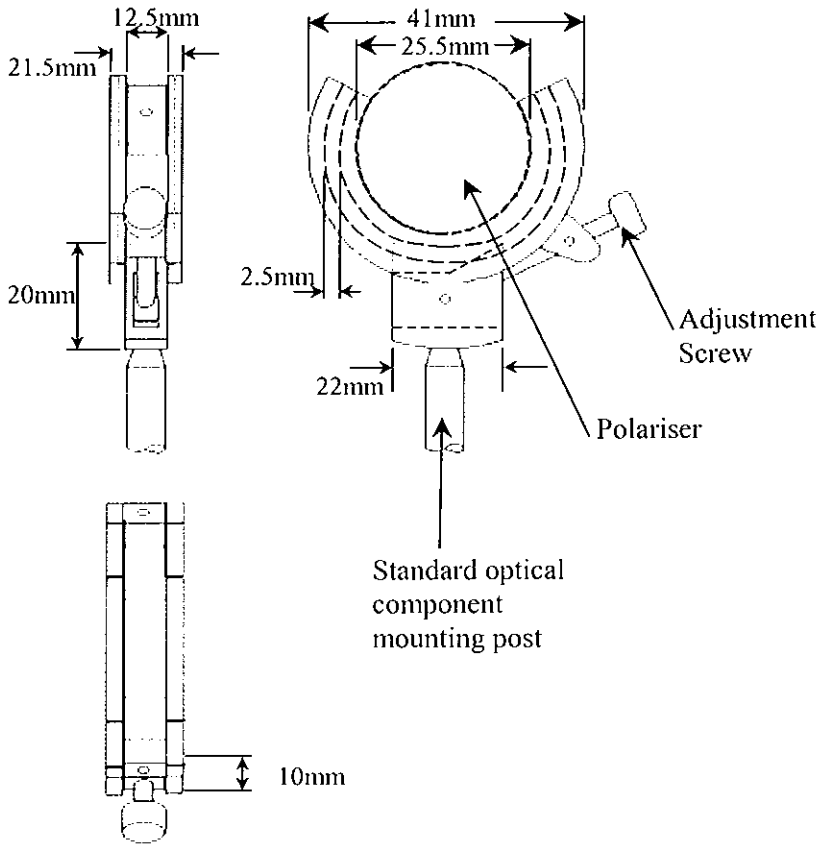

Figure 4.3: Vernier type rotation stage for polariser to provide the required rotational precision.

Care must be taken when the polarisers are being mounted, to avoid strain induced birefringence. Calcite Glan Taylor polarisers from Halbo Optics with 10mm apertures were selected for this application. Wider apertures may be used if greater intensity is required. If two polarisers of different quality are used, the better one should be used for the input polariser, due to the effects of polariser imperfections, a_p, on imaginary-part spectra (from equation 3.11). To first order, the analyser is less important in this regard. Rotational accuracy is also not as important, as analyser offset tends to affect the DC level, rather than the AC, and autophasing the lock-in may assist here. A standard non-vernier rotational mount will therefore suffice.

(iii) Low strain window. As RAS measures sample induced changes to a polarised light beam, all other influences on the beam's polarisation state must be reduced or eliminated. This was mentioned earlier when discussing the polariser mounts, but it applies to every optical component between the polariser and analyser, as it may be quite difficult to remove all birefringence effects. As the candidate quantum wire systems investigated here must be maintained in vacuum, the vacuum chamber viewport is an obvious candidate for a source of strain induced birefringence due to the pressure difference on its surface and possibly due to its attachment on a flange. Adequate spectral range is also a consideration.

It is possible to obtain windows that are specially fabricated to reduce the possibility of strain effects. They usually consist of a cylindrical arrangement, as shown in figure 4.4. This configuration distributes pressure induced strain along the side of the cylinder, rather than along its face. They may also be constructed of fused silica, for improved UV transmission.

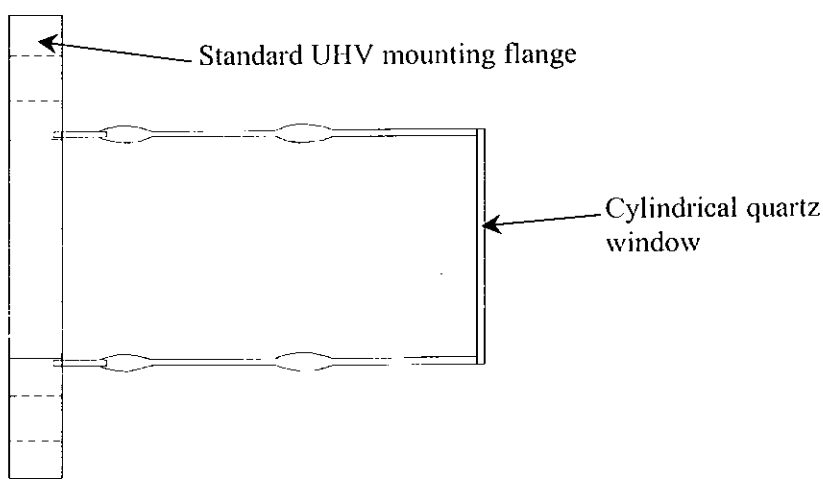

Figure 4.4: A side cutaway of a typical low strain quartz window.

Although this reduces window strain, it does not remove it entirely, and this strain will have its own RA spectra that will add to the samples. If the strain is assumed to be small and constant, however, sample spectra may be adjusted to compensate, using a procedure that will be described later. The constancy of this strain is a very important factor. Any vibrations in the chamber will be transmitted to the window, and this will modulate the polarisation effects at the vibration frequency and couple those oscillations into the light beam. If they are near any of

the PEMs harmonics, they may not be filtered by the lock-in and will result in an offset in the RA spectra. There is no way to compensate for this. If it is not to occur, the chamber must be kept as free from vibration as is possible given its configuration and use. A low strain fused silica bakeable window, for adequate spectral transmission, was purchased from EPI Europe.

(iv) Photoelastic modulator. The operation of the PEM was briefly described in the previous chapter. By modulating the retardation along one of its optical axes relative to the other, the polarisation state of any light it interacts with will be altered, as long as the light beam is not polarised along one of those axes. With appropriate set-up, it will select between the axes specified by the polariser. In order to work as efficiently as possible, its aperture must be wide enough to completely accept the light to be analysed.

During operation, the PEM crystal is compressed by a piezoelectric transducer, which is driven by a control voltage, which may be quite large. Unless adequately shielded, it may interfere with other parts of the spectrometer, especially if a photodiode detector is used. This driving voltage oscillates at a predetermined frequency, which sets the PEM's fundamental frequency. This drive voltage may or may not be a pure sinusoid, but regardless, this will not result in purely sinusoidal vibration in the crystal. This will result in the presence of higher harmonics in the PEM's oscillating output. Although this is useful in distinguishing between the real and imaginary parts of the RA response, in other regards it can pose problems, especially if the lock-in is driven by a square wave reference. This will be considered in section 4.2, (viii).

The PEM crystal may also have some residual birefringence as a result of its mounting inside the PEM, in a similar manner to the other optical components. This will add a certain constant value on to the PEM's retardation, and may be represented by equation 4.1.[3]

$$\delta_{PEM} = \delta_{PEM} \sin(\omega t) + \delta_0 \qquad \text{Eq 4.1}$$

where δ_0 is the constant strain. There is little the operator can do about this, as it is intrinsic to the PEM's manufacture, and as it is usually small it does not normally need to be considered

As with the lamp, the example of other groups working in the field has been followed and a Hinds PEM-90 with FS-50 optical head was selected for use. In this area, unlike the others, choice of alternatives is relatively limited. Indeed, to the author's knowledge, the only current alternative is a PEM from Beaglehole Instruments, which also gives good performance in an RAS setup.

(v) Monochromator. A monochromator is required for scanning over a range of photon energies. The grating must have adequate spectral range and it must in some fashion be computer controllable. Apart from these criteria and a general desire for compactness, there are no other special requirements here. There is no fine structure in RAS, so very high resolution is not required. For this reason a CM-110 monochromator from Digikröm was chosen, which is quite compact and features an onboard microcontroller and stepper motor. It has an f number of 3.3.

(vi) Mirrors. Concave mirrors are used to focus the lamp arc onto the target sample, and to focus the reflected beam into the monochromator. The nature of the mirrors is at the user's discretion, but they should have high quality reflective coatings, and the focal lengths must be appropriate for the RAS installation. As much as is possible, they should also be matched to the monochromators f number to maximise light collection. Four 25.4mm mirrors, with focal lengths of 150, 200, 250 and 500mm were selected to allow good set-up flexibility. These correspond to f numbers of 5.9, 7.8, 9.84 and 19.68 respectively. Although there is an increasing mismatch with the monochromator's f number, resulting in poorer light collection, it isn't practical in a compact design to have the larger mirror diameters that would be required for keeping the f numbers low, especially at larger focal lengths.

(vii) Detector. There are two main options here: a photomultiplier tube or a silicon photodiode. Each detection method has its own advantages. The detector sees a small AC signal, proportional to the optical anisotropy at the modulator frequency, and a large DC signal. The origin of this was seen in the previous chapter. The AC signal may be between three to five orders of magnitude smaller than the DC, so low noise signal recovery is an absolute priority and is the prime factor in detector selection.

As stated, the two options are a photomultiplier tube or a photodiode. Traditionally, low noise detection has been the domain of the photomultiplier, as its gain occurs at the dynodes and it has no need for noisy electronic amplification. However, advances in silicon photodiode design and low noise IC amplifiers have made the photodiode a viable choice again. The diode's traditional strengths have been greater ease of use, no need for high supply voltages, greater robustness and smaller size, but here too, the photomultiplier tube has made advances, with increasing miniaturisation and on-board power supplies greatly easing the convenience of their use. When using a photodiode, it is important to consider the PEM's driving voltage. Unless the diode and PEM are adequately shielded, the diode may be affected by the large electric field that this can generate. The photomultipler is generally unaffected by electric fields, but is quite vulnerable to magnetic fields, which may deflect electrons away from the dynodes. Most PM tubes can be purchased with appropriate magnetic shielding.

Although low noise electronic amplification of a photodiode output is possible to RAS specifications, it may be quite difficult to achieve. In this instance, a Hamamatsu S1227-66BQ photodiode was employed for good spectral range. Although an effective amplification circuit was produced, difficulties in its optimisation led to its eventual abandonment in favour of a photomultiplier tube.

The tube chosen was a Hamamatsu 957-08 hybrid assembly, which consists of a R928 photomultiplier tube and a built-in DC converter, which allows operation from a 15V power supply and a 0 to 4V control voltage for gain. This proved very convenient to use and was relatively compact. It did, however, require construction of a specialised holder, shown in figure 4.5, and construction of a simple amplifier.[4]

With greater time to spend on the photodiode preamplifier, it may become a more viable alternative, as the diode does have many advantages. This approach is demonstrated by research groups in Germany, who use photodiodes regularly in RA spectroscopy.[5] Miniature photomultipliers from Hamamatsu and others may however sustain interest in the photomultiplier approach.

(viii) Lock-in Amplifier. This is used to extract the RA signal from the detector output. It compares a reference frequency, selected by the operator, to a broadband input and returns the amplitude of any component of the input that is at the reference frequency. Due to the nature of the lock-in process, the output is the RMS of the selected frequency component's amplitude.

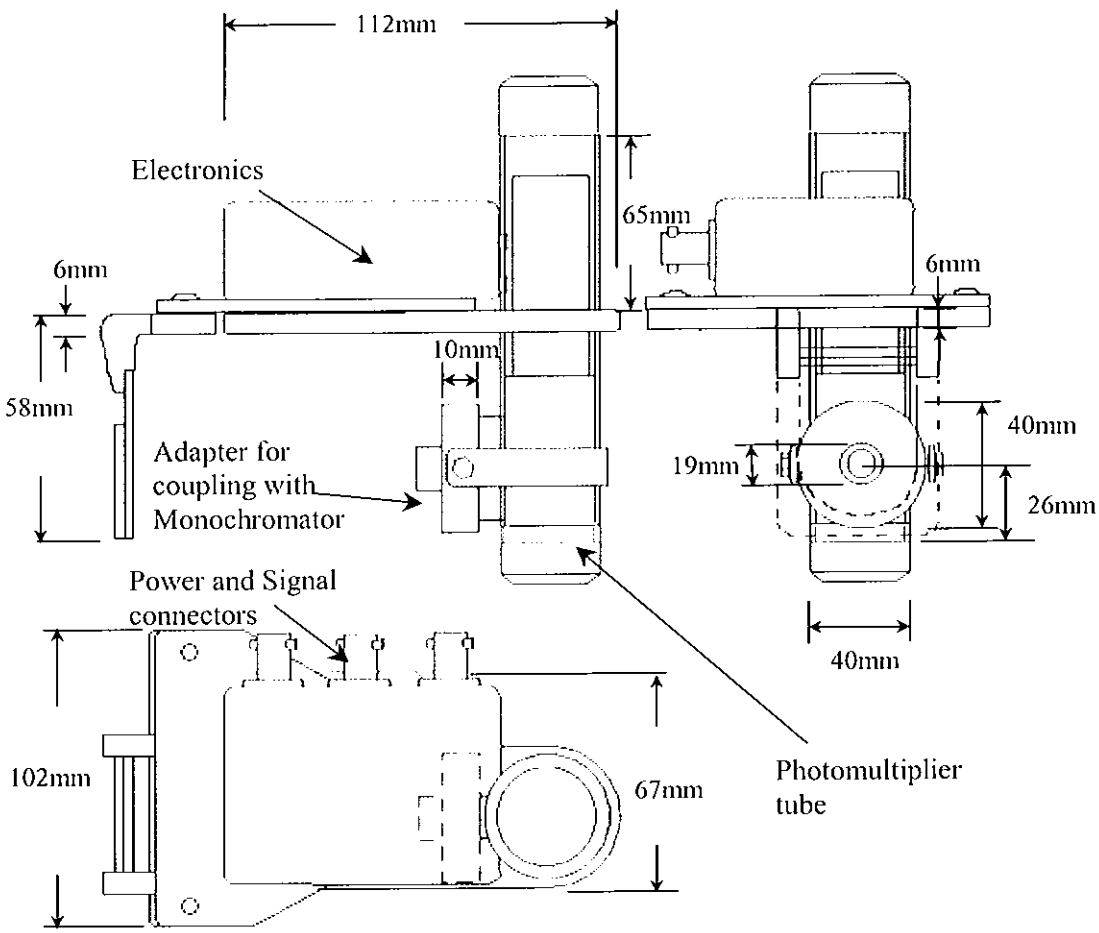

Figure 4.5. Photomultiplier tube holder and electronics assembly, designed for coupling onto the monochromator.

Generally, they operate by generating a square wave of ±1V at the reference frequency and multiplying the input by this. The output is then passed through a low pass filter. (The combination of lock-in amplifier and filter is called a phase sensitive detector or PSD). The output is then the RMS signal mentioned above. This is a general introduction, however, and many publications offer detailed explanations and discussions.[6]

As the reference is a square wave, the signal will have higher harmonics that the lock-in will also to detect. This is a potential source of problems, as the PEM generates unwanted harmonics in its output. Fortunately, due to the symmetry of the square wave, only odd harmonics are present, and the lock-in will therefore only be affected by odd harmonics of its fundamental measurement frequency. With the PEM operating at 50kHz, if the lock-in is operating in first harmonic (f) mode, the first problem frequency is 150kHz, and in second harmonic mode (2f) this becomes 300kHz. As the lock-in is only required to detect up to the PEM's second harmonic at 100kHz, a band pass filter can be used to safely prevent the higher harmonics from being detected.

To maximise the lock-in's output, the input wave must be in phase with the reference wave, for reasons which may be found in Meade, et. al.[6] Many lock-ins are provided with an autophasing system, which performs this task when required. This generally works by antiphasing the two signals, as it is easier to zero the outputs than it is to maximise them, and then adjusting the reference phase by 180^0. In general, some fine tuning will be required by the operator.

EG&G's model 5210 lock-in was used here. As well as providing excellent lock-in detection, the instrument provides one digital to analogue and four analogue to digital converters, which are ideal for controlling the photomultiplier gain and measuring the DC signal component respectively.

Once appropriate components were selected, the spectrometer was assembled as shown in figure 4.1. The selection of suitable focal length mirrors will depend on the installation of the instrument. The mirror focusing light onto the sample should be close to the lamp, to ensure it captures a sufficiently large cone of the lamp's output. The lamp has an arc length of approximately 1mm, which gives some freedom when focusing the spot onto the sample. A spot size of up to 5mm can be tolerated in some cases.

Selection of the second mirror depends on the slit size and f number of the monochromator. For reasons mentioned earlier, exact f number matching wasn't possible. To maximise the detected signal then, as much light as possible should be

focused through the slit. For most experiments described in this thesis, 1mm slits were used.

It is also essential that all components are aligned using the back reflection technique to minimise the polarisation effects of off-normal incidence reflection.

4.3 Operation of the Spectrometer

Equation 3.11 shows that there are different operational considerations depending on the spectrum being collected (real or imaginary). In both cases though, there are certain effects will have an influence on spectra of either type and the difference between effects on real or imaginary spectra is simply a matter of degree.

Assuming that sufficiently high quality polarisers were used to minimise a_p, the imaginary spectra will be influenced primarily by window strain effects. As mentioned earlier, these can occur when any vibrations around the chamber, for example the pump motors, are transmitted into the low strain window through the chamber walls. This will modulate the small birefringence in the window and may lead to an oscillating polarisation change, which may affect the output. The magnitude of its interference will depend on the magnitude of its frequency components.

The real spectra are more influenced by polariser (ΔP) and PEM (ΔM) misalignments. If present, they will reduce the output signal intensity by selecting or modulating, respectively, axes which are marginally offset from those desired. It should be noted, however, that if both polariser and PEM were misaligned by the same angle in the same direction this effect would be minimised. It is mutual misalignment that causes the greatest problems.

As mentioned, the effects should be minimised in both cases. This is accomplished in the following ways.

(i) The only real way to remove the effects of window vibration is to remove the vibration. This is best accomplished by careful consideration of the experimental layout. A secure, stable mount for the RAS will also aid greatly here.

Assuming that there are no vibrations in the window, any residual birefringence must still be accounted for. This is done using a window strain correction procedure, which works on the following premise. If, for simplicity, the axes of interest on a sample are referred to as x and y, then the RA response is simply[1]

$$\frac{\Delta r}{r} = \frac{r_x - r_y}{r_{bulk}} \qquad \text{Eq.4.2}$$

If the sample is now rotated through 90^0 the x and y axes interchange, and its response now becomes

$$\frac{\Delta r}{r} = \frac{r_y - r_x}{r_{bulk}} \qquad \text{Eq.4.3}$$

which is the negative of the original response. If both spectra are added, the result will be zero RAS. If a strained window lies along the optical path, however, it will add an additional response to the detected signal. As the window is not rotated, this response will remain the same in both 0^0 and 90^0 spectra. Adding the spectra will therefore cancel the sample response and double the window response, which can then be extracted by dividing by two. Although this is not rigorously correct mathematically, it works well enough in practice. The correction is therefore

$$\frac{\Delta r_{window}}{r} = \frac{RAS_0 + RAS_{90}}{2} \qquad \text{Eq.4.4}$$

The window strain may then subtracted dynamically by the control software as each data point is collected.

(ii) As the polariser's alignment with the surface is as crucial as its relative misalignment with the PEM, an accurate means of adjusting its angle by very small amounts is required. This is achieved with a Vernier rotation stage, as described earlier.

(iii) The PEM, once positioned, should remain undisturbed unless adjustments are absolutely necessary. As far as is possible, it should be positioned with one of its

axes normal to the spectrometer base. Although this is not crucial, as any misalignment must be mirrored by the other optical components, it will aid overall spectrometer alignment. A holder, shown in figure 4.6 was constructed which allowed for small adjustments in the PEMs mount angle.

In addition, there are other more general considerations when operating the spectrometer, most of which have been described earlier. The lamp must be given sufficient time for the arc discharge to stabilise. If this is not done, it may lead to a general increase in noise, a decrease in signal intensity, or spurious spectral features, until the lamp warms up. The age of the lamp will also be a factor here, as an older lamp will be less stable.

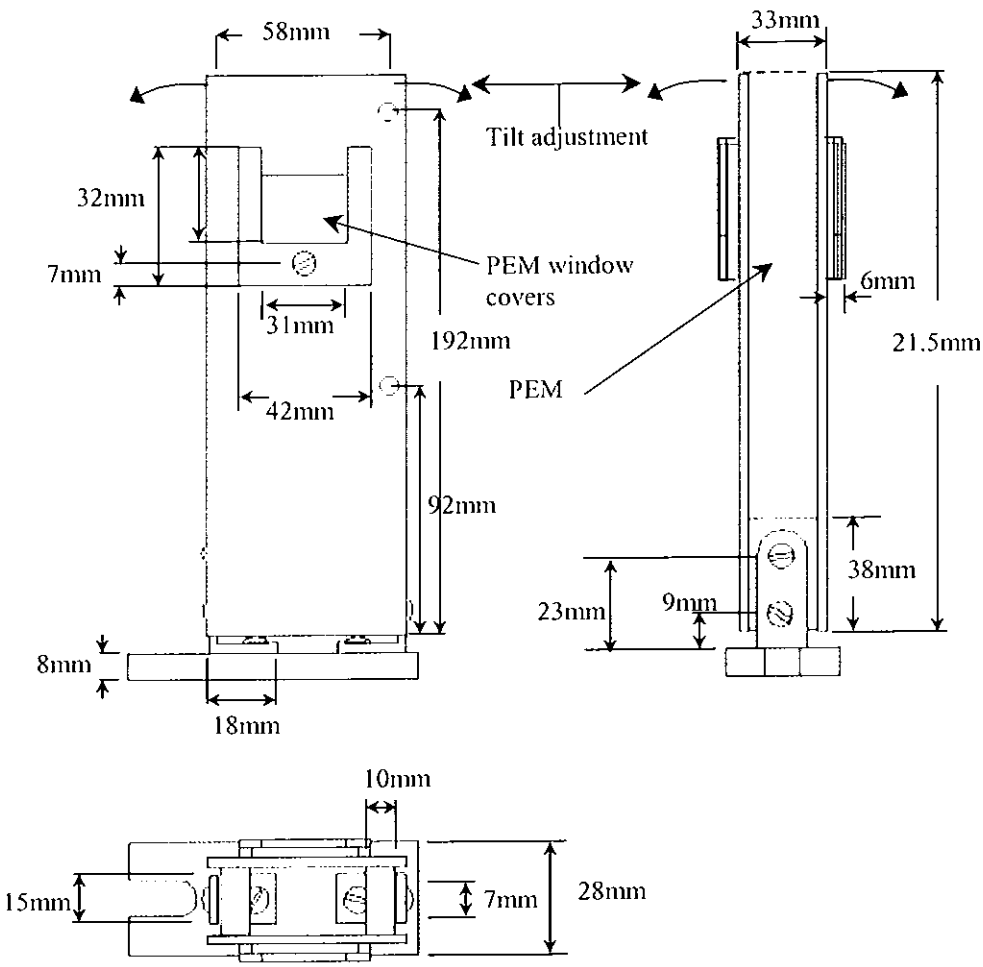

Figure 4.6: Adjustable PEM support, allowing two axis tilt adjustment of the PEM's orientation, which is important for signal maximisation.

Concave mirrors must be appropriately chosen to allow focusing of a suitable small spot onto the sample, and good collection of the reflected beam. This choice will depend on the RAS installation.

Misalignment of the analyser does not appear to be as critical. It should be aligned at 45^0 to the PEM axes to maximise the detected signal, and should subsequently be adjusted only if absolutely necessary. As even minor rotations will affect not just the signal amplitude, but also the phase relative to the lock-in reference signal, these adjustments should be made before any experimental data is taken. If it is adjusted during a run, the data may have to be abandoned, as the signal phase difference that exists during the window correction operation *must* be maintained for the duration of the experiment for data to be comparable.

When photodetectors were considered, the influence of unwanted electric and magnetic fields was mentioned. Careful thought must be given to shielding, especially in the photodiode case, as there are may be many sources of electrical noise in a typical online environment.

4.4 Signal Recovery

The output of the spectrometer should now be considered. Figure 4.7 schematically shows the control configuration for operation of an RA spectrometer from a single PC.

The configuration is relatively straightforward, and will only vary slightly with different set-ups. A PC with 3 serial ports (or a mixture of serial and GPIB, or port polling) will be sufficient to control the system. Now that the spectrometer has been correctly set up, there should be an output signal to the PC, which is mostly, if not all, sample related. This data must still undergo minor processing so it can be related to the theoretical surface response. This processing can be formulated by considering equation 3.11.

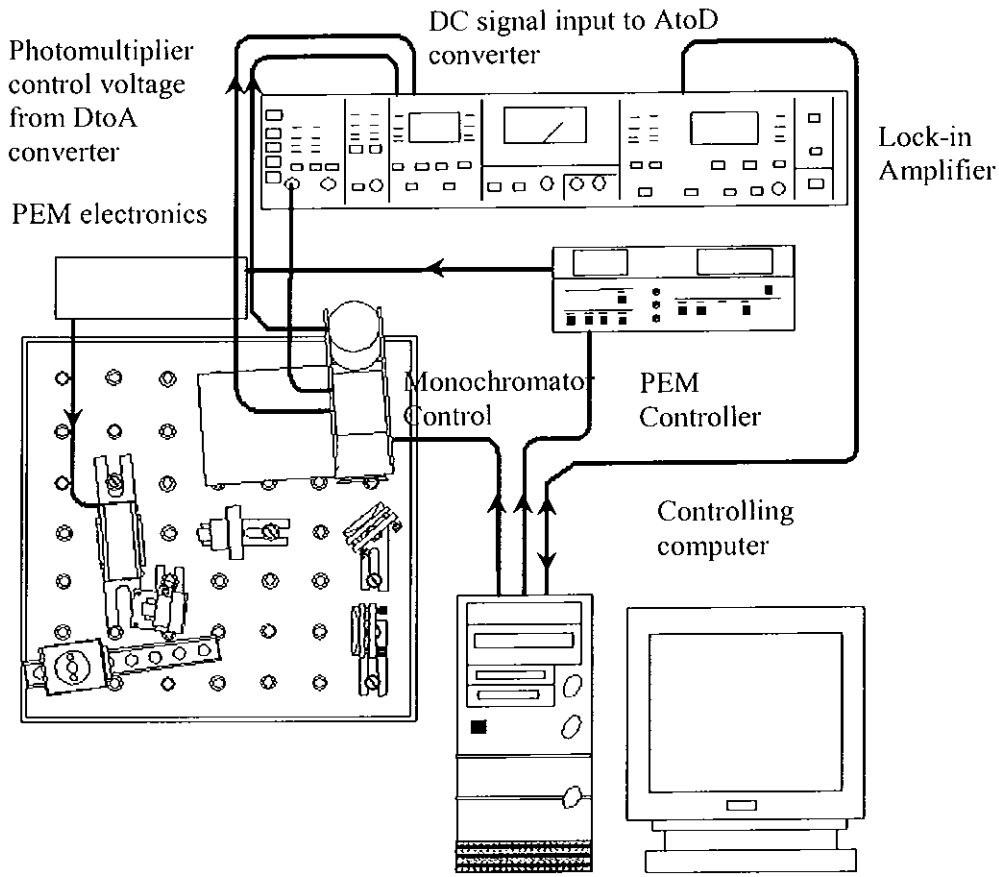

Figure 4.7: Control set-up showing the equipment required in addition to the optical components. The arrows indicate the direction of information flow.

This reveals that, in order to get an accurate, maximised output, as well as minimising the misalignments, the relevant Bessel function, J_1 or J_2, should be at its peak value. As the value of the Bessel function depends on the PEM retardation, plots of J_1 and J_2 will yield the appropriate values of δ_{PEM} for the imaginary and real response respectively. These are 1.8423 and 3.0512 radians, and these values should be used during data acquisition (Figure 4.8).

The signal current is converted into a voltage and fed into the lock-in amplifier, which will extract either the first(imaginary response) or second(real response) harmonic as specified by the PC. This RMS output is converted into a peak amplitude for calculations. The unmodulated DC current is also converted into a voltage and processed through a low pass filter into an analogue to digital converter.

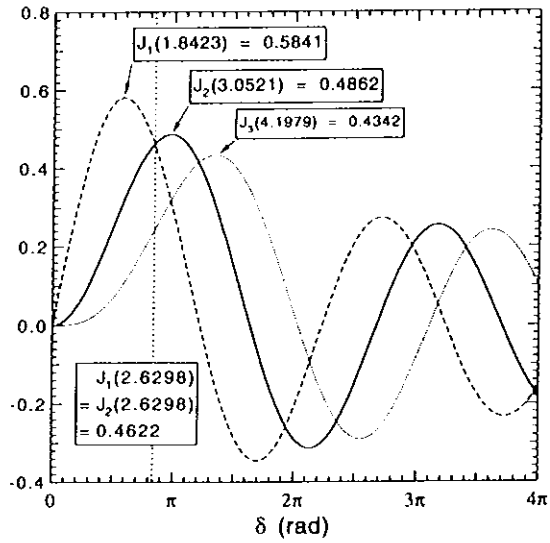

Figure 4.8: Plots of Bessel functions J_1, J_2 and J_3.

The RA response may now be related to the detector output using the following expressions, derived from equation 3.11:

$$\mathrm{Re}\left(\frac{\Delta r}{r}\right) = \frac{1}{2J_2(\delta_{PEM})}\frac{\Delta I_{2\omega}}{I} \quad \text{and} \quad \mathrm{Im}\left(\frac{\Delta r}{r}\right) = \frac{1}{2J_1(\delta_{PEM})}\frac{\Delta I_{\omega}}{I} \qquad \text{Eqs. 4.4, 4.5}$$

When measurements are taken at retardations corresponding to maximised J_1 and J_2 functions (Figure 4.8), these equations become

$$\mathrm{Re}\left(\frac{\Delta r}{r}\right) = \frac{\sqrt{2}}{2J_2(3.0521)}\frac{\Delta V_{2\omega}}{V} \quad \text{and} \quad \mathrm{Im}\left(\frac{\Delta r}{r}\right) = \frac{\sqrt{2}}{2J_1(1.8423)}\frac{\Delta V_{\omega}}{V} \qquad \text{Eqs. 4.6, 4.7}$$

$$= 1.4544\frac{\Delta V_{2\omega}}{V} \quad \text{and} \quad 1.2162\frac{\Delta V_{\omega}}{V}$$

These correction factors are therefore simply proportionality constants and may be implemented by the control software at the same time as the window correction. The software was written using National Instruments LabVIEW graphical programming package, which greatly reduced development time and aided testing, and allows configuration of most PC controllable aspects of the spectrometer, such a lock-in, PEM and monochromator settings. The software creation principally involved the

creation of three drivers to communicate with the PEM, monochromator and lockin. The EG&G supplied lockin driver had several errors that prevented it functioning, but these were easily fixed and the driver then functioned perfectly. The monochromator driver was written from the ground up. As it required byte transmission, rather than the more conventional string transmission, it was not possible to carry over any portions from the lockin driver. The PEM's communications were string based and could be accomplished with standard labVIEW functions with minimal setup.

In addition to the drivers, the program had to loop over a pre-set range of wavelength or time values to collect a spectrum and then present the information in a user interface, or front panel. A screenshot of the program's front panel is shown in figure 4.9. This also provides the user with the ability to completely configure the serial ports and some instrument settings. The program is described in more detail in appendix D.

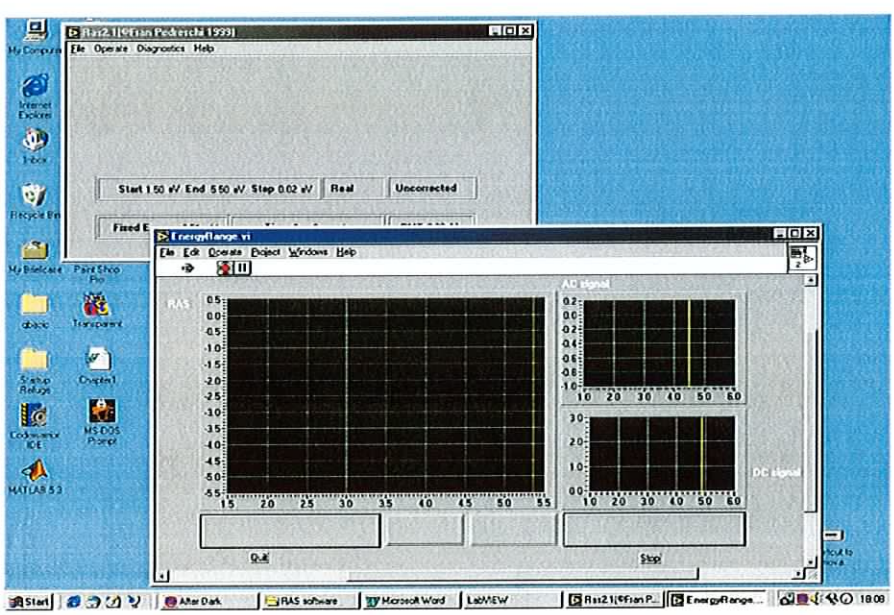

Figure 4.9: Screenshot of LabVIEW RAS control program in operation.

4.5 Uses of RAS

RAS may be used in two modes, full spectrum and dynamic. Full spectrum, as its name suggests, collects data over a range of photon energies, in this case 1.5eV to 5.5eV. This mode gathers the most information about the surface but it is slow, with an average acquisition time of three minutes for a single spectrum, which renders it unsuitable for monitoring fast reactions. Dynamic mode monitors a single wavelength

and gathers information with respect to time. Although it gives less surface information it is faster, collecting a data point approximately every second. This is limited by the monochromator slew time, the PEM settling time and the time constant of the lockin amplifier.

Both operational modes may be used in a complementary fashion. Full spectral RAS may identify photon energies of interest, which may then be examined during a reaction or process in dynamic mode. Dynamic mode spectra have also been shown to exhibit growth oscillations during the growth of multiple layered structures, in a similar manner to RHEED. As RAS requires a less specialised chamber in this instance it might ultimately prove to be a widely accepted instrument of choice in this situation.

It should also be possible to combine both techniques into one, replacing the monochromator and detector with some form of diffractive element and a CCD array type detector. This would require a complete reanalysis of the spectrometer, as different components would be used, and it poses some experimental challenges with regard to array refresh rates and modulation frequencies, but these should not prove insurmountable.

4.6 Summary

This chapter has demonstrated the setup of a RAS spectrometer and some of the more fundamental requirements necessary to its effective operation. There is more to this than could be covered in one chapter, however, and the included references have a large collection of useful information, covering some of the technique's more esoteric characteristics. Chapter 6 will demonstrate the application of RAS to selected systems, give examples of the data it can obtain and show how it may be used with other techniques to aid the characterisation of surface properties.

4.7 References

[1] *Hamamatsu photonics, L2194-02/C6979 lamp/power supply manual.*

[2] J. Rumberg, Dip. Thesis in Phys., TU Berlin, 1996

[3] O. Acher, E. Bigan, B. Drevillon, Rev. Sci. Instrum. **60** (1) 65 (1989)

[4] from P. Horowitz, W. Hill, *The Art of Electronics*, Cambridge University Press, 1989

[5] *Personal communication, J.R, Power*

[6] M. L. Meade , *Lock-in amplifiers : principles and applications,* London: Peregrinus on behalf of the Institution of Electrical Engineers, 1983

Chapter 5

Additional Experimental Techniques for Sample Characterisation

This chapter gives a brief description of the experimental techniques that were used in addition to the RAS. The techniques described are mostly commercial, off the shelf equipment with the exception of the MOKE and TRMOKE, which were constructed in-house by the magnetic group in TU Eindhoven, and the Mössbauer spectrometer, which was constructed by the Mössbauer Group at the Interfaculty Reactor Institute in TU Delft.

5.1 Atomic Force Microscopy

Atomic force microscopy is one of several scanning probe techniques in common use today.[1] It is a surface profiling technique, and was used on the nanoparticle samples described in chapter 7 to examine how the particles are arranged on the substrates following deposition.

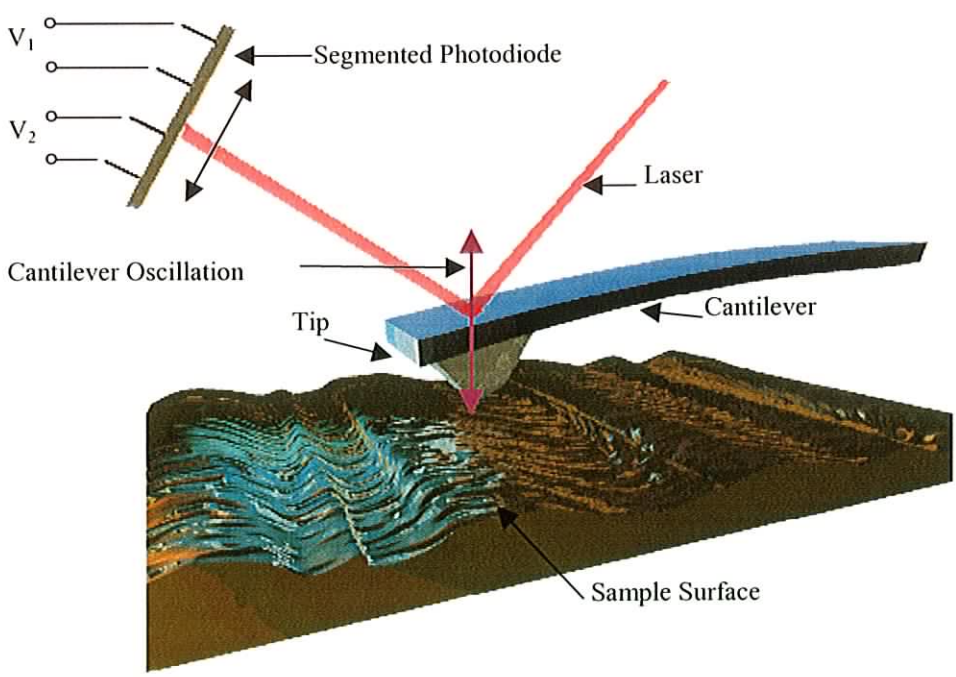

Figure 5.1: Illustration of an AFM in operation, showing the use of a reflective cantilever and a segmented photodiode to measure tip oscillations. The deflection is proportional to the ratio of the voltages across the photodiode.

Generally, it involves the use of a tip which has an apex diameter on the nanometer range, normally at least 10nm or so for commercial tips, which is mounted on a cantilever.[2] This is moved over a sample surface with a few nanometres separation. Van der Waals forces cause an interaction between the tip and the sample, producing a deflection of the tip, which is measured by reflecting a laser off the back of the cantilever onto a segmented photodiode.

There are two modes of operation. Contact mode involves bringing the cantilever close to the surface until the van der Waals forces cause it to bend. The approach then continues until the tip makes direct contact. The deflection is measured from the photodiode according to

$$\text{Deflection} \propto \frac{V_1}{V_2} \qquad \text{Eq. 5.1}$$

where V_1 and V_2 are the voltages over the two diode segments, and is proportional to the interaction force. The deflection may be measured while keeping the base of the cantilever at constant height, but this can be dangerous as large changes in surface topography may be present which could result in a tip crash. The spring constant of contact mode cantilevers is normally relatively soft to allow as much deflection as possible and reduce the likelihood of tip damage. The deflection in this case is proportional to the surface topography. Alternatively, the tip deflection may be kept constant by adjusting the height of the cantilever base as it moves. This is safer in most cases. The amount to which the base has to be moved in order to maintain constant cantilever deflection will be directly related to the surface topography.

The second mode of operation is non-contact or 'tapping' mode, where the cantilever is driven by an oscillator at its resonance frequency. The spring constant of the cantilever is greater in this case, as the tip does not normally strike the surface. The tip is again brought to within a few nanometers the surface, but not as close as in contact mode.

Instrument feedback settings will determine the actual tip-sample separation. The proportionality between force and deflection does not apply in this case, but the force gradient can be related to the spring constant by:

$$c_{z0} - \frac{dF_z}{dz} = c \qquad \text{Eq. 5.2}$$

where c_{z0} is the spring constant in the absence of an interaction, c is the actual spring constant and F_z is the z component of the interaction force. The change in spring constant causes a shift in the resonance frequency. This shift causes a change in amplitude and may cause a phase shift. The tip approach continues until the amplitude reduction reaches a set value, at which point scanning begins. The frequency shift is used to control a feedback loop, which attempts to maintain constant tip-sample separation. The average tip deflection and the phase shift may be measured. The height measurement is more common as it is again directly related to the surface topography. This latter mode of non-contact operation is more often used as it normally provides better lateral resolution than contact mode, and there is less risk of surface damage through tip contact.

5.2 Magnetic Force Microscopy (MFM)

This is a modification[2] of the AFM technique that uses a tip coated with a magnetic material such as iron. It is therefore sensitive to magnetic fields produced by a material. It was used to map the magnetic behaviour of the nanoparticle samples. Both tapping and 'contact type' modes are possible. 'Contact type' is used as a descriptor, although because the tip-sample separation is normally greater the term contact mode doesn't really apply. The greater height is necessary to separate the magnetic interaction from the topographic interaction and this is only possible at greater tip-sample separations. The image will otherwise be a convolution of magnetic and topographic information. Analogously with the AFM set-up, 'contact' mode produces an image which is proportional to the magnetic force, and tapping mode produces an image proportional to the force gradient.

It is desirable to have the tip follow the sample topography, but that is difficult in this case as the feedback loop must now be controlled by the magnetic force. This introduces a new difficulty, as unlike the van der Waals force, which is always attractive in AFM, the magnetic force can be attractive or repulsive. If tapping mode is used, which it normally is, frequency measurement is again used, but the different

force regimes can shift the frequency in different directions. As the instrument is not able to determine which way the frequency has shifted without re-tuning the cantilever, it will not be able to determine if the force is attractive or repulsive and this type of response must therefore be avoided. This is achieved by applying a potential across the tip sample gap that produces an attractive force. It is set up to make sure the tip is always attracted to the sample. Appropriate calibration removes this constant bias from the measurement.

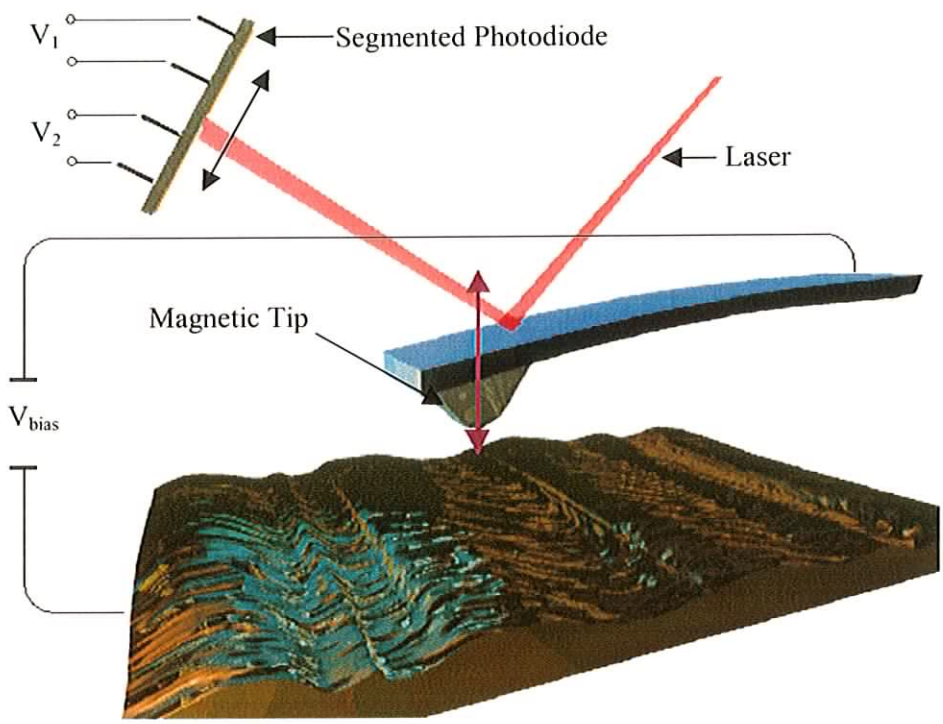

Figure 5.2: A Magnetic Force Microscope. Essentially an AFM with a magnetic tip and some software and operational changes, notably the bias voltage across the tip sample gap to ensure a monotonic tip response.

As the tip does not follow sample topography, a part of the sample that is closer to the tip will have a greater interaction and will seem to be more magnetic, which would be misleading. There are two main ways of achieving topographic compensation; (i)Digital Instruments[3] employ a 'Lift Mode' technique, where the tip makes two passes on each scan line. The first is a close range scan where van der

Waals forces will dominate, resulting in a largely topographic scan. The tip is then withdrawn by a certain fixed height, which is added to each point on the topographic scan. As this occurs on a line by line basis, the effects of thermal drift and piezo creep are minimised. (ii)Omicron[4] use a variation of this, where a rapid surface topographic scan is performed and a plane correction is derived from this. The tip is offset a fixed height from this plane and the scan is performed. This is more vulnerable to thermal drift.

Another method of topographic correction may be used in tapping mode scans. The voltage applied to the tip-sample gap may be modulated at some frequency other than the frequency at which the cantilever is being driven. This frequency may then be used to control a feedback loop which controls the tip sample height, and the magnetic information can then be obtained by frequency shift measurements of the cantilever as before. This technique has proved successful but requires considerable modification of most commercial systems.

5.3 Scanning Tunnelling Microscopy (STM)

This is another well documented scanning probe technique,[2] shown in figure 5.3. It differs from the previous in that it does not measure forces but rather images the electronic states of a sample. It was used to probe the structure of the Si(111)-4x1-In quantum wires. A tip is brought close enough to the surface so that, with a certain applied voltage across the tip-sample gap, quantum tunnelling can take place. This occurs due to the finite barrier height between the tip and sample, which results in an exponential decay of the wavefunction into the gap,

$$\psi(z) = \psi(0)e^{-\frac{\sqrt{2m(U-E)}}{\hbar}z} \qquad \text{Eq. 5.3}$$

where E is the electron energy and U is the potential. It can be shown that this tunnelling results in a current given by

$$I \propto e^{-2kd} \qquad \text{Eq. 5.4}$$

where d is the tip sample separation and k is the characteristic decay constant of the Fermi level electron wavefunctions in the tunnelling gap. Analysis yields a general expression for the current as a function of applied voltage and tip-sample distance

$$I(V,z)=\frac{4\pi e}{\hbar}\int_0^{eV} dU\rho_T(E_{F,1}-eV+U)\rho_s(E_{F,2}+U)M(U,z) \qquad \text{Eq. 5.5}$$

where U is the electron energy, ρ_s and ρ_T are the sample and tip LDOS, $E_{F,1}$ and $E_{F,2}$ are the tip and sample Fermi energies, V is the applied voltage, z is the tip-sample distance and M is a factor related to tip and sample wavefunction overlap.

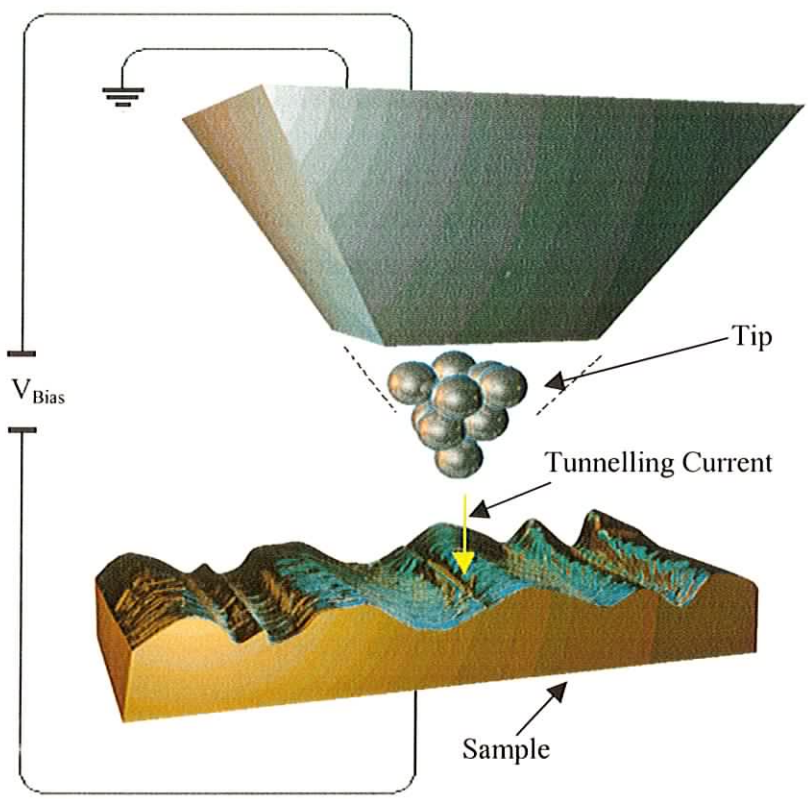

Figure 5.3: Illustration of a Scanning Tunnelling Microscope. If the tip sample bias is sufficient, electrons will tunnel from the tip to the sample or vice versa. In practice the tip will not be as sharp as that portrayed here.

If the sample is positively biased with respect to the sample, electrons will tunnel from occupied states in the tip into unoccupied states in the sample, and if it is negatively biased they will tunnel from occupied sample states into unoccupied tip states. Only states that lie between the Fermi levels of the tip and the sample can be involved in tunnelling. Theoretical descriptions of STM can be found in many

sources,[2] and it can be shown that the final tunnelling current depends on the tip sample distance and the degree of wavefunction overlap.

As with the AFM and MFM, there are several modes of operation. The tunnelling current may be used to drive a feedback loop, which maintains constant current by adjusting the tip height as the sample moves. It may also be used in constant height mode, when the current will change as the tip is moved over a surface with changing topography. As before, care must be taken in this case to avoid a tip crash, so it should only be used on very flat samples.

The instrument may also be used spectroscopically, where the tip-sample bias is varied between two set points and the tunnelling current measured. From these I/V curves information on the LDOS around the Fermi level can be obtained. There is no analogous mode of operation in AFM/MFM.

5.4 MagnetoOptical Kerr Effect (MOKE).

This effect is the change in the polarisation state of linearly polarised light reflected from a surface of a magnetic material, and was discovered by John Kerr in 1877. It is quite similar in principle to RAS, but the incident light is considered to be made up of two superimposed circularly polarised beams, rather than two linearly polarised beams.[5] A magnetic material, or a material which is magnetised by an external field, will have an unbalanced spin population in its energy levels. Opposing spin states absorb light of opposite circular polarisation, so if an uneven population exists different reflectance coefficients will be present for the two polarisation states and the reflected light will undergo a polarisation change which can be related back to the magnetic state of the sample. It was used to measure the magnetic properties of the nanoparticle samples. The technique does not have the extreme surface sensitivity of RAS and its depth penetration is controlled by the wavelength of the optical probe.

Experimentally, the apparatus is quite similar to RAS, and only the addition of a computer controllable electromagnet and some rearrangement of the components is required. Many of the alternative setups mentioned for the RAS are also useable here, but as they all use relatively low modulation frequencies they are not ideal. In the

normally used configuration the PEM is placed in the incident beam, while it normally intersects the reflected beam in RAS. There is also normally a choice of light sources, a Xenon lamp for variable wavelength studies and a laser if hysteresis loops are required. The sample is placed in the magnetic field generated by the electromagnet. This configuration is shown in figure 5.4 (a).

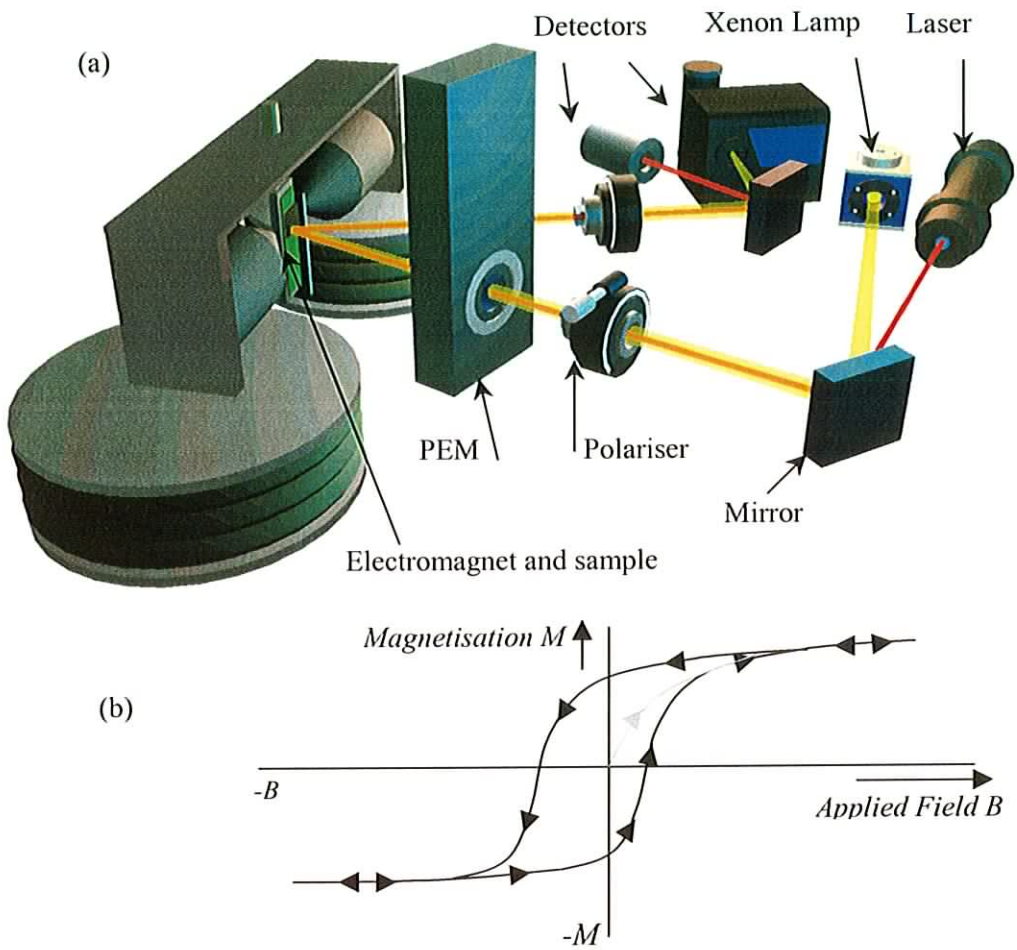

Figure 5.4: MOKE apparatus in longitudinal configuration, components as in RAS with the addition of an electromagnet and a laser (a). An example of a single wavelength, magnetic hysteresis curve is also shown (b).

It is slightly different to the RAS, as the PEM is configured to alternately select two beams of circularly polarised light of different handedness, rather than two linearly polarised beams This is accomplished using appropriate optical component alignment and PEM retardation settings, and results in a reflectance variation due to the alternating handedness at the PEM frequency which can be detected by a lockin amplifier. Both variable wavelength and fixed wavelength scans can be taken, but

fixed wavelength scans using a laser are more common, as hysteresis loops, from which remanence and coercivity can be determined, can be taken with this approach (figure 5.4 (b)). The laser is used preferentially in this configuration, due to its greater intensity, as long as a laser with a suitable wavelength is available.

The apparatus can be configured in three configurations, polar, longitudinal and transverse, shown in figure 5.5. Polar is normally used to measure perpendicularly magnetised samples, longitudinal and transverse to measure in-plane magnetisation.

The Kerr rotation and ellipticity respectively, are defined as

$$\theta_K = \frac{1}{2}(\phi_+ - \phi_-) \quad \text{and} \quad \varepsilon_K = \frac{r_+ - r_-}{r_+ + r_-} \qquad \text{Eq. 5.6}$$

where ϕ_+ and ϕ_- are the phase angles of the right and left hand circularly polarised (rhcp and lhcp) light respectively and r_+ and r_- are the reflectances of rhcp and lhcp.[7]

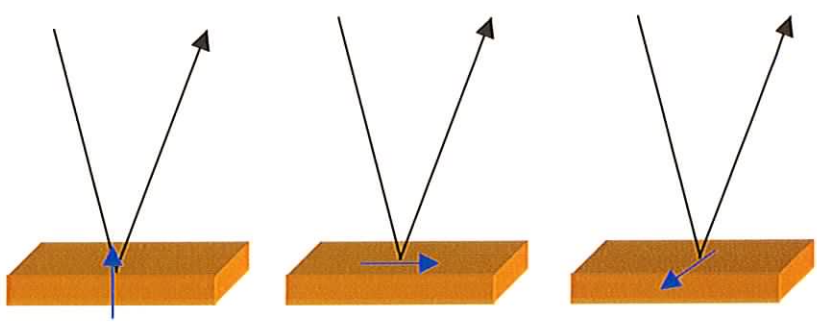

Figure 5.5: Respectively Polar, Longitudinal and Transverse geometries for MOKE instrument setup.

Similar Jones Vector analysis to that used for the RAS equations shows that

$$\varepsilon_K \approx \frac{I(f)}{4J_1(\delta_0)I(0)} \qquad \phi + \theta_K \approx \frac{I(2f)}{4J_2(\delta_0)I(0)} \qquad \text{Eq. 5.7}$$

where *I(0)* is the dc detector signal, *I(f)* and *I(2f)* are the detector signals at frequencies f and 2f, J_1 and J_2 are Bessel functions, ϕ is the angle between the analyser's polarisation axis and the x-axis and δ_0 is the modulation frequency.[6]

It can be shown that the longitudinal configuration in general results in a signal which is one order of magnitude smaller than in the polar configuration. Both longitudinal and polar configurations have a linear relationship with the off diagonal elements of the surface dielectric tensor. The transverse configuration has a signal which is even smaller and is not linear with respect to the off diagonal elements and is therefore not often used. Both longitudinal and transverse forms require a more difficult derivation than the polar setup due to the more complex form of the Fresnel reflectance ratio for these geometries. In all configurations, it is very difficult to obtain a proportionality factor between the Kerr signal and the magnetisation, so the actual magnitude of the Kerr signal is less important than its *maximisation*. The selection of a particular configuration is normally then simply a question of which will give the greatest response given the expected magnetisation state of the system being studied.

5.5 Time Resolved Magneto Optical Kerr Effect (TRMOKE)

The Time Resolved Magneto-Optical Kerr Effect[7] is a powerful technique for probing magnetic dynamics. It is a modification of the MOKE instrument which uses a more powerful laser in a pump-probe configuration, and was also used to probe the magnetic behavior of the nanoparticle samples. The pump beam, which is arranged to be more powerful than the probe, is used to cause a disruption to the magnetic state of the sample. The probe is then used to track these changes as a function of time, and is monitored in the same way as conventional MOKE. The instrument is normally used in one of two configurations.

(i) The heat generated by the laser pulse is sufficient to raise the temperature of the sample temporarily above its blocking temperature (where thermal energy becomes large enough to overcome the energy barrier between easy magnetisation directions), and thereby achieve thermal demagnetisation. The remagnetisation as the sample cools is observed using the probe beam.

(ii) The pump beam may be split into right and left circularly polarised components. These selectively excite different spin states in the sample and the effect of this on the sample magnetisation can be observed.

The interaction of the probe beam with the sample is the same as that for MOKE. The behaviour of the magnetisation upon interaction of the pump beam in this situation is however far more complex and for the most part is not completely understood. In general, there is a four step process to be considered.

(i) The pump pulse excites a non thermal distribution of electrons, which in the presence of an external field, will be spin resolved whether the sample is magnetic or not. The energy distribution of the excited states matches that of the probe beam, as the electrons have not yet had enough time to begin to dephase, $t \approx 10^{-15}$sec.

(ii) Electron-electron interactions distribute energy through the system, beginning a relaxation process toward a thermal distribution. The time frame for this is still much less than the electron-phonon interaction time, $t \approx 10^{-14}$sec.

(iii) Electrons and phonons begin to interact, and the excited electrons decay via phonon cascade, dumping energy into the lattice, $t \approx 10^{-13}$-10^{-12} sec.

(iv) Electrons and phonons reach a common equilibrium, $t \approx 10^{-10}$.

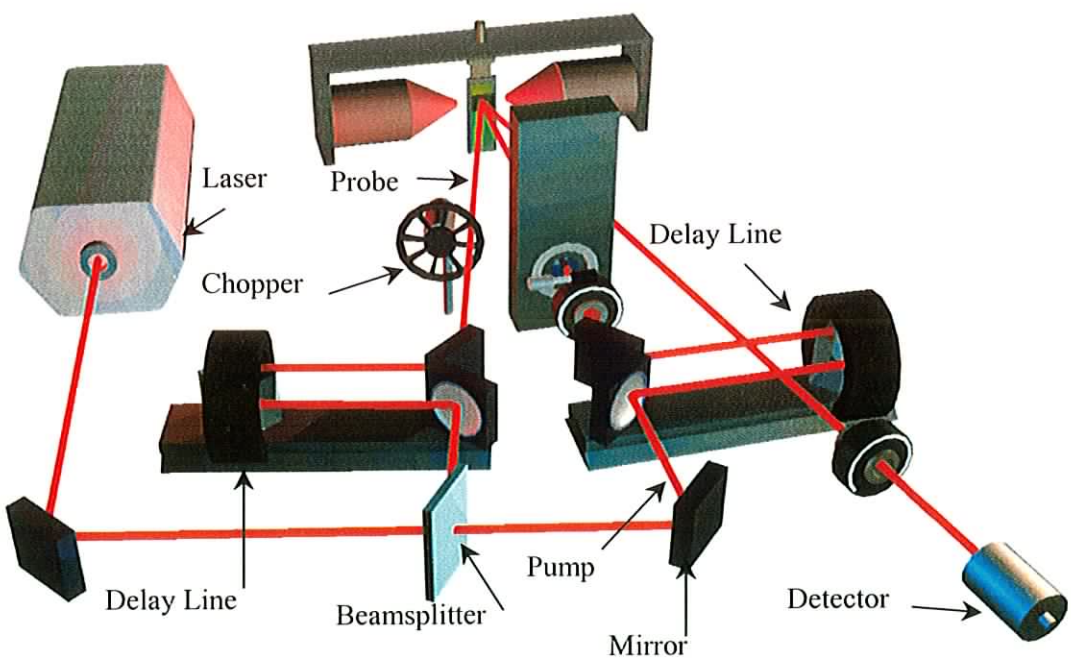

Figure 5.6: Time resolved MOKE setup, showing the addition of the femtosecond laser, delay lines, optical chopper, and a slight component rearrangement.[7] The scattered pump beam is not shown.

The final two steps are quite well understood as it has been relatively easy to investigate those time scales for some time now. The first two steps, in particular the initial demagnetisation, are still the subject of considerable investigation.

For this reason the technique is frequently used in a qualitative fashion, without any direct calculation of material constants based on its measurements. An experimental arrangement is shown in figure 5.6,[7] and a typical spectrum in figure 5.7.[8] This can then be used in conjunction with curve fitting techniques to attempt to explain a systems behaviour.

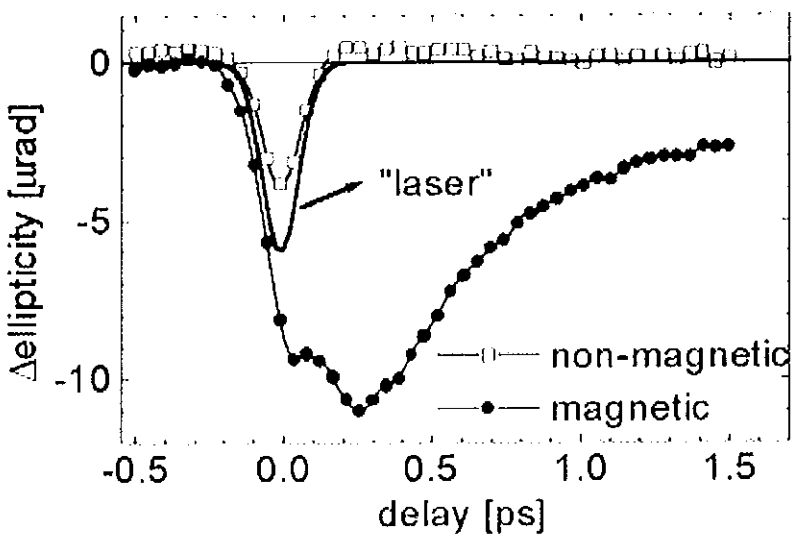

Figure 5.7 An example of a TRMOKE measurement of nickel wedges,[8] showing both magnetic and non-magnetic contributions, obtained from the difference in the up and down response, and average of the up and down response respectively.

Additional components are required in order to construct the instrument from a MOKE. Figure 5.6 shows the two delay lines, which consist of mirrored segments of variable length that move on motorised actuators. An additional chopper is sometimes used on the probe beam to assist in dc signal recovery.

A Jones vector analysis can also be applied here, yielding

$$\frac{V_{ac}}{V_0} = \sin^2\alpha + \frac{1 - J_0(2A_0)}{2}\cos^2\alpha\left|\theta_{MO}(\Delta(t))\right|^2 \qquad \text{Eq. 5.8}$$

$$\frac{V_{1f}}{V_0} = J_1(A_0)\sin(2\alpha)\theta'_{MO}(\Delta t) \qquad \text{Eq. 5.9}$$

$$\frac{V_{2f}}{V_0} = \frac{J_2(2A_0)}{2}\left|\theta_{MO}(\Delta t)\right|^2 \qquad \text{Eq. 5.10}$$

which are the normalised dc, f and 2f signals detected by the lock-in amplifier and ϑ_{MO} is the Kerr rotation. For small α, the angle between the analyser and the lab horizon, equations. 5.9 and 5.10 can be approximated by:

$$\frac{V_{1f}}{V_0} \approx 2J_1(A_0)\frac{\theta'_{MO}(\Delta t)}{\alpha} \qquad \text{Eq. 5.11}$$

$$\frac{V_{2f}}{V} \approx \frac{-J_2(2A_0)}{2}\left(\frac{\left|\theta_{MO}(\Delta t)\right|}{\alpha}\right)^2 \qquad \text{Eq. 5.12}$$

Therefore although almost crossing the polariser and analyser reduces the overall signal the normalised signals are enhanced by a factor of $1/\alpha$. In this configuration, V_{1f} scales with the real part of the complex magneto-optical rotation, while V_{2f} contains some ellipticity information but it is weak.

5.6 X-Ray Photoelectron Spectroscopy (XPS)

XPS,[9] or Electronic Spectroscopy for Chemical Analysis, ESCA, is a commonly used surface analysis technique for determining surface composition. It was used to investigate the surface chemical composition of Co nanoparticles, as Co Mössbauer spectroscopy was not available. X-rays are generated by bombarding a magnesium or aluminium anode with electrons in an x-ray gun. This produces core vacancies that result in x-ray fluorescence. A synchrotron source may also be used as a source of tunable X-rays, which cause the emission of core level electrons from the samples which are emitted from the surface and collected by an accelerating lens. A hemispherical analyser selects electrons of varying energy which are counted in a detector. If the energy of the incident x-rays is known the binding energy of the emitted electron can be found from the Einstein equation:

$$E_{KE} = h\nu - E_B - e\phi$$ Eq. 5.13

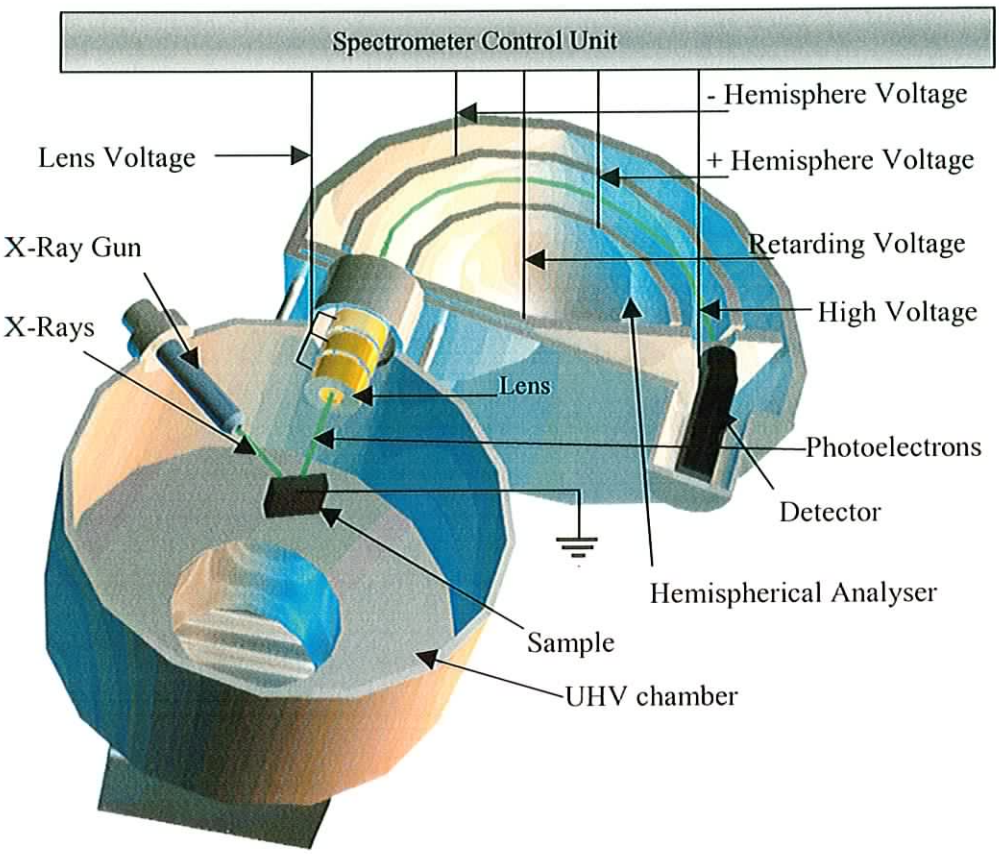

Figure 5.7: An example of a typical XPS set-up using a hemispherical analyser. The energy of the electrons reaching the detector is controlled by the voltages across the hemispherical analyser, which varies the electron trajectories.

where E_{KE} is the kinetic energy of the emitted photoelectron, hν the photon energy, E_B the core electron binding energy and ϕ the work function. The core level electron binding energy is specific to a particular atom so the spectra can be used to determine the chemical composition of a surface.

5.7 Low Energy Electron Diffraction (LEED)

Low Energy Electron Diffraction[9] is a very well documented surface analysis technique and was used to verify the formation of Si(111)-4x1-In quantum wires. Electrons are generated through thermionic emission and accelerated onto a sample.

The accelerating voltage is selected so that the electron wavelength will be sufficiently small to cause diffraction off the crystal lattice of the sample. If there is sufficient long-range order in the lattice periodicity a diffraction pattern will be formed on a phosphorescent screen, and this will be the Fourier transform of the surface lattice.

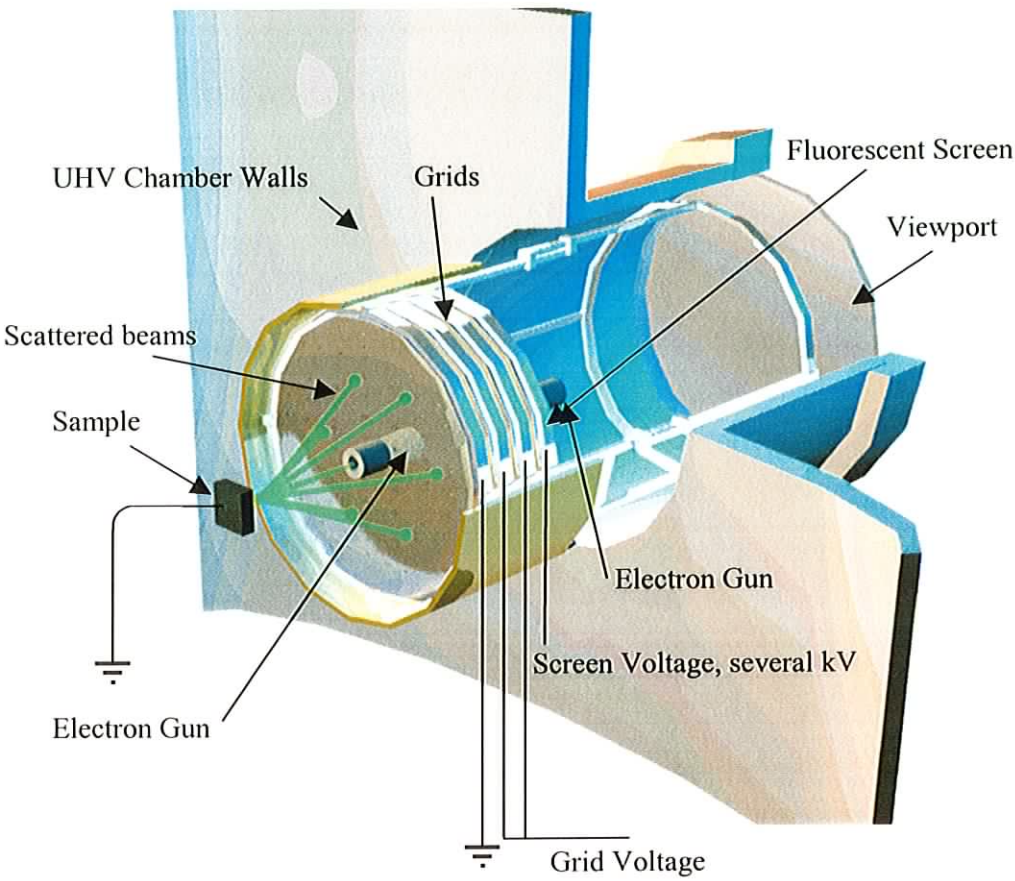

Figure 5.8: Rear view LEED apparatus. Electrons accelerated by the electron gun diffract off the atomic planes in the sample, and produce a diffraction pattern when reflected onto the screen.

It is also possible, given a system of sufficient quality to do detailed analysis of the LEED patterns and spot profiles. This is known as I(V)LEED and is probably the major research use of LEED. In many circumstances the instrument is used simply to identify what, if any, surface reconstructions are present.

5.8 Mössbauer Spectroscopy

Mössbauer spectroscopy[10] was used to investigate the composition of the Fe nanoparticle cores. It allows the detection of specific atoms in a sample and can give some information about their chemical environment. This is accomplished through the excitation of ground state nuclei into excited states by γ-ray photon absorption. The energy range of photons that will excite this state is very narrow, and to achieve a sufficient quantity of photons in this energy range excited nuclei of the same isotope as those being examined are used as the source. This can limit the application of the technique somewhat, as, in order to look for iron, for example, a sample of irradiated iron must be used as the γ-ray source. The recoil of the nuclei on emission has negligible effect on the photon energy and resonant absorption can take place.

The primary absorption level can be split or shifted by isomer shifts, quadrupole interactions and hyperfine splitting. In order to identify these effects the energy of the incident photons needs to be varied. Fortunately, the energy shifts are normally quite small and a sufficient energy variation can be obtained by Doppler shifting the photons by vibrating the source on a slider. This setup is shown in figure 5.9.

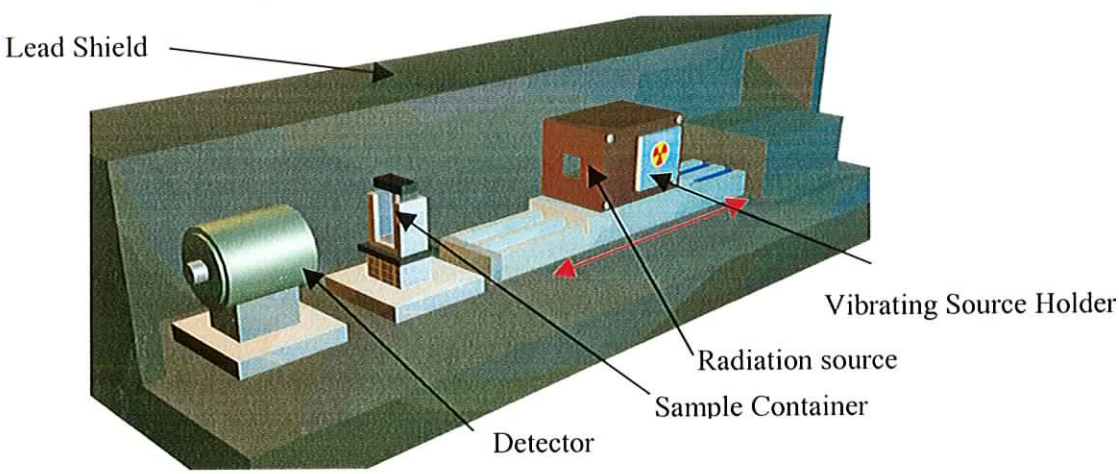

Figure 5.9: An example of a typical Mössbauer spectrometer. The slight doppler effect induced energy shift caused by the oscillating source holder is sufficient to scan around the absorption region of the sample.

5.9 Superconducting Quantum Interference Device Magnetometry (SQUID)

Superconducting Quantum Interference Device Magnetometry[11,12] is a very sensitive technique for the detection of magnetic moments. It was used to examine the magnetic properties of the Co nanoparticles. Unlike MOKE, however, it measures the

response from the whole sample, not just a portion of the surface. A sample is placed into a superconducting loop that is broken by two layers of insulator, called Josephson junctions, which can be produced by photolithography. In practice the superconducting wire arrangements can be more complex than that shown schematically below.

When a bias current (Ib) is applied to the SQUID, voltage across the SQUID is zero if the current is less than the critical current (Ic). If the bias current exceeds the critical current, the SQUID ceases to be superconducting and voltage is produced. When a magnetic flux is introduced into the SQUID loop, the value of this critical current decreases.

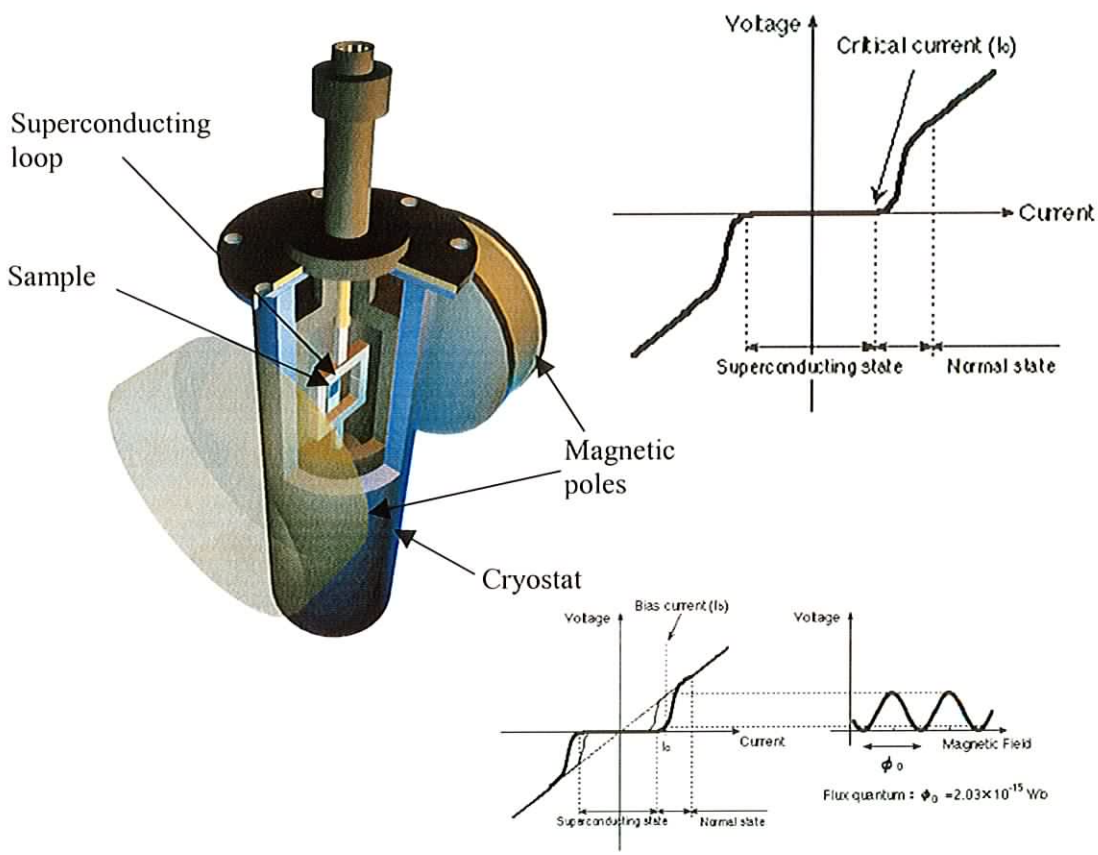

Figure 5.10: Representation of a Superconducting Quantum Interference Device Magnetometer in a cryostat, allowing temperature dependent measurements. The superconducting loop can have a more complex arrangement that that shown here. The insets show the current-voltage characteristics of the loop.

When the bias current is fixed at a slightly higher value than the critical current and an external magnetic field is applied, the voltage will change in a periodic wave in accordance with the flux quantization. The number of oscillations in this voltage

gives a direct count of the flux quanta passing through the SQUID loop, from which the total magnetic field can be calculated.

5.10 References

[1] H. K. Wickramasinghe, Acta Mater. **48** 347 (2000)

[2] R. Wiesendanger, H. J. Guntherodt, editors, Scanning Tunneling Microscopy III: Theory of STM and Related Scanning Probe Methods (Springer Series in Surface Sciences, No 29)

[3] www.di.com/

[4] www.omicron-instruments.com/

[5] P van der Heijden, Magnetic properties of oxide-based thin films and multilayers, Ph.D. Thesis, 1998, http://alexandria.tue.nl/extra2/9800645.pdf

[6] J. Kerr, Phil. Mag. 3, 339, (1877)

[7] e.g. B. Koopmans, M. Van Kampen, J. T. Kohlhepp, W.J.M. de Jonge, Phys. Rev. Lett., **85**, 844, (2000) *and references therein*

[8] http://www.phys.tue.nl/fna/research/ultra.htm

[9] e.g. M. Prutton, Introduction to Surface Physics, Clarendon Press, 1994

[10] e.g. http://www.webres.com/mossbauer_spectroscopy.html

[11] R. L. Forgacs A. Warnick, IEEE. Trans. Instrum. Meaa. IM-15,113 (1966).

[12] F. Wellstood, C. Heiden, J. Clarke, Rev. Sci. Instrum. 55, 952 (1984).

Chapter 6

Indium on silicon

As mentioned in the introduction, one-dimensional and quasi one-dimensional metals have been attracting interest for a variety of reasons. Not only do they have interesting electronic properties which could be useful for optoelectronic and magnetic devices, but they also present a challenge to theoreticians, as the expectations of current theory is not always matched by experimental results. In this chapter two candidate structures, consisting of indium induced reconstructions on Si (111) and (100) surfaces, are investigated using RAS and STM for signs of quantum confinement, an essential ingredient for a one-dimensional metal.

6.1 One-Dimensional Metals.

A conventional three-dimensional metal is described as a nearly free electron gas, where the lattice atoms cause a periodic variation in the otherwise uniform potential that the electrons would feel. When a function describing this potential is substituted into the Schrödinger equation and solved, it results in a generally parabolic dependence of E, the electron energy with k, the electron propagation wavevector. The periodic potential has the effect of introducing forbidden energies or band gaps, and this results in the familiar E vs. k band structure, as shown in figure 6.1.

A key factor here is that although the electrons are strongly interacting their correlation is presumed to be relatively weak. This results in the widely used Fermi liquid model. It can be shown that Fermi liquid behaviour is truly possible only in three- and two-dimensional materials, however.[1] In one-dimensional systems, the electron correlations become more effective, resulting in collective charge and spin density oscillations. The experimentally observable properties of such systems should be significantly different in origin to those of their higher dimensional relatives. Despite this, many quantum wire systems display properties more closely comparable with a one dimensional Fermi liquid.[2]

Theoretical descriptions of strongly correlated electrons are daunting, and exact solutions of these systems are rarely possible except in low energy regimes, where there is a variety of solvable models. One particularly applicable description is the Luttinger-Tomonaga model, which has yielded much success. Such systems are therefore generically called Luttinger liquids[3] as they display non-Fermi liquid behaviour,[4] such as

1. A linear, continuous E vs. k dispersion with no band gaps.

2. Spin-charge separation, where an injected electron seems to split into separate spin and charge quasiparticles, which then disperse with different velocities.

This is a satisfactory theoretical description of a one-dimensional material, but its application to real systems has been problematical. The observable quantities do not always differ too much from those of Fermi liquids and various effects can destroy the quasi one-dimensionality of candidate systems, such as inadequate confinement or coupling between neighbouring parallel conductors or the substrate. Strong spin-orbit coupling can also destroy the effects. In addition, the Peierls distortion, mentioned in the introduction, can be an impediment to the achievement of one-dimensional conductivity. Overall, this has made it difficult to directly observe Luttinger liquid properties and the reconciliation of experimental results and theoretical expectations still represents a challenge.

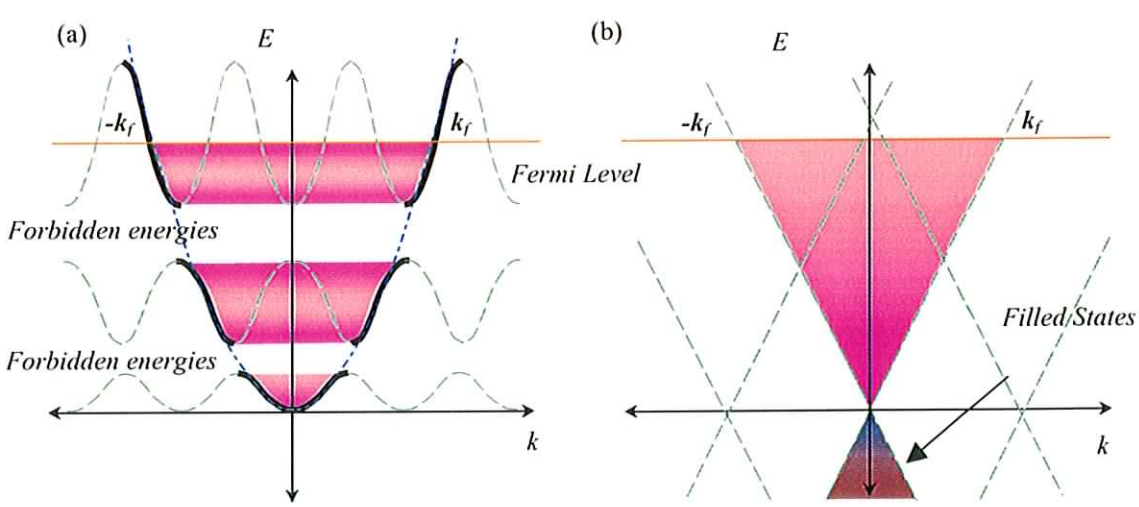

Figure 6.1: Comparison of (a) Fermi and (b) Luttinger liquid dispersions. Notable differences are the linear dispersion and the absence of band gaps in the Luttinger liquid.

A full description of Luttinger liquid behaviour and the challenges in observing it in real systems is beyond the scope of this work. The focus here is on electron confinement, a key requirement of a one-dimensional metal. Some materials, such as carbon nanotubes, achieve this due to the presence of the surface of the structure. Otherwise, a suitably strong confining potential in a two- or three-dimensional structure is required. Recent calculations have shown that the effects of the confinement barriers can be considerable and that the inclusion of accurate potential barriers in theoretical descriptions may resolve some differences between experiment and theory.

It has been demonstrated that deposition of indium onto silicon surfaces under UHV conditions can cause reconstructions that seem to resemble wires in STM images,[5] especially on the Si(111) and Si(001) surfaces. An example of these wire-like structures is shown in figure 6.2. This wire-like structure however, does not guarantee either one dimensionality or conductivity. The confinement is therefore investigated, on the premise that an anisotropic electronic structure, if present, will result in an anisotropic optical response that the RAS should be able to detect. Previously, RAS of the Si(111)-5x2-Au system, which also consists of wire-like structures stretching across the surface, demonstrated a strong optical response.[6]

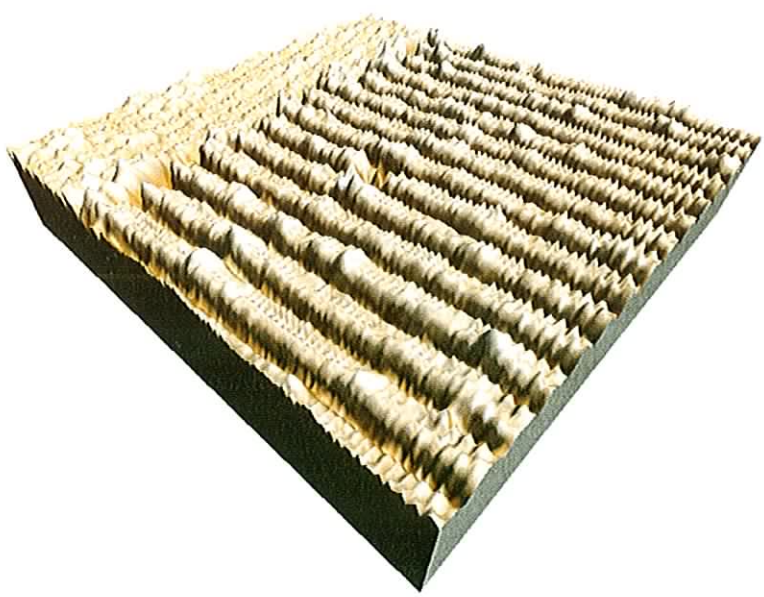

Figure 6.2: Preliminary 22nm x 22nm STM of two intersecting domains of indium wires on the Si(111) surface, obtained during Si(111)-4x1-In experiments. The domain distribution can be improved for RAS work by appropriate thermal treatment of the surface. The sample-tip bias was +1.2V, and feature height ~.8Å

6.2 Indium on Si(111)

6.2.1 The Silicon(111) Surface

Silicon atoms have the electronic configuration $1s^2 2s^2 2p^6 3s^2 3p^2$. The four occupied valence orbitals hybridise to form four sp^3 hybrid orbitals, which gives bulk silicon a tetrahedral structure, similar to bulk carbon in diamond form. When this structure terminates in a (111) surface, assuming no other factors at present, it would appear as in figure 6.3, which also shows a step on the surface. However, the break in symmetry at the surface will have a consequent effect on bonding causing the surface atoms to relax somewhat from their expected bulk positions. Also, each top layer Si atom has a dangling bond that contains one electron and is therefore highly reactive.

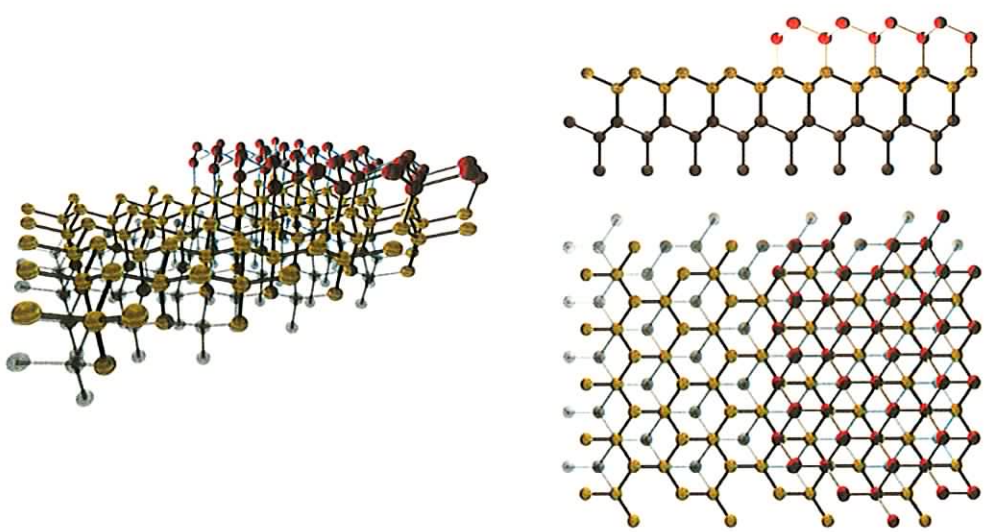

Figure 6.3: Unreconstructed Si(111) surface showing tetrahedral structure and steps.

Under normal circumstances, these bonds would be terminated by an adsorbed impurity, such as oxygen or hydrogen. During cleaning in UHV conditions, these atoms desorb and the dangling bond structure is regenerated. It can be shown using energy considerations that it is very favourable for this surface to reorganise itself into a more stable configuration. There are two reconstructions that generally result, the 2x1 and the 7x7. The preparation required for the experiments in this chapter results in the formation of the 7x7, shown in figure 6.4. The 7x7 structure, known as the Dimer Adatom Stacking Fault (DAS) structure,[7] is highly complex, and has been described elsewhere in more dedicated studies. That information is not of great

relevance here, simply that the presence of adsorbed impurities generally destroys it, therefore its appearance on a LEED display is an indicator of general surface cleanliness. In order to generate well ordered single domain reconstructions of sufficiently large area such cleanliness is crucial.

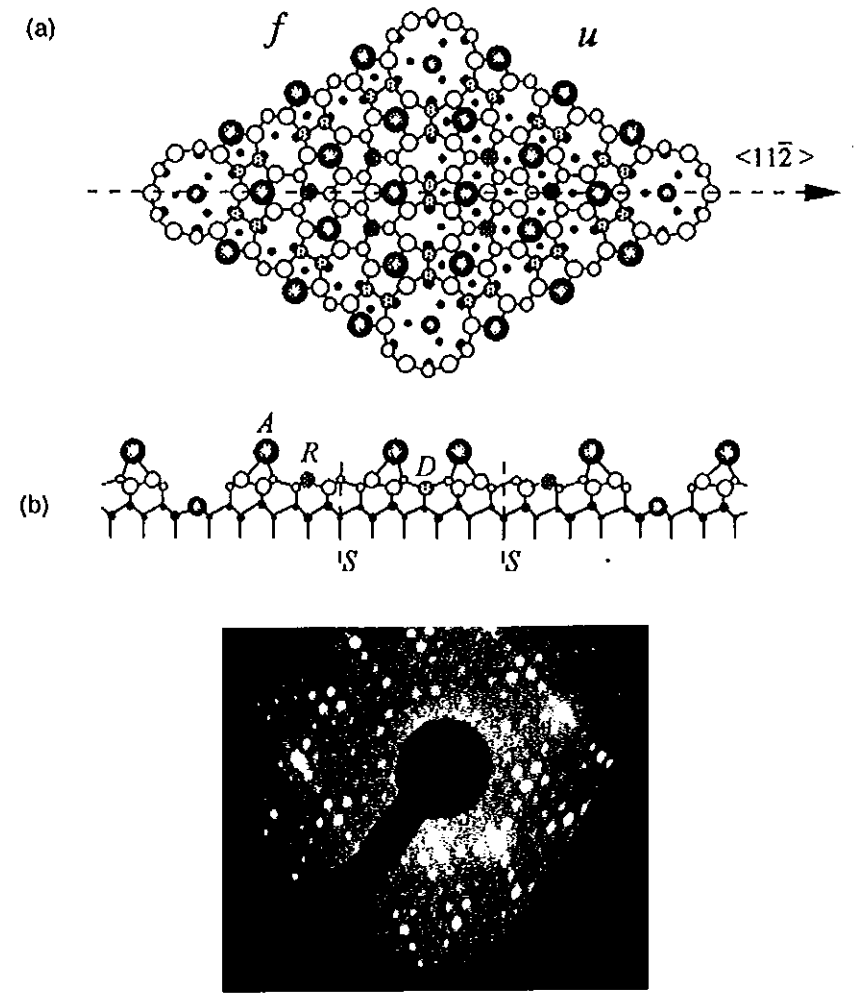

Figure 6.4: The Dimer Adatom Stacking fault (DAS) model of the SI(111)7x7 reconstruction[7] and a LEED image showing the 7x7 pattern taken during RAS experiments. The LEED image did display spot-splitting, but this is not apparent in this image due to resolution problems with the CCD camera.

6.2.2 Indium-Induced Reconstructions of the Si(111) Surface

Metal atoms can be deposited onto a surface using a variety of methods, for example wire evaporation, sputtering, etc. In this case, a Knudsen cell evaporator was used. This generates a flux of atoms or ions, which, if properly directed, will coat the substrate and may induce surface reconstructions. In the case of indium on the Si(111) surface, many reconstructions are possible, with dependencies on In coverage and

substrate temperature before or after deposition. Figure 6.5 is a brief list of some of the possible reconstructions. They were investigated by Kraft, et al,[8] and more information may be found there.

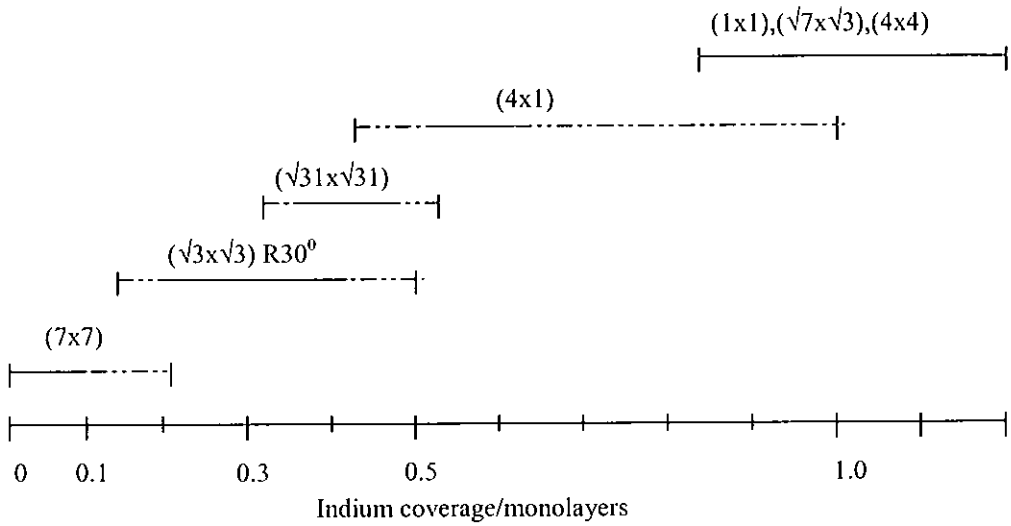

Figure 6.5: Diagram depicting the various reconstruction of In on Si(111) for temperatures of 400-550^{0}C.

As the Si(111)-4x1-In system was found by STM to be composed of parallel wire-like structures,[5] this was investigated further.

6.2.3 The Si(111)-4x1-In Reconstruction

The 4x1 reconstruction has been the subject of many investigations in recent years, using LEED,[9] ICISS,[5] PES,[10] XRD,[11] AES,[9] STM,[5,12] and HREELS.[13] There is still confusion over its physical structure, despite the excellent recent STM data[12] and XRD.[11] There are two available models which fit most, but not all, of the available data. The first was proposed by Zotov, Saranin, et al.,[14] and is shown in figure 6.6(a). It consists of parallel In rows, three atoms wide. The central In row is bonded metallically to the edge row atoms, and the edge row atoms are covalently bonded to the Si substrate which displays a Pandey type reconstruction.[15,16] In between the In rows there is single zigzag chain of Si atoms, which was added to meet surface Si coverage requirements. The second was proposed by Bunk, et al.,[11] figure 6.6(b). This

also consists of a zigzag Si chain, which is covalently bonded to two zigzag In chains, one on either side of the Si chain. The In chains also bond covalently with the substrate, which is unreconstructed in this case.

The existing information was insufficient to preferentially select one model, but two recent studies attempted to shed light on the situation. The first study showed that the system undergoes a Peierls-like distortion at low temperature,[17] forming an 8x2 reconstruction, which was initially believed to be driven by the formation of a Charge Density Wave (CDW).

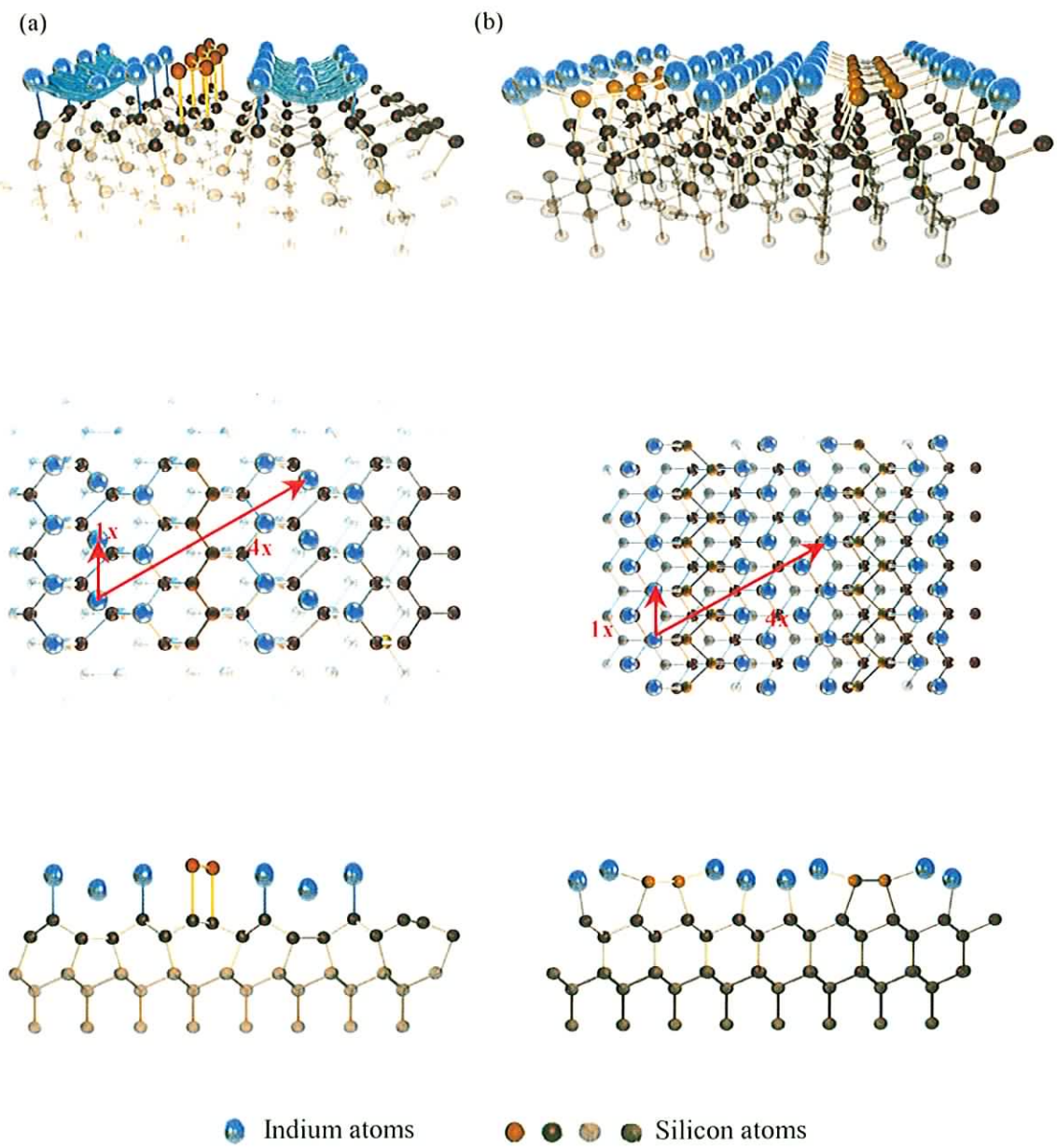

Figure 6.6: Competing structures for Si(111)-4x1-In: (a) Saranin, et. al.[14] (b) Bunk, et. al.[11]

This would seem to favour the Zotov, Saranin model as the purely metallically bonded indium atoms of the centre row would have a relatively large freedom towards displacement. The Bunk model could find it more difficult to distort at low temperatures, as the covalent In-Si bonds should have less freedom to move.

Zotov[12] also proposed a modification to Bunks model, removing the edge row In atoms that are bonded to the Si substrate bonds and replacing them with a single In row, metallically bonded to the inner In atoms, which, as with Zotov's original model should more favourably undergo a low temperature Peierls-like distortion. Bunk, et al, then attempted to explain this distortion in the context of their original model, by way of a positional distortion along a glide plane that they identified using SXRD.[18] This investigation cast doubt on the CDW theory, as it showed that the distortion does not form completely over the surface, rather forming domains of the distortion with are strongly correlated perpendicular to the chains but more loosely correlated parallel to the chains. This does not improve as the temperature is dropped from 100K to 20K, but it would be expected to, as the CDW became more dominating. This implies that the CDW formation was not the primary driving force in this rearrangement, and that instead it may be simply be a caused by a reduction in free energy due to the surface restructuring. A recent HREELS study also cast doubt on the CDW theory.[13]

In addition, electronic structure calculations by Nakamura, et al,[19] performed using the coordinates obtained from the Bunk XRD experiment produce a band structure that agrees well with the established photoemission data, while the same calculations performed at the Zotov model do not. This is the most compelling evidence in favour of Bunks model, and it is now almost taken for granted that this is the true picture, although more work, especially band structure and energy calculations, needs to be done to understand the low temperature transition. In order to further clarify the room temperature structure, STM experiments were performed in an attempt to obtain physical evidence to back up the band structure calculations.

6.2.4 STM of Si(111)-4x1-In

The STM and STS experiments were performed on pre-cut and polished p type Silicon in an Omicron Variable Temperature UHV STM with a base pressure of $2x10^{-11}$ mbar. The silicon was prepared in the preparation chamber and degassed over night at ~600^{0}C by resistive heating. After cooling, the samples were flashed to 1240^{0}C by direct current heating several times, followed by a 10 second flash to 1240^{0}C, quenched to ~900^{0}C and allowed to cool slowly to room temp, over approximately 10 minutes. The sample temperature was checked at all stages using an optical pyrometer. Pressure was kept below $3x10^{-10}$ mbar during sample preparation. The preparation of single height steps was not too important due to the small area requirements of STM, and multidomain samples can sometimes prove useful by effectively allowing scans in multiple directions at once, without having to change the scan direction. The treatment effectiveness and surface cleanliness were examined using LEED and STM, figure 6.7, which showed the 7x7 reconstruction expected from clean Si(111). This STM image was obtained using the documented settings for imaging the 7x7 reconstruction, which were supplied by Omicron.

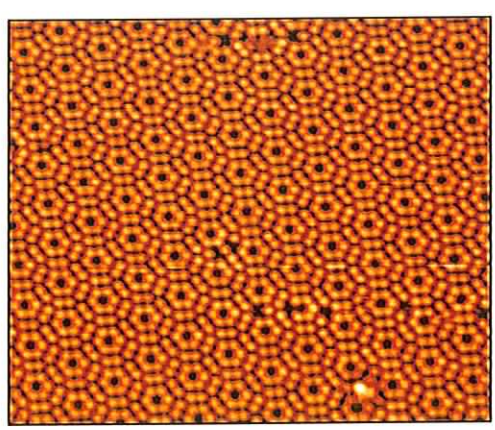

Figure 6.7: STM image of clean Si(111) surface clearly showing the expected 7x7 reconstruction.

Indium was deposited using a Knudsen cell (K-cell) evaporator. This was attached to an exposure meter that had been calibrated during previous experiments with the UHV system. 0.75 monolayers were deposited, as this was expected to be sufficient to form the 4x1-In reconstruction.[8] The samples were examined using LEED which verified the presence of a multi-domain 4x1 reconstruction (e.g. figure 6.15). This structure persisted for beam energies between 50eV to 100eV, indicating good long range ordering. The samples were then transferred into the STM. Scanning normally

began immediately, although it sometimes took approximately 45 minutes for the distortive effects of thermal drift to reduce to acceptable levels. The software automatic drift correction was used to stabilise the instrument for repeated scans. The initial scans produced images similar to figure 6.2, which showed a clear wire structure with an inner furrow, but no internal structure. This had been seen previously.[5] The tip sample bias voltage and current setpoints were adjusted to optimise the image. Figure 6.8 shows a topographic image taken with a sample bias of +1.2V with respect to the tip and plane flattened. All subsequently stated tip sample biases will also refer to the sample bias with respect to the tip. This is a 50nm x 50nm scan showing long, ordered regions of parallel wire growth. The lower region also shows arrays of dot like structures. These were found to form at low indium coverages, after excessive thermal annealing or after the sample were left unattended for long periods, ~1 day, by which time the wire like structures had almost disappeared. The dots are probably due to low density indium coverage decorating the underlying substrate. As they were not directly relevant to this work they were not investigated further.

Larger area scans were used to investigate the coverage of the surface and the domain distribution, although this is not important for the STM work. The silicon used here had relatively small terraces, averaging approximately 50nm, which limited wire growth, as they seemed to require terraces above a certain minimum size for successful nucleation. It was found that the normal flashing and depositions in the experiment were sufficient to widen the terraces by approximately 20nm. Any additional flashing cycles on top of these caused too much damage to the surface.

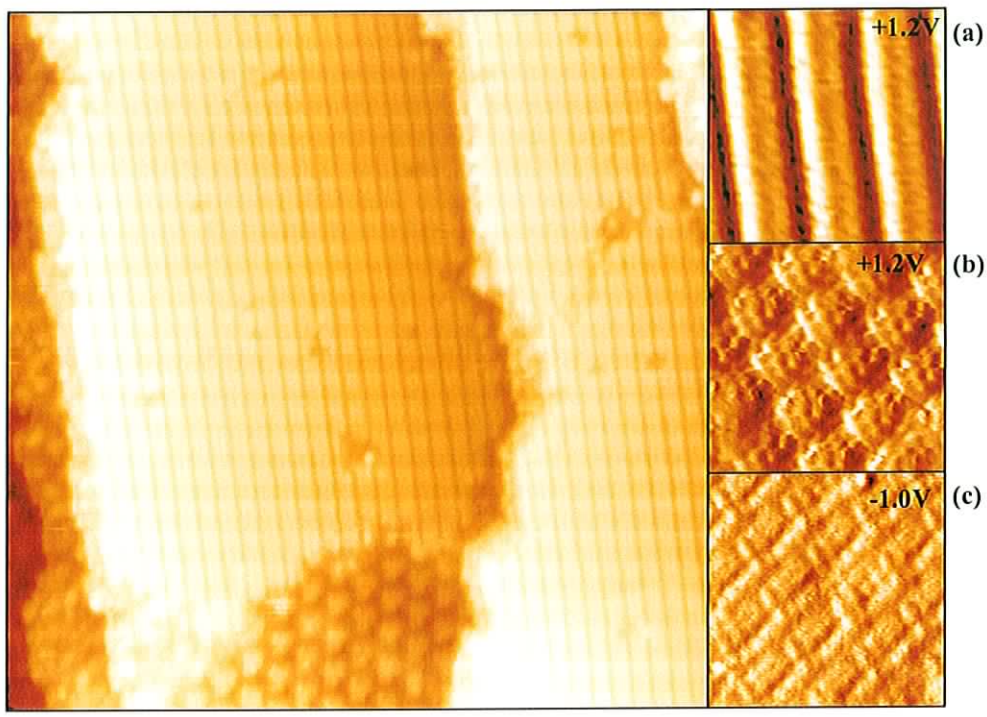

Figure 6.8: 50nmx50nm STM image of Si(111)-4x1-In wire structures, obtained at a bias of +1.2V. The insets show (a) a close up region of the wires, 10nm x10nm, also at +1.2V and (b) and (c) In dot structures at 10nm x10nm and biases of +1.2V(b) and –1.0V(c), believed to be a low coverage decoration of the underlying Si, possibly the $\sqrt{31}x\sqrt{31}$ structure. The orientational differences are due to drift changes. All biases refer to sample with respect to tip.

In order to examine the wires' internal structure, smaller, slower scans were obtained. These can only be obtained after the sample has cooled sufficiently that thermal drift is very small. Examples are shown in figure 6.9, also a dual mode scan, at +1.0V and –1.0V, flattened and drift corrected. The empty state image appears to show greater electron localisation. The horizontal lines on the image are believed to be In-Si bonds.

In an attempt to improve clarity, scans were taken in different directions. Figure 6.10 shows a series of wires scanned at 120 degrees to those in figure 6.9. This image was filtered to reduce noise, and shows more clearly the internal structure of the wires. This structure strongly resembles the Bunk structure.

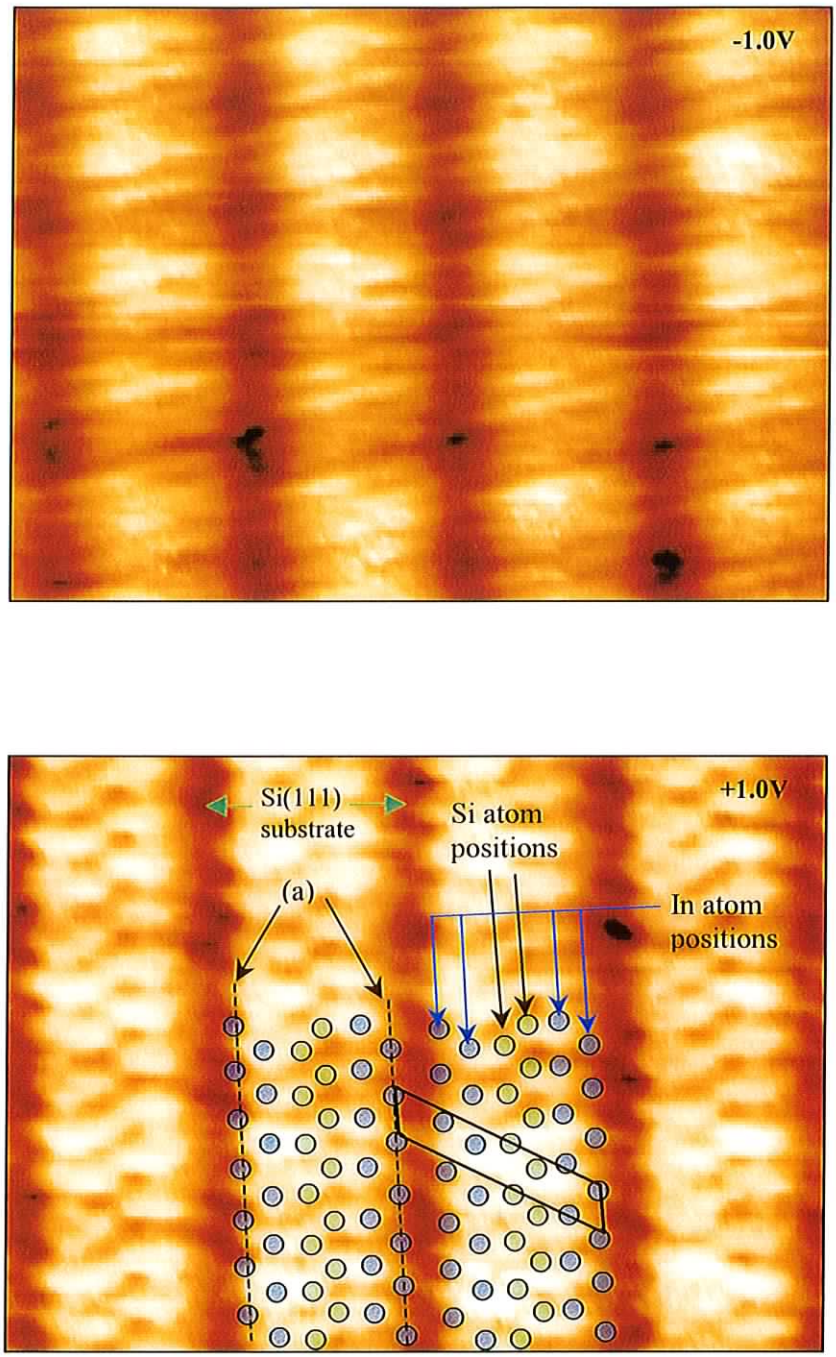

Figure 6.9: Filled and empty state images (-1.0 and +1.0 volts respectively) of In wires. Image dimensions are 6.1x5nm. Expected positions of In and Si atoms are shown as a semitransparent overlay, with a 4x1 unit cell. The unit cell dimensions, from this image, are ~4Å (1x- direction) and 1.6nm (4x- direction) The edge In atoms (a) that bond to the Si substrate appear very dim. This may be due to electron density being pulled into the In-Si substrate bonds.

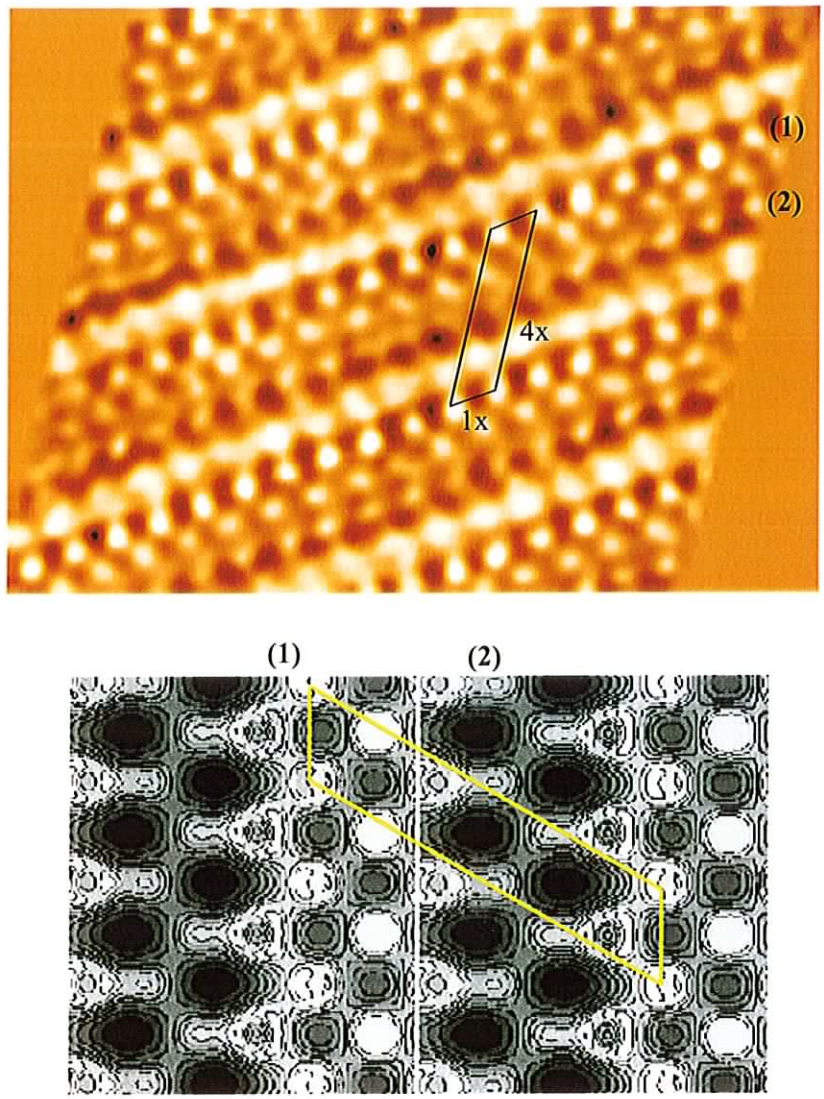

Figure 6.10: A flattened and filtered STM image of the In wires(a), which is compared structurally to the calculated valence charge density map from Nakamura, et al (b). The distortion in the STM is probably due to slight errors in the drift correction. Nevertheless, there is a strong similarity between the two images. The calculations also seem to suggest the slight difference in intensity between different sides of the wire. (sides (1) and (2) above), with the sides appearing to have a slightly different charge density. The 4x1 unit cell is again indicated.

Figure 6.10 also shows a calculated valence charge density map, from the calculations performed of Nakamura, et al.[19] The structure of this image, and that of Bunks original ball and stick model, compares very well with the STM data obtained here for this system. A 4x1 unit cell is shown in both images in figure 6.10 for illustration. There is a slight distortion, probably due to imperfect drift correction. The charge density seems to indicate a reduction in density on the Si zigzag, whereas the apparent Si zigzag in the STM image is quite intense. This may be due to the presence

of a state at the tunnelling voltage, +1.0V, on the Si rows that is obscured in the valence charge density image. Despite this discrepancy, the similarity between the valence calculations the STM images is further strong experimental evidence to support the Bunk model.

6.2.5 STS of Si(111)-4x1-In

Scanning tunnelling spectroscopy was also performed on the system, using the same conditions as the STM measurements, in order to look at the electronic structure of the wires. Figure 6.11 shows spectroscopy from –3.0V to +3.0V.

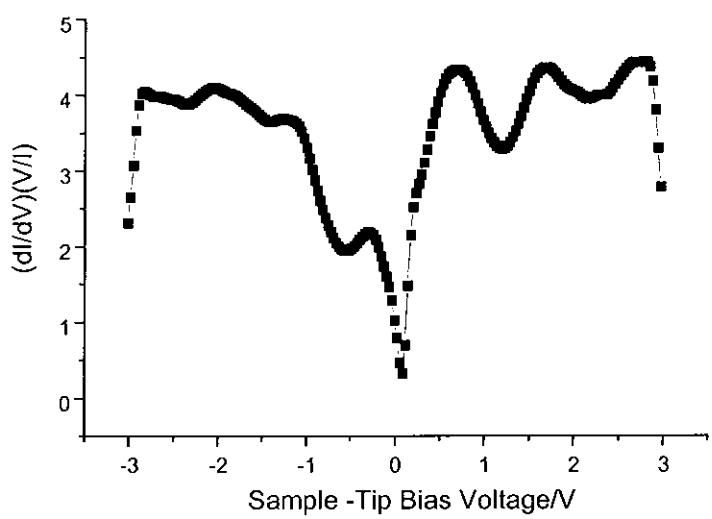

Figure 6.11: STS of Si(111)-4x1-In.

This shows three empty states between 0 and +3V, centred at 0.75V, 1.75V and ~2.7V. These peaks are quite well defined and reproducible across the surface. The filled state features are less distinct, although some features may be apparent at –0.4V, -1V and –2V.

Figure 6.12 shows the band structure for the surface calculated by Nakamura, from Bunk's model. It is difficult to do a direct comparison between E/k band structure and STS, as E/k plots show resolved energy vs. wavevector information,

while STS shows Density of States (DOS) vs. E, where the DOS has contributions from every state at that energy, regardless of wavevector. It is possible nevertheless to make some general statements of comparison. As the tunnel current depends on the density of states at a particular energy, the STS may then be loosely compared to a compacted form of the band structure, with all k states 'integrated' with respect to energy. The greater the number of k states at a given energy, the greater the STS response at that energy. To a visual inspection then, the flatter the E/k curve the greater the number of states at that energy and therefore the greater the intensity. In figure 6.12, the flatter parts of the band structure are highlighted using green lines.

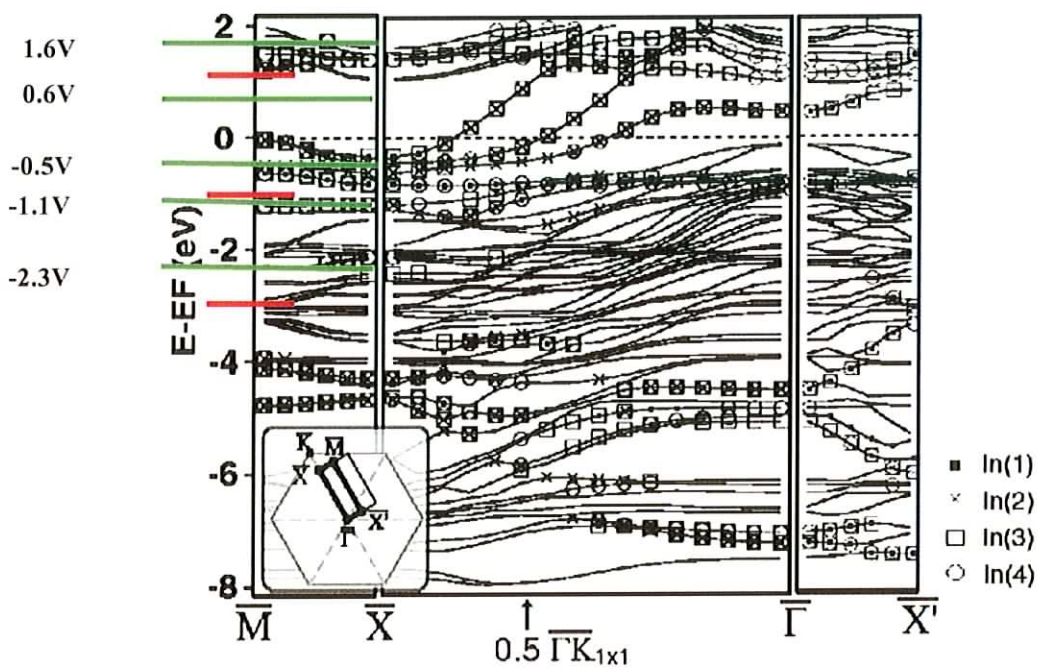

Figure 6.12: Calculated band structure from Nakamura, et al[13].

This would appear to indicate that STS intensity spikes should be found at -2.3V, -1.1V, -0.6V, 0.5V and 1.6V. This is qualitatively in quite good agreement with the actual STS data. This will be compared to the measured bandstructure (from Abukawa, et. al.[22] and Hill, et. al.[23]) and the RAS later.

6.2.6 RAS of Si(111)4x1-In

The RAS experiments were performed on Boron-doped p-type vicinal Si(111) from Wacker Chemical, polished 4^0 off the [111] direction towards [$11\bar{2}$] under ultra high vacuum with a base pressure of $4x10^{-11}$ mbar. Degassing and cleaning conditions were identical to those of the STM experiments, with additional thermal treatment to generate a regular array of single height steps following procedures in O'Mahony, et al.[20] Surface cleanliness and step formation was checked using LEED, which showed a sharp 7x7 spot pattern and energy dependent spot splitting, a characteristic of stepped surfaces.

A Knudsen cell evaporator was again used to deposit In onto the clean surface which was held at 400^0C. No exposure meter was available, therefore the K-cell was calibrated using LEED to confirm the presence of the 4x1 structure. Deposition times were extended in ten second steps until the 4x1 pattern saturated, which happened at approximately 200 seconds. This then corresponds to approximately 0.75 monolayers.

The In deposition was also followed with single wavelength RAS at 1.9eV. This wavelength was chosen as it is believed to be a characteristic of In-Si bonding.[21] The result is shown in figure 6.13. Deposition began at 20 seconds.

There is an initial positive increase in RAS which saturates at 110 seconds (a), followed by a substantial negative peak at ~200 seconds (b). The anisotropy then decreases slightly up to ~250 seconds (c), and remains constant thereafter.

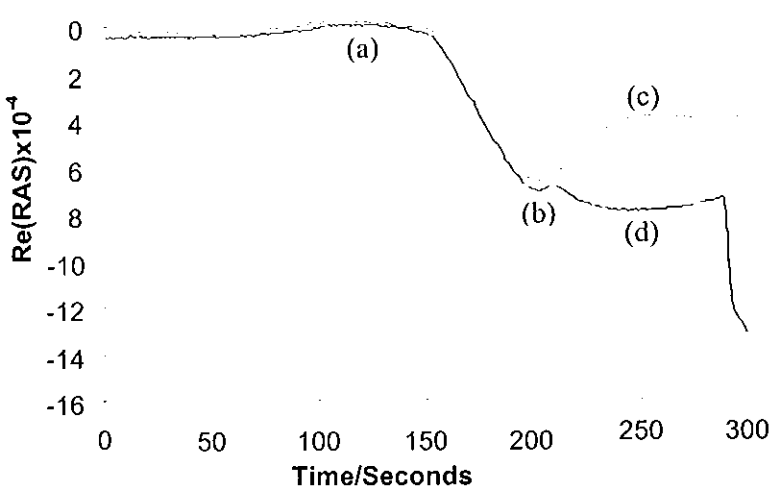

Figure 6.13: RAS of In deposition, with the shutter closed after different deposition times. The red curve was obtained with indium deposition continuing after the evolution of the peak at (b). For the blue curve, In deposition was terminated at (b)

The sample was cleaned and the deposition was repeated. In this case, the In deposition was halted at saturation of the negative peak at ~200 seconds. The RAS initially decreased as previously, but this was followed by an increase in peak height, which was unexpected (d). Further investigation suggested an explanation for this, which will be presented later.

RAS of this surface as a function of photon energy is shown in figure 6.14, along with RAS of the clean surface. The clean surface shows small features at 3.4 and 4.2eV which are bulk related, corresponding to transitions across the direct silicon bandgap. The slight anisotropy of the stepped surface, which is otherwise isotropic, allows these features to contribute the RAS signal.[6]

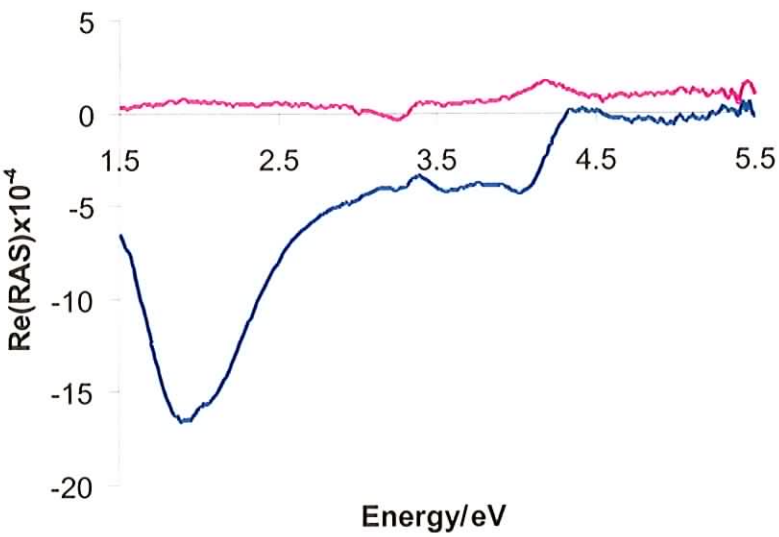

Figure 6.14: RAS of Si(111)4x1-In dominated by large feature at 1.9eV (blue curve). This is believed to be characteristic of In-Si backbonds. RAS of the clean Si(111) surface is also shown (purple curve)

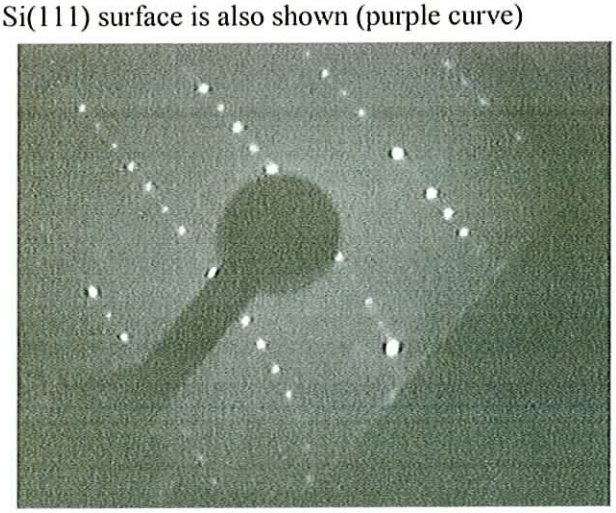

Figure 6.15: LEED pattern showing single domain 4x1 pattern on the Si(111) surface.

RAS of the indium surface shows a large change from the clean surface, consisting mainly of a feature at 1.9eV with an amplitude of 1.65%, which is one of the largest signals detected from well ordered structures on semiconductor surfaces to date, and almost three times larger than the Si(111)5x2 Au system.[6] LEED of this surface, shown in figure 6.15, confirmed a 4x1 structure. The geometry of the system was such that the positive RAS direction was along the apparent In chain direction. This indicated that the feature was due to an optical transition in a state perpendicular to the chains. Compared to some RAS spectra, the feature is also quite narrow. This narrowness and the intensity suggest that at least one of the states involved has a relatively flat dispersion and that the initial state is highly populated.

The exact origin of this feature is unclear. Photoemission spectroscopy from Abukawa, et al,[22] mapped the surface electronic structure and an initial state meeting the requirements above was found. Figure 6.16 shows surface states below the Fermi level parallel and perpendicular to the chain direction. They show a completely filled band, d, ~1.0eV below the Fermi level, whose dispersion is flat perpendicular to the chains but has a notable dispersion parallel to the chains. This could be the initial state in the transition, and has been assigned to bonds between the Si dangling sp^3 hybrid bonds and In valence electrons from the edge In rows. Although these band assignations were based on a surface model which has now been superseded, it remains in good agreement with the models of Saranin and Bunk, which also predict Si sp^3–In bonds and metallic In-In rows. The metallic character of the surface was also verified by Hill's IPES data,[23] shown in figure 6.17 which showed Fermi level crossing parallel to the In chains. The IPES spectra shows an empty state centred at 2eV above the Fermi level, which also has flat dispersion perpendicular to the chains and could therefore be the final state in the transition, although this state has not been assigned to a particular surface feature. A transition between these two states would have an energy of approximately 3eV however, so one of these suppositions is wrong. As there is no 3eV feature present, it is possible that this transition is symmetry forbidden, while a transition from state d to some state at approximately 1eV above the Fermi level is allowed. Alternatively, this could be a transition between some states at the Fermi level and the 3eV IPES feature, although neither photoemission of IPES indicate any intensity at the Fermi level perpendicular to the wires.

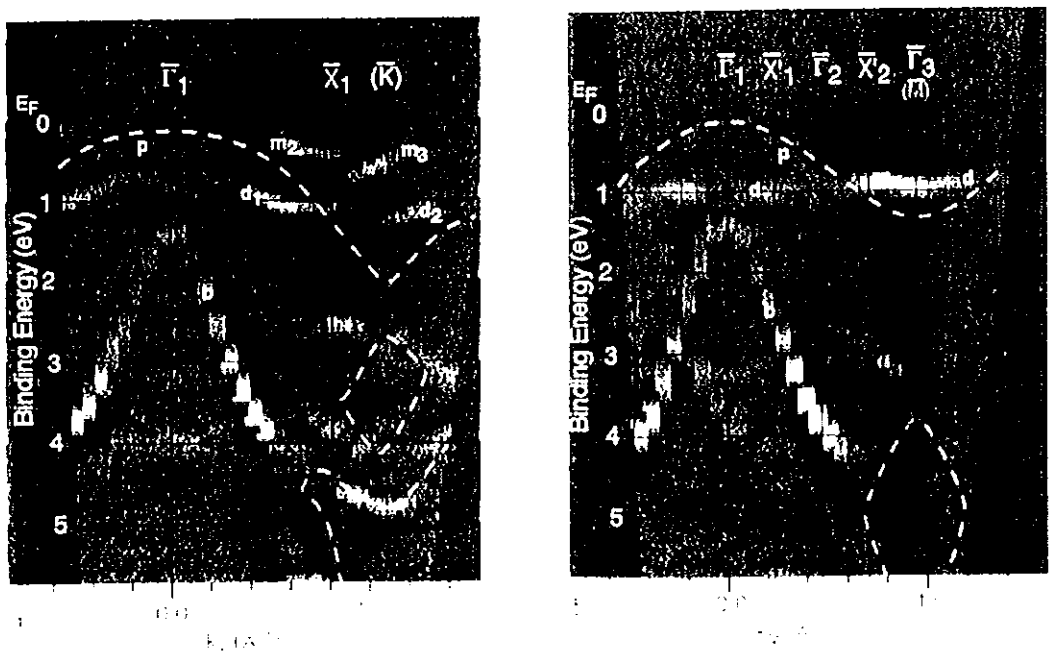

Parallel to chains

Perpendicular to chains

Figure 6.16: Grey scale display of photoemission data collected from the Si(111)4x1-In surface parallel and perpendicular to the chain direction.[22]

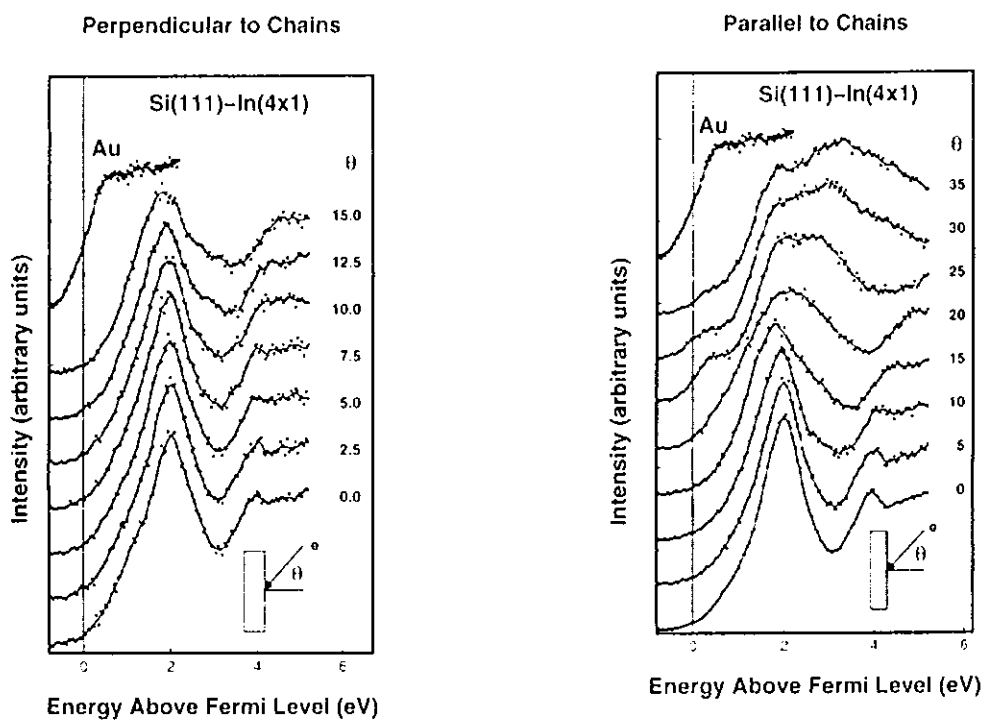

Figure 6.17: IPES spectra of Si(111)4x1-In showing unfilled states parallel and perpendicular to chains.[23]

The STS seemed to show a state at 1eV above the Fermi level, possibly supporting the possibility of the state d being involved, but more work is needed before this can be accepted as definitive. RAS is unable to shed any further light on this issue, and more detailed calculations will probably be required.

With the feature formed after 180 seconds confirmed as due to Si(111)4x1-In, an explanation is now suggested for the behaviour of the fixed wavelength RAS in figure 6.13. At (a) the In is still arranged randomly on the surface, or is forming lower coverage reconstructions that have little or no optical anisotropy. The peak at (b) indicates formation of the 4x1 structure. The initial reduction in intensity(c) after (b), despite the continuing indium flux, was due to the formation of $(1x1)R30^0$ In islands over the 4x1 superstructure, which reduce the RAS signal. As the sticking coefficient for In-In is much less than In-Si,[14] once the flux is removed (d) and the sample is still at 400^0C the In islands desorb, exposing the 4x1 structure again, with a corresponding increase in the RAS signal. The initial slight increase in RAS was found from LEED patterns to be due to the formation of a $(\sqrt{31}x\sqrt{31})$ structure, which forms at lower coverages (Figure 6.5).

6.3 Indium on Silicon(001)

6.3.1 The Bare Si(001) Surface

The currently accepted model of the singular Si(001) surface used in subsequent experiments is shown in figure 6.18.[24] It consists of parallel rows of Si dimers, where the dimer orientation is orthogonal to the apparent row direction. The dimers may be buckled.[25] This is referred to as the Si(001)-2x1 reconstruction. This model is assumed in all subsequent descriptions of the indium reconstructions and is formed after the surface is heated to remove oxide, hydride and any other unwanted adsorbed atoms.

For most of the experiments that will be discussed here, vicinal samples were used, which are polished a few degrees off [001] towards a particular surface direction to preferentially produce steps of a single orientation. The magnitude of this angle will be mentioned when the relevant experimental details are discussed.

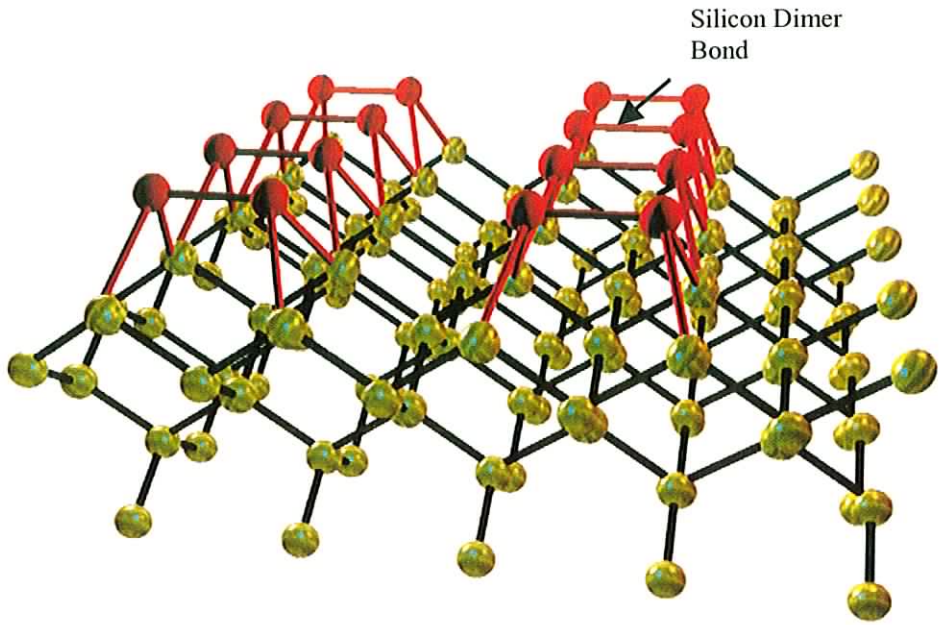

Figure 6.18: Currently accepted Si(100) surface model. The Si dimers are shown unbuckled.

6.3.2 The Si(001)-4x3-In Surface

The 4x3 reconstruction is formed above 150^0C at all but very low coverages (where a partial 4x3 may form). The reconstruction has been extensively studied but its structure has still not been conclusively determined. Previously, non-atomic resolution STM,[26] ICISS,[27] CLPS[28] and PAC[29] were used to determine certain characteristics about the system which allowed the suggestion of plausible models. Further investigation with high resolution STM allowed Zotov, et. al., to suggest a model.[30] This, however, seemed to be incompatible with surface XRD measurements of Bunk, et. al.,[31] which led them to suggest an alternative. As with the 4x1, debate continued about the Zotov and Bunk structures. This appears to have been resolved with the findings that first principles energy calculations[32] once again favour the model of Bunk, et. al. This is shown in figure 6.20.

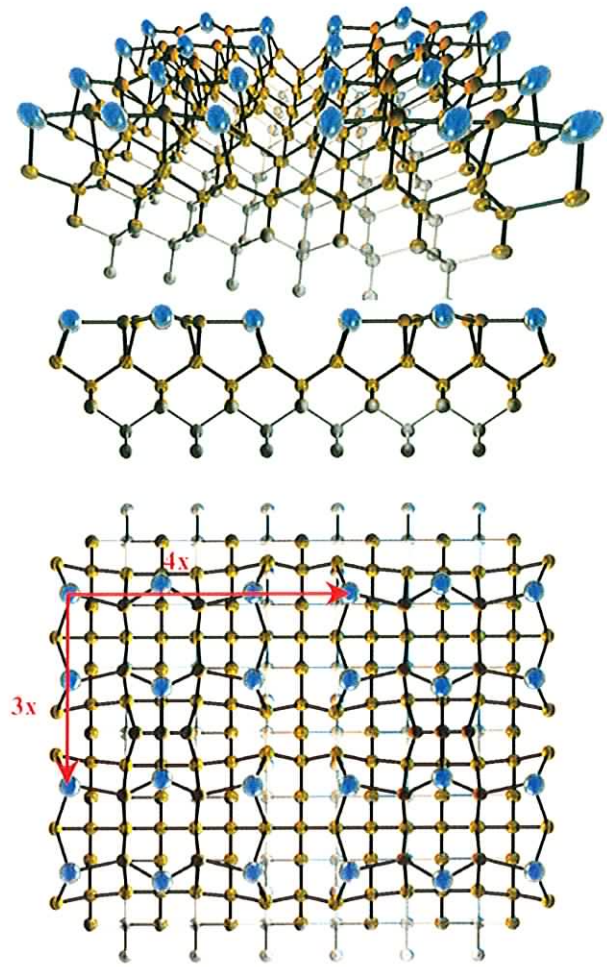

Figure 6.20: The Si(001)4x3-In reconstruction proposed by Bunk, et al.

In this case the surface formation energy of the Bunk, et. al. model is 3.8eV/[4x3]unit cell lower than the Saranin/Zotov model and 2.9eV/cell lower than their amended model. Calculated LDOS for the Bunk model also more closely resembles the STM data of Zotov, et. al.

6.3.3 STM of Si(001)-4x3-In

The experiments were performed in UHV conditions on Si(001) samples offcut by 4^0 towards [110] and mounted in the preparation chamber for direct current heating. All samples were degassed at approximately 600^0C (1.2A current) overnight with system pressure at 3.5 x 10^{-10} mbar. The surface was cleaned by flashing to 600^0C followed by cooling to below 150^0C. In was deposited from a Knudsen cell

evaporator at 900^0C, which was monitored using an flux meter. During In deposition, the K-cell was at 900^0C and chamber pressure was 7.8×10^{-10} mbar. The sample was held at 150^0C. After cooling, the samples were transferred into the STM chamber. STM experiments were then performed on this surface. Figure 6.21 shows two 20nm x 20nm dual scan images of the same region at biases +1.0V and –1.0V, with closer range images in figure 6.22. Excessive indium was deposited in these experiments, resulting in the orthogonal multilayer growth, as opposed to the islanding observed with Si(111)-4x1-In.

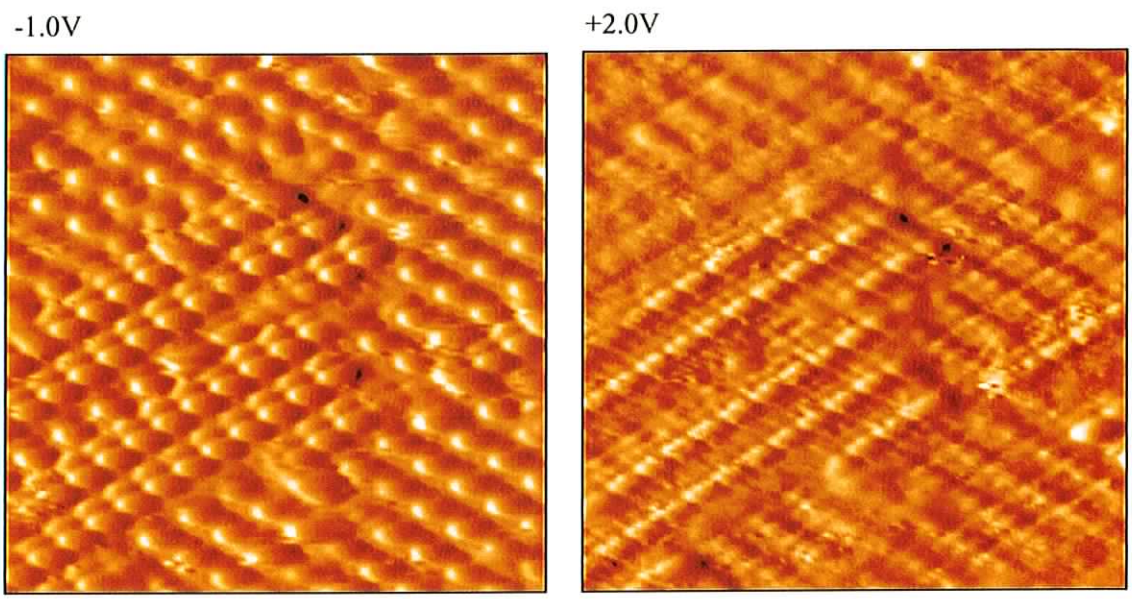

Figure 6.21: Dual scan, 20nm x 20nm, of the Si(001)-4x3-In surface at sample-tip biases of –1.0 and +2.0V respectively.

Some internal structure on the +2.0V image in figure 6.22 is apparent, which compares reasonably with the expected In atom positions from Bunks model, figure 6.20. The exact registry of the In atoms is difficult to judge, as there are no portions of the bare Si(001) surface visible in these images.

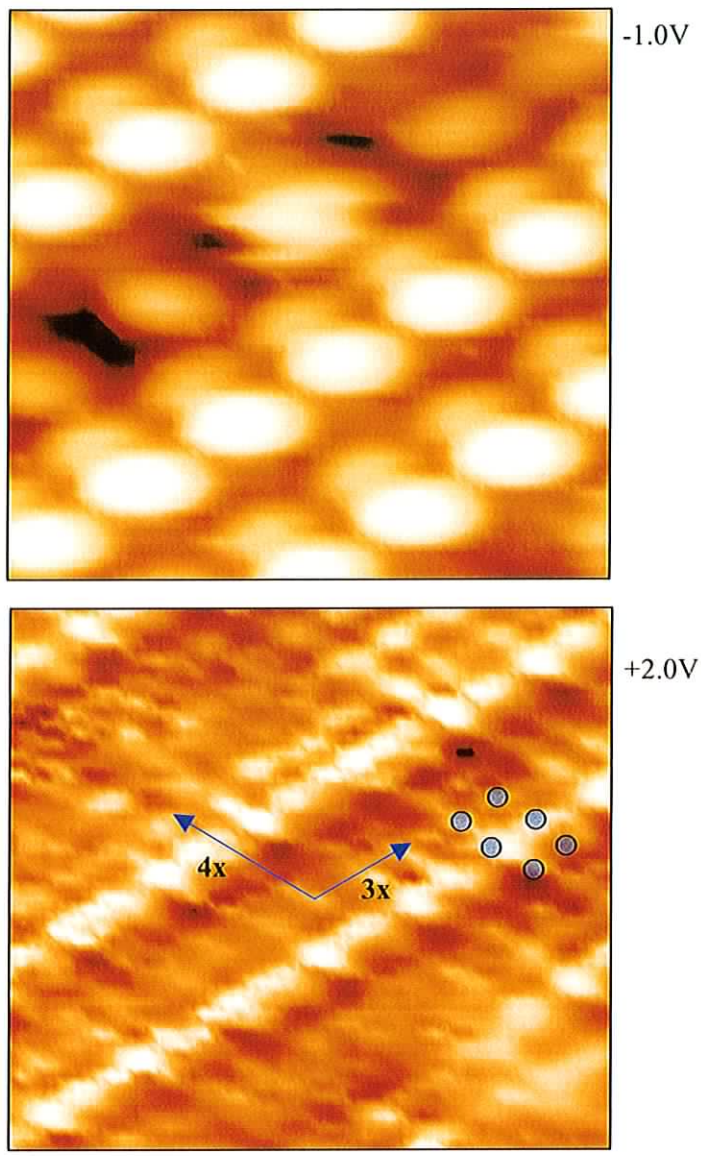

Figure 6.22: Dual scan 5.5nm x 5.5nm STM images, also at –1.0V and +2.0V showing the repeating unit of the 4x3 structure. Some structure is apparent on the +2.0V image, which corresponds reasonably to the expected structure from Bunks model. Expected In atom positions are also indicated.

6.3.4 RAS of Si(001)-4x3-In

Surface treatment and deposition conditions were the same as the STM experiments. The surface was examined using RAS to verify that it was clean whenever this was appropriate. A clean surface RA spectrum is shown in figure 6.23.

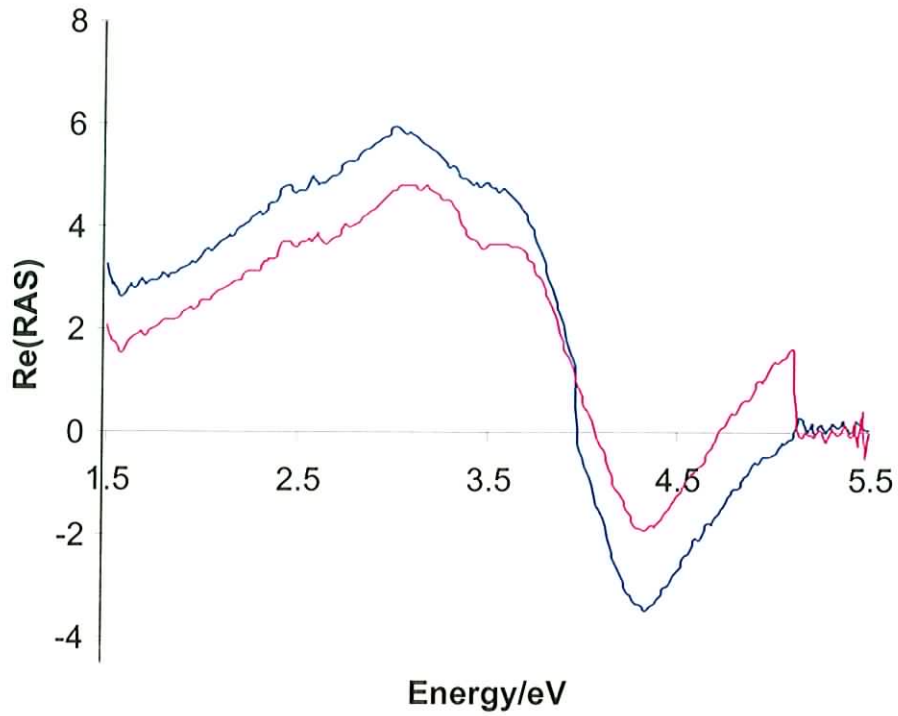

Figure 6.23: Two RAS of clean Si(001) 2x1 surface, which were taken consecutively with about 20 seconds between scans. The offset between spectra may be due to sample cooling. The blue curve was obtained first.

During the initial run, the deposition of In was followed using fixed wavelength RAS at 2.0eV, which as before is an energy associated with In-Si bonds.

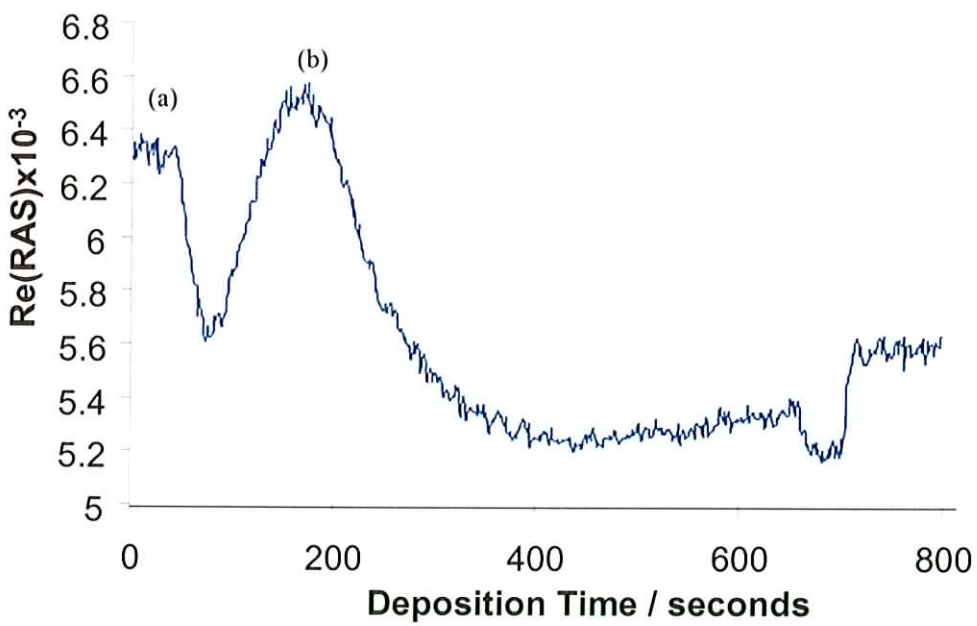

Figure 6.24: A fixed energy scan of In deposition. The sample was maintained at 150^{0}C during deposition. Deposition began at (a), and the RAS signal maximised at (b).

It was impossible to follow the surface changes using LEED during this stage of the experiment due to the chamber's geometry. After 720 seconds the deposition was discontinued and the sample cleaned. The spectrum was used to identify what deposition time was required for transient features to appear, and is shown in figure 6.24. In deposition began at 80 seconds (a). One such feature was observed after 100 seconds of deposition (b), and therefore after the sample was cleaned 100 seconds of In was deposited and the surface examined with variable energy RAS. This was repeated several times to verify its reproducibility and to allow LEED examination. A representative RA spectrum is shown in figure 6.25.

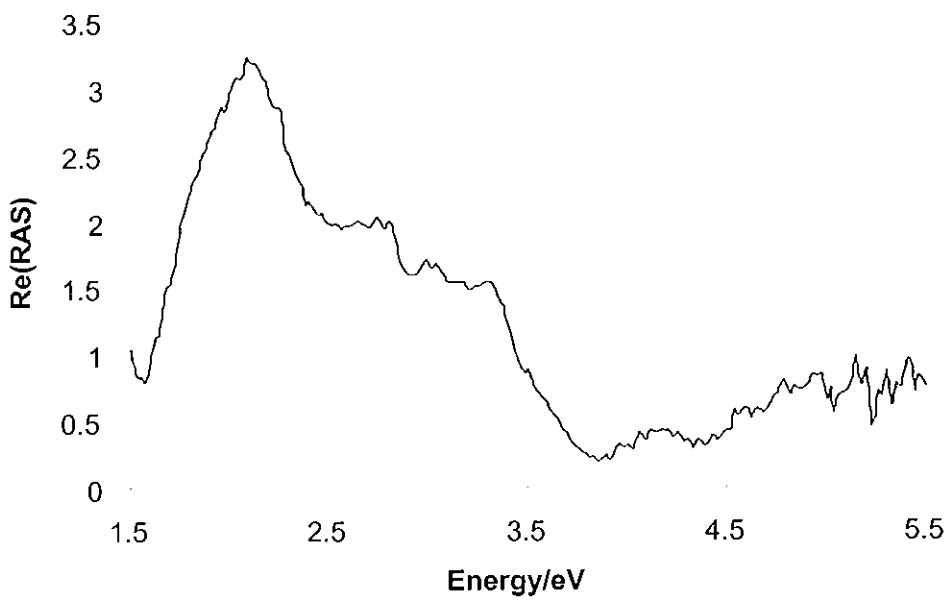

Figure 6.25: RAS of Si(001)4x3-In reconstruction.

This reveals a feature at 2.1eV with a magnitude of ~3 x 10^{-3}. This may be due to In-Si bonding, for reasons mentioned earlier. The reconstruction was later verified as 4x3 using LEED. Unfortunately, to date there is no photoemission data of any kind for this surface, so its electronic structure is unknown and it is difficult to draw conclusions about the features origin. Most work on the system has been structural. This highlights the need for photoemission and inverse photoemission data on this system.

6.4 Summary

The quantum wire candidate structures Si(111)-4x1-In and Si(001)-4x3-In have been investigated using STM, STS and RAS to examine the atomic structure of the systems and to determine how much electron confinement, if any, is present.

Extensive structural studies had been undertaken previously on both systems, but opinion was divided about the outcome, with two competing structures for each system. STM studies were performed to help to resolve this issue. STM of Si(111)-4x1-In demonstrated atomic resolution and a structure that strongly resembles the model proposed by Bunk, et al. STM of Si(001)-4x3-In was not as clear, but a structure that also resembles Bunk's model is apparent. This is strong experimental evidence for the validity of these models. STS of Si(111)-4x1-In showed energy levels that seem to correspond with Nakamura's calculations.

The systems were also investigated with RAS. The Si(001)-4x3-In system has a reasonable RAS response. Without photoemission or calculations, however, it is difficult to say any more, highlighting the need for further work on this reconstruction.

The RAS of Si(111)-4x1-In reconstruction however, is surprisingly large for a semiconductor–metal system. This is strong evidence that there is quantum confinement perpendicular to the chains, although it wasn't possible to determine the precise origin of the RAS feature with certainty. Abukawa's photoemission[22] and Hill's IPES[23] also demonstrates one-dimensional metallicity, which makes the 4x1 a very interesting system, because quasi-one-dimensionality and metallicity are not often found together. The Si(111)5x2-Au system, for example, is metallic but not one dimensional, and Si(111)-M(3x1), M=Li, Na, K, Ag, are one dimensional but insulating. This system may be the smallest metallic wire system in existence, and would appear to be a good test system for quantum wire investigations, and the recent electronic structure calculations are a strong aid in understanding the results of whatever subsequent experiments may be performed. Although the integration of these structures into real devices would be very difficult, similarly sized structures may ultimately be used as atomic scale interconnects in molecular electronic devices, particularly with recent and impending lithography advances.

6.5 References

[1] J. Voit, Rep Prog Phys, 57 977 (1994)

[2] S. Das Sarma, D.W. Wang, Phys. Rev. Lett, 84, 2010, (2000)

[3] F. D. M. Haldane, J. Phys. C: Solid State Phys., 14, 2585, 1981

[4] L K Dash, A J Fisher, J. Phys.: Condens. Matter **13** 5035 (2001)

[5] e.g. J. L. Stevens, M.S. Worthington, I, S. T. Tsong, Phys. Rev. B, 47, 1453, (1993)

[6] J.R. Power, P. Weightman, J.D. O'Mahony, Phys. Rev. B 56 3587 (1997)

[7] K. Takayanagi, Y. Tanishiro, M. Takahashi, S. Takahashi, J. Vac. Sci. Tech. A 3 1502 (1985)

[8] J. Kraft, M.G. Ramsey, F.P. Netzer, Phys. Rev. B. 55, 5384, (1997)

[9] A. A. Saranin, E. A. Khramtsova, K. V. Ignatovich, V. G. Lifshits, T. Numata, O. Kubo, M. Katayama, I. Katayama, K. Oura, Phys. Rev. B, 55, 5353, (1997)

[10] H. Öffner, S. L. Surnev, Y. Shapira, F. P. Netzer, Surf. Sci, 307-309, 315, (1994)

[11] O. Bunk, G. Falkenberg, J. H. Zeysing, L. Lottermoser, R. L. Johnson, M. Nielsen, F. Berg-Rassmussen, J. Baker, R. Feidenhans'l, Phys. Rev. B, 59, 12228, 1999

[12] A. A. Saranin, A. V. Zotov, V. G. Lifshits, J. T. Ryu, O. Kubo, H. Tani, T. Harada, M. Katayama, K. Oura, Phys. Rev. B., 60, 14372, (1999)

[13] K Sakamoto, H. Ashima, H.W. Yeom, W. Uchida, Phys. Rev. B.,**62**, 9923, (2000)

[14] A.A. Saranin, A.V. Zotov, K.V. Ignatovich, V.G. Lifshits, T. Numata, O. Kubo, H. Tani, M. Katayama , K. Oura, Phys. Rev B. 56, 1017, (1997)

[15] K. Pandey, Phys. Rev. Lett. 47, 1913, (1981)

[16] S. Erwin, Phys. Rev. Lett 75, 1973 (1995)

[17] H. W. Yeom, S. Takeda, E. Rotenberg, I. Matsuda, K. Horikoshi, J. Schaefer, C. M. Lee, S. D. Kevan, T. Ohta, T. Nagao, S. Hasegawa, Phys. Rev. Lett, 82, 4898, (1999)

[18] C. Kumph, O. Bunk, J. H. Zeysing, Y. Su, M. Neilsen, R. L. Johnson, R. Feidehans'l, K. Beechgaard, Phys. Rev. Lett, 85, 4917, (2000)

[19] J. Nakamura, S. Watanabe, M. Aono, Phys. Rev. B, 63, 193307, (2001)

[20] J.D. O'Manony, Semicond. Sci. Tech. 8, 495 (1993)

[21] *personal communication, J. R. Power*

[22] T. Abukawa, M. Sasaki, F. Hisamatsu, T. Goto, T. Kinoshita, A. Kakizaki, S. Kono, Surf. Sci. 325 33 (1995)

[23] I.G. Hill, A. B. McLean, Phys. Rev. B. 56, 15725, (1997)

[24] Y.S. Shu, W.S. Yong, F. Jona, P.M. Marcus, The Structure of Surfaces, New York: Springer 1985

[25] B.W. Holland, C.B. Duke, A. Paton, Surf. Sci., 140, L269 (1984)

[26] A. A. Baski, J. Nogami, C. F. Quate, Phys. Rev. B., 43, 9316, (1991)

[27] B. Steele, D. M. Cornelison, L. Li, I. S. T. Tsong, Nuc. Inst. Meth. Phys Res. B, 85, 414, (1994)

[28] H. W. Yeom, T. Abukawa, Y. Takakuwa, Y. Mori, T, Shimatani, A. Kakizaki, S. Kono, Phys. Rev. B., 54, 4456, 1996

[29] G. Krausch, R. Fink, K. Jacobs, B. Luckscheiter, J. Lohmüller, B. U. Runge, U. Wöhrmann, G. Schatz, Surf. Sci., 285, 81, (1993)

[30] A.V. Zotov, A.A. Saranin, V.G. Lifshits, J.T. Ryu, O. Kubo, H. Tani, M. Katayama, K. Oura, Phys. Rev. B 57 12492 (1998)

[31] O. Bunk, G. Falkenberg, L. Seehofer, J. H. Zeysing, R. L. Johnson, M. Neilsen, R. Feidenhans'l, E. Landemark, App. Surf. Sci, 123/124, 104, (1998)

[32] N. Takeuchi, Phys. Rev. B, 63, 245325, (2001)

Chapter 7

Magnetic Behaviour of Metallic Nanoparticles

Following the work on one-dimensional structures, zero dimensional quantum dot type structures were investigated. They should also display unusual behaviour due to quantum confinement. Specifically, Iron and Cobalt metallic nanoparticles were examined for novel magnetic properties. Particles of varying size and size distributions were used, and both static and dynamic magnetic properties were examined.

7.1 Magnetism

Magnetism has long been understood as having its origins in a material's electrons through a combination of spin and angular momentum.[1] Bulk materials can be broadly categorised into three types: Paramagnetic, where the individual moments can align with an applied magnetic field but in the absence of the field there is no preferential alignment direction; Ferromagnetic, where spins possess parallel alignment and a preferential direction, normally caused by the application of an external field at some point in the sample's history; and Antiferromagnetic, where neighbouring spins tend to oppose each other and are equal in magnitude, resulting in a zero net magnetic moment. Ferrimagnetism, a special case of antiferromagnetism, where the spins are opposed but different in magnitude, results in a non zero total moment.

Concentrating on ferromagnetic materials, under normal circumstances a volume of a magnetic material will consist of many domains, which are regions containing atomic moments of parallel alignment. The different domains will not normally be in alignment with each other, and are dynamic, changing size, shape and alignment to minimise the energy of the system for a given orientation of the total moment. Many of the bulk properties are controlled by this behaviour and the interactions at the boundaries between domains.

Although this behaviour has been well categorised for bulk materials, as the material's size is reduced unusual effects begin to be observed. The number of domains diminishes and the energy required to change the orientation of the moment also reduces. On the nanoscale limit the material or particle may become single domain as it is no longer energetically favourable to form multiple domains.[2] The magnetic moment alignment of the entire material, no longer influenced by the domain walls, will be determined by the material's anisotropy. This has two general origins, spin-orbit coupling, which tends to create easy axes along the crystal axes, and shape effects, which are long range dipole effects which are heavily influenced by the material's shape.[3] In larger volumes the shape anisotropy is negligible, but in smaller structures, especially thin films, the shape anisotropy can become more influential and may even dominate.

These effects combine to create an orientational energy dependency for the magnetic moment, normally resulting in one or more low energy directions for the moment separated by energy barriers. To change the direction of the material's moment, a process known as reversal, the system must be given enough energy to overcome the barrier. This may come from the application of an external field or an elevation in temperature.

The energy barrier between different moment orientations is approximated by the following expression, according to the Dormann-Bessais-Fiorani modification of the Shtrikman-Wohlfarth model:[4]

$$\mathrm{E_b} = E_{b0} + n_1 a_1 M_{nr}^2 V \coth\left(\frac{a_1 M_{nr}^2 V}{kT}\right) - \left(\frac{a_1 M_{nr}^2 V}{kT}\right) \qquad \text{Eq. 7.1}$$

where E_{b0} is the energy barrier in the absence of interactions, n_1 the number of nearest neighbours, M_{nr} is the intrinsic magnetisation and a_1 a constant related to the volume concentration of particles in the sample, and V is the particle volume. This shows that there is a dependency of the material's volume, and therefore reduces as a material becomes smaller. In nanoscale samples, this energy barrier may become so low that thermal energy is sufficient to cause the moment switch between easy alignments. This situation, which occurs in single domain particles where the individual atomic

moments behave collectively as one moment, is known as superparamagnetism, due to its resemblance to atomic paramagnetism.

The Langevin function, coth(x)-(1/x), is very important in describing the behaviour of superparamagnetic nanoscale materials and generally relates the magnitude of the magnetic moment to the system temperature. Due to the small size of these structures, effects previously considered negligible may become very important, such as surface roughness or adsorbed impurities.[5] Especially where particle sizes reduce to a scale of ten nanometres, it becomes increasingly difficult to define a magnetic material in conventional terms, as ferromagnetism, antiferromagnetism, etc., require a certain degree of long range order to become definable. The borderline between an oxide coating and the metallic core of a nanoparticle, for example, is very hard to define or describe. The size of even these very small particles precludes first principles calculations at present so a definitive description still awaits.

7.2 Colloidal Metallic Nanoparticles

Colloidal nanoparticles consist of metal cores (cobalt or iron here) with nanometre scale diameters, which are surrounded by a stabiliser, which may be a polymer or some other organic molecule. They are generally prepared using the inverse micelle technique,[6] which involves adding a surfactant material to the desired solvent. The surfactant will then form spherical regions in the solvent, from which the solvent is excluded, which act as mini chemical reactors. A salt of the required metal is then added with a reducing agent. Metal clusters then form in the 'reactors' until the reaction is inhibited, by removal of heat, addition or removal of reagents, etc. This can result in a large size distribution, which is then filtered to product the required size and distribution. Ordinarily, bare metal particles will form agglomerates to reduce the surface energy of the system. To prevent this, the stabiliser is added, which is normally a molecule containing a functional group with an affinity for the particle material. They also help to minimise oxidation.

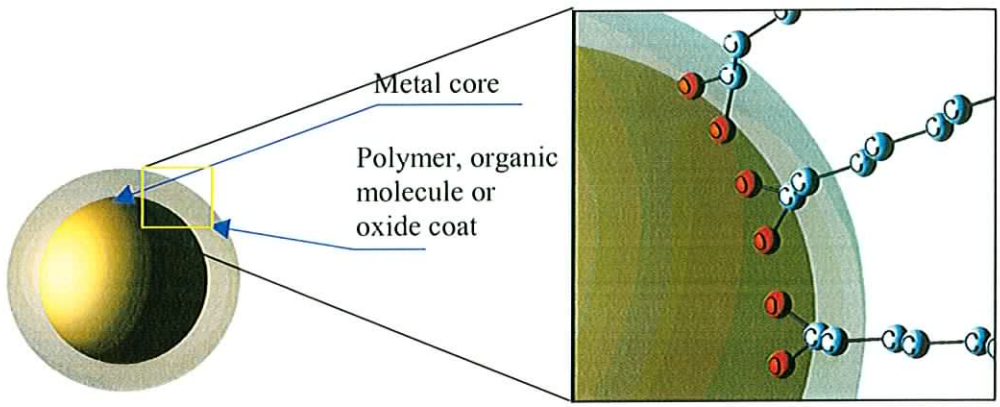

Figure 7.1: Schematic of a metallic nanoparticle. The inset shows the stabilising molecules adhering to the surface of the particle, although exact bonding details, which are uncertain in most cases anyway, are not shown.

Nanoparticles exhibit many interesting electronic, optical and magnetic properties. Due to the small size (cores ≤~11nm) they fit into the category of single domain, superparamagnetic samples outlined previously. It is also found that the magnetic moment of the particles may be enhanced over the bulk due to the larger proportion of atoms at the surface. It has been shown that the presence of a larger surface area results in increased spin and orbital contributions.[7]

The behaviour of these particles can also be modified by external interactions; either deliberately applied external fields or the mutual interactions of an array of particles.[8,9] This interaction can range from purely dipolar at long distances to a combination of dipolar and exchange forces at separations of less than ~1nm. Exchange force interactions between particles are therefore unusual, as the stabilising molecules normally ensure that the cores separation is ~5nm at least.[10]

The internal structure of the particles is also very important and interesting in itself. Despite the presence of the stabiliser and care during particle preparation, some oxidation is inevitable, and while iron and cobalt oxides are antiferromagnetic in bulk form, nanoparticles of these materials display temperature dependent ferromagnetic/superparamagnetic behaviour. This is related to the previously stated requirement to have a certain volume of a material with long range ordering before it can be assigned to a magnetic category. This opens new possibilities for the creation of novel magnetic materials.

Iron and Cobalt particles were examined. The iron particles were obtained in liquid solutions from the University of Utrecht. The cobalt particles were obtained from IBM, pre-deposited onto HOPG substrates.

7.3 Cobalt Particles

The cobalt particles used here were produced by C.B. Murray and S. Sun in IBM's T.J Watson research centre in Yorktown Heights. They are produced by the reduction of $CoCl_2$ in dioctylether in the presence of oleic acid using trialkylphosphine as a reducing agent.[6] Due to the liberation of highly toxic phosphine gas this procedure must be carried out in a double walled preparation chamber.

This procedure results in the formation of particles with diameters between 2-11nm and a size distribution with less than 7% standard deviation. Two types of particles are produced:

1. ε-cobalt The particles are initially produced with an oleic acid stabiliser surrounding the cobalt core, which inhibits oxidation and prevents clumping. These are referred to a ε-cobalt, as the lattice structure is different to the normally occurring cobalt phases, being apparently similar to the β phase of manganese.

2. hcp-cobalt. The ε-cobalt particles can also be annealed to 400^0C in the presence of acetone, which strips the oleic acid, converts the lattice to a hcp structure and oxidises approximately 1nm of the cobalt particle. This strongly inhibits further oxidation of the core.

7.3.1 AFM

As mentioned, the particles used here were obtained already deposited on HOPG surfaces. They were examined using ambient AFM to determine both the fraction of the surface that was covered, how the particles were stacked together and the degree of ordering, as shown for a hcp sample in figure 7.2. The instrument used was a Nanoscope iii from Digital Instruments with ~10nm diameter tips from Olympus. The scans were obtained in tapping mode. As the particle diameters were similar in size to

the tip radius, obtaining clear images was difficult and a lot of parameter variations were required to optimise them.

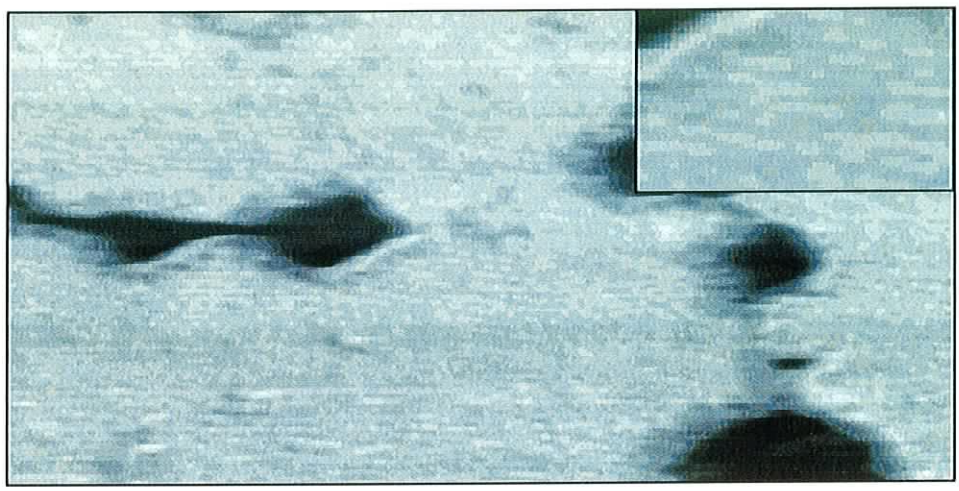

Figure 7.2: AFM image (547nm x 744nm) of hcp-cobalt particles on HOPG substrate, demonstrating surface coverage and hexagonal arrays. Inset shows 70nm x 100nm zoomed image. This may be compared to the TEM in figure 1.6, which is a close range image showing better resolution of the particles.

Although it is difficult to numerically quantify the surface coverage, figure 7.2 is typical for most of the surface. This is important as sufficient surface coverage is a requirement for optical measurements to ensure acceptable signal/noise discrimination. The images also demonstrated excellent hexagonal ordering (inset, figure 7.2). Figure 7.3 shows a image of an ε-Co sample taken on the same instrument, demonstrating similar ordering.

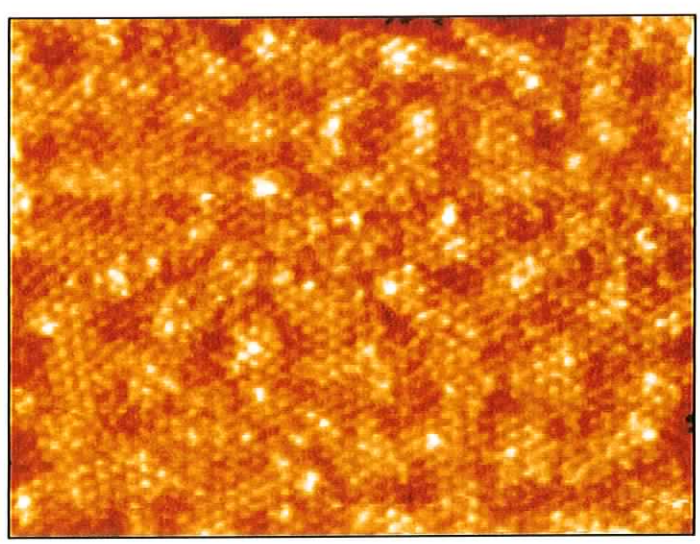

Figure 7.3: AFM image (547nm x 744nm) of ε-cobalt particles on HOPG substrate, showing hexagonal ordering.

7.3.2 XPS

XPS was performed on ε-Co particles in an effort to determine the degree of oxidation of the surface. Although it is not ideal due to poor depth penetration, it was used because Co Mössbauer was not available. Figure 7.4 shows a spectrum obtained from the particles, along with Co and CoO reference peaks. It was not conclusive, showing only that the particle cobalt peaks are offset from the expected positions of both cobalt and cobalt oxide. This may be because of unusual bonding at the surface or interference from the shell.

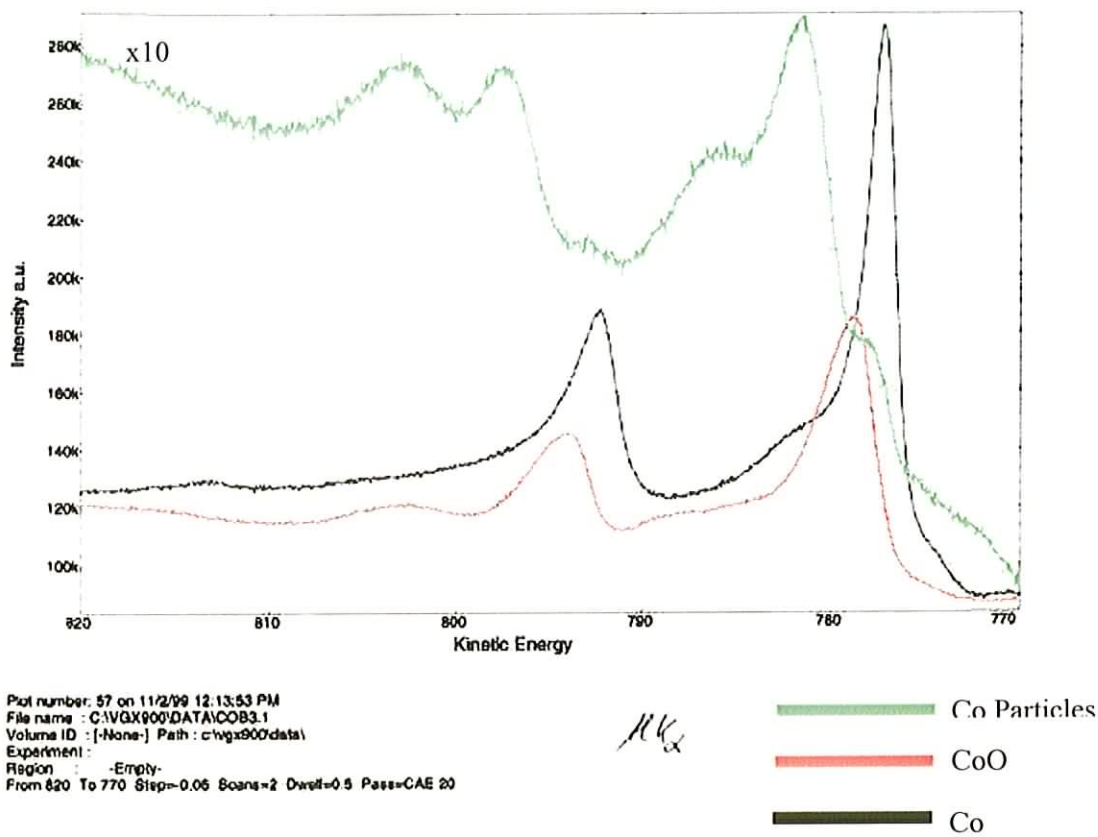

Figure 7.4: XPS spectra showing cobalt particles (green), reference cobalt oxide (red) and elemental cobalt(black) The peaks are shifted by approximately 5eV from the Co peaks and approximately 3eV from the CoO peaks. They are also broadened, suggesting a distribution of environments is present. The cobalt particle spectrum is scaled by a factor of ten, for clarity.

It has been shown that nanoparticles can exhibit shifted photoemission responses due to relaxation of the surface bonds, which can also generate an electrical dipole moment by pushing electron density towards the particle core.[11] Detailed calculations are needed to quantify this shift, however, and that was not possible here.

7.3.3 SQUID

The magnetic properties of the ε-cobalt particles were examined using a commercial SQUID magnetometer at various temperatures from 5K to 300K, shown in figure 7.5, which shows two ranges, from –0.5 to +0.5T and –0.1 to +0.1T.

The squid curves demonstrate a clear transition from ferromagnetic behaviour to a superparamagnetic regime, somewhere between 150 and 200K. This is shown by the loss of hysteresis between those temperatures. Loss of hysteresis is an effect that superparamagnetic particles exhibit.[12]

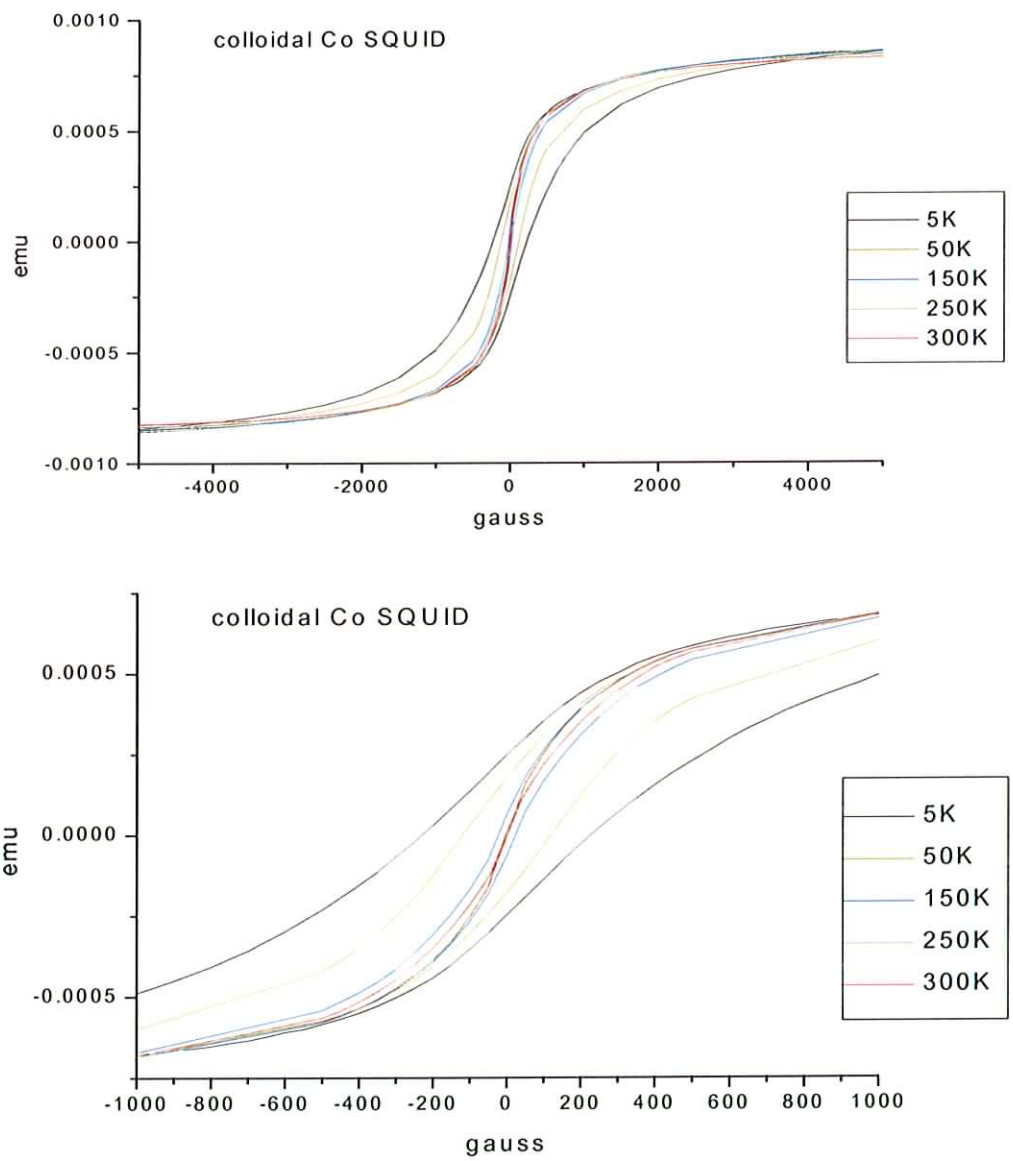

Figure 7.5: Variable temperature SQUID measurements on ε-Co samples, showing the sample magnetisation against applied field, demonstrating a transition from ferromagnetic (from 5K to 150K) to superparamagnetic (above 250K).

7.3.4 MOKE

The magnetic properties of the ε-cobalt particles were also examined optically using MOKE. Using the setup shown in figure 5.4, the sample was mounted in the holder and measurements were taken at several points on the surface by focusing the laser spot on the desired region. Due to the low signal, it was necessary to average over several measurement cycles. Room temperature measurements, figure 7.6, revealed superparamagnetic behaviour, in line with expectations. This is qualitatively similar to the room temperature SQUID measurements from section 7.3.3.

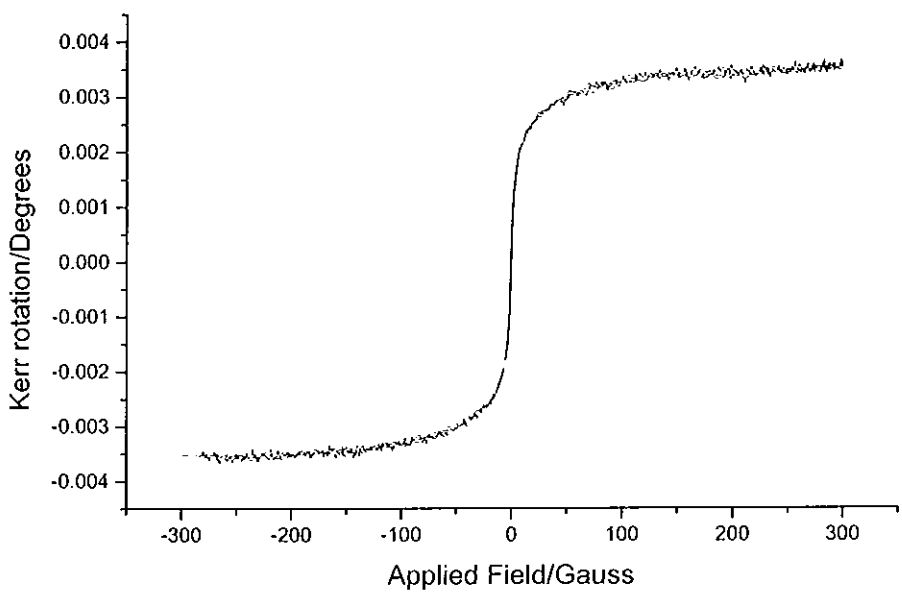

Figure 7.6: Room temperature MOKE of colloidal cobalt particles on HOPG, demonstrating superparamagnetic behaviour (loss of hysteresis).

Low temperature MOKE was performed by placing the samples into a cryostat. A specialised cryostat/electromagnet assembly replaces the sample holder/electromagnet from figure 5.4. In this experiment, magnetisation curves were very difficult to obtain, as there seemed to be a faraday rotation in the cryostat window that was larger that the particle response. This may have been due to insufficient magnetic field strength at the sample position in the cryostat, or an insufficient quantity of particles on the sample. In the time available to perform the experiments, this problem could not be overcome. The experiment did demonstrate one advantage of MOKE over SQUID though, which is its ability to sample different points over a surface. The samples used had partial coverage of the particles, as determined by AFM in section 7.3.1, and the

MOKE signal was observed to disappear over the regions of bare HOPG and reappear over covered regions.

7.3.5 TRMOKE

Time resolved MOKE measurements were also performed, shown in figures 7.7 and 7.8. These show the samples in opposing magnetic fields. There is no discernible difference between the signals, suggesting that the applied magnetic field was too low or that there was insufficient material to obtain a detectable response. The features present are due to the sample's reflectivity changing with temperature.

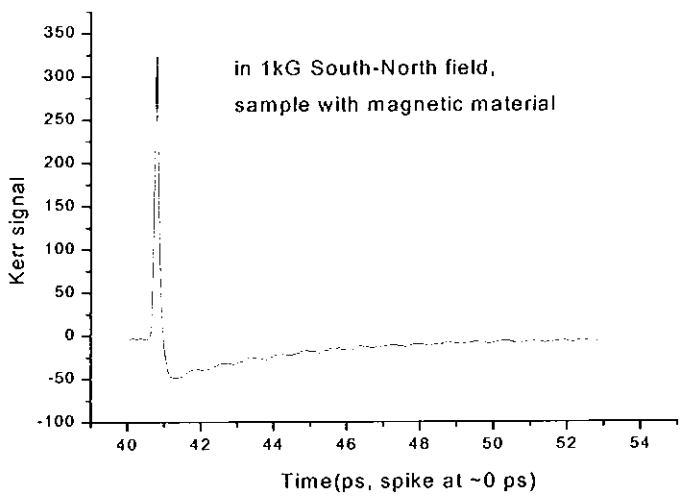

Figure 7.7: Time resolved MOKE measurements of Co particles taken in longitudinal geometry with South-North field. After the initial reflectance spike there is a gradually diminishing oscillation, later attributed to phonons reflecting in the substrate.

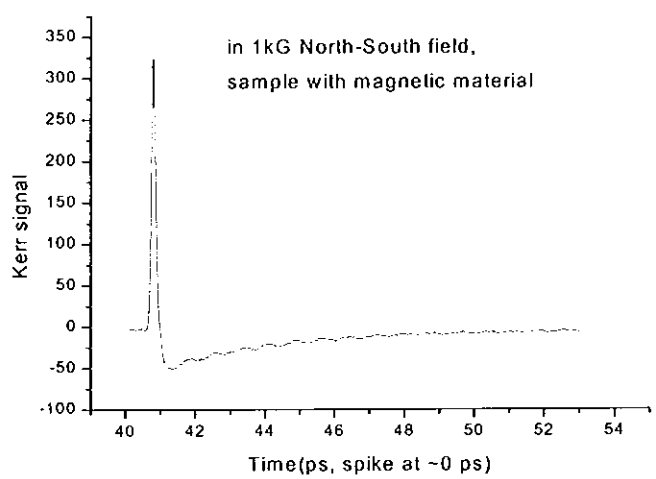

Figure 7.8: Time resolved MOKE measurements of Co particles taken in longitudinal geometry in North-South field. This is identical to figure 7.7, indicating that the features are due to non-magnetic effects.

An oscillation was present in the measurements taken on the samples, which had an unclear origin. It was found, however, that this was also present in the bare HOPG measurements with similar amplitude and frequency, suggesting that it is non-magnetic and probably caused by phonons moving from the top to the bottom of the sample and reflecting from different distances. Despite the lack of success of the optical measurements, they are still very promising for studying this type of magnetic behaviour. Improvements in the signal/noise performance of the instruments and the magnetic field strengths that can be generated should improve the chances of success. The use of larger particles, which are closer to the border of ferromagnetic behaviour at room temperature, might also be more successful in the short term, although this defeats the purpose of generalising the technique for the study of all particle sizes.

7.4 Iron Particles

The iron core samples used in this work were produced by Karen Butter, et. al., in the University of Utrecht, also using the inverse micelle technique. Iron pentacarbonyl ($Fe(CO)_5$) is used as the metal source, in a solution of decaline. Decomposition of the $Fe(CO)_5$ is controlled by temperature rather than a reducing agent in this case. Temperature is applied until the clusters reach a desired size, after which the solution is allowed to cool. After separation, many samples of varying sizes and distribution are produced. In this work, particles with a 10.5nm diameter core, and a standard deviation size distribution of approximately 15%, determined from TEM measurements, were used. The stabilising molecule in the case is a form of polyisobutene, code number SAP 285 from Shell Chemicals. This is approximately 10nm long, but is somewhat flexible. The resulting particles are therefore 30nm in diameter with 10.5nm cores. Due to the polymer coat which enforces a ~20nm separation between metal cores, any interactions are again going to be dipolar.

7.4.1 Mössbauer Spectroscopy

In order to determine the particle core composition, the particles were studied using Fe^{57} Mössbauer spectroscopy, in experiments performed on our behalf by the Interfaculty Reactor Institute at TU Delft. These spectra are shown in figure 7.9. Particles of different size were analysed for comparison.

TEM work carried out in prior to this work in Utrecht indicated that there were two distinct regions in the metal cores. These were believed to be a elemental iron core surrounded by an iron oxide coat. Through the use of curve fitting, however, it was determined that two forms of iron oxide were present, and that there was no elemental iron, despite the preparation of the particles under nitrogen and the protection of the polymer shell. That the particles are still magnetic is very interesting, as bulk iron oxide is antiferromagnetic due to superexchange.[13] This is an example of the unexpected effects that can arise in quantum scale structures.

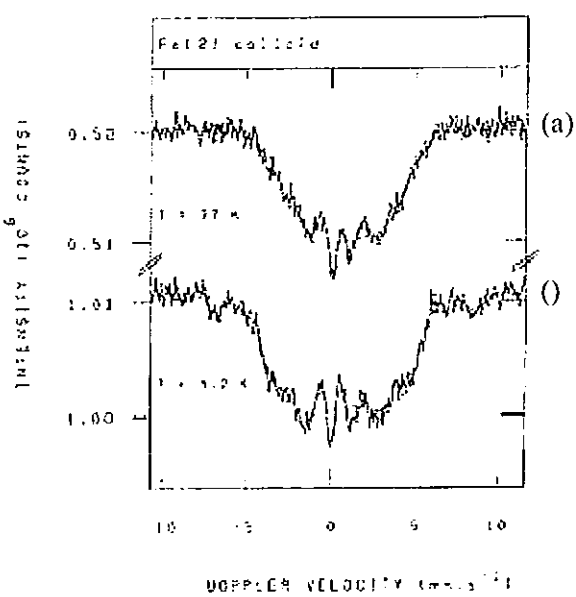

Figure 7.9: Mössbauer spectroscopy of 30nm particles at (a)77K and (b)4.2K. The use of curve fitting determined that two iron oxides were present.

7.4.2 AFM and MFM of Iron Particles.

The iron particles were imaged using a Digital Instruments Nanoscope iii AFM/MFM under similar conditions to the Co particle experiments, again to determine coverage and ordering. In order to do this they had to be deposited onto a

substrate. Thermally oxidised Si(111) was used due to its availability. It was spin coated with the polymer Formvar, to modify the particle-surface adhesion properties. By adjusting the rotational speed a smooth, even coverage of Formvar could be obtained. The particles were then deposited using Michelotto's method,[14] which involves the slow evaporation of a solution of particles onto an inclined substrate. The evaporation is controlled by the quantity of solvent vapour in the local atmosphere, and the particle density on the substrate is controlled by the solution concentration. The setup is shown diagrammatically in figure 7.10. The optimum angle was found to be ~10^0. This should lead to an even, well dispersed particle distribution.

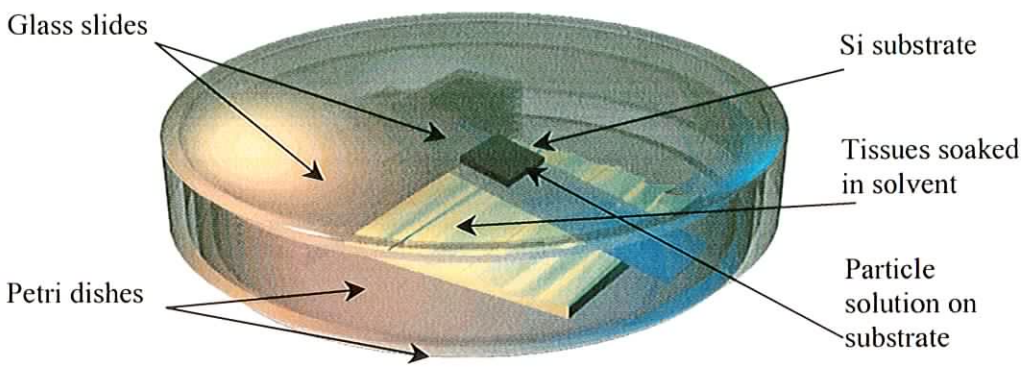

Figure 7.10: Method of deposition of iron particles onto a substrate.

These films were also found to be very stable. The AFM images in figure 7.11(a) was taken after the films were prepared, 7.11(b) and (c) were taken one year after the films were originally prepared, using an Omicron UHV AFM. Aside from some aggregation the films are essentially the same as after initial deposition.

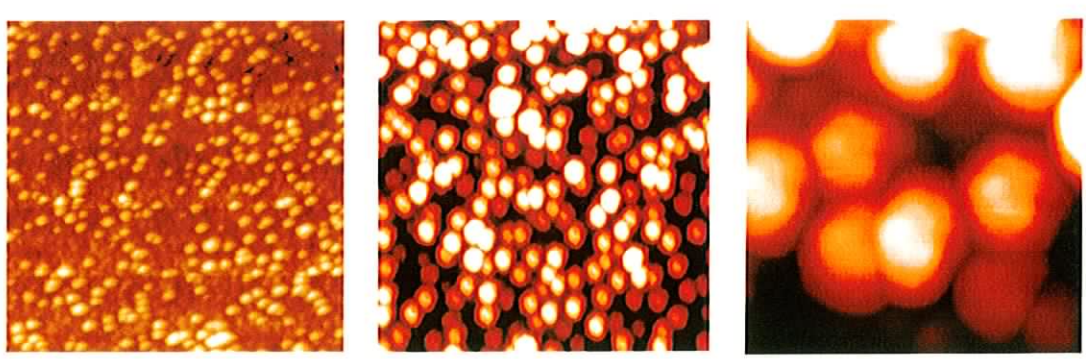

Figure 7.11: AFM images of iron nanoparticles.(a)700 x 700nm (b) 500x500nm after 1 year, in UHV (c) 100x100nm after 1 year, in UHV.

This image shows that the particles are forming disordered arrays. This disorder is probably due to the relatively large size distribution. This sample was also examined using MFM, which takes topographic and magnetic images.[15] Both images were taken in tapping mode.

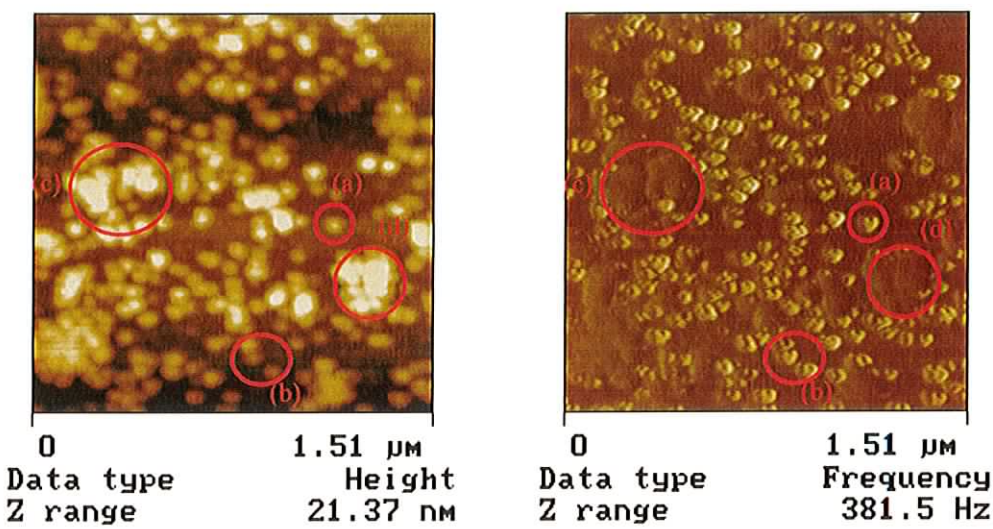

Figure 7.12: Topographic and magnetic force gradient image of iron particles on Formvar coated SiO_2. The marked regions are discussed in the text.

Figure 7.12 shows topographic and magnetic force gradient images taken over the same region of the sample. This demonstrates an unusual effect. If the images are compared, it can be seen that individual particles are visible on both scans, as can be seen in regions (a) and (b). However, the particles that are gathered in clusters are strongly visible on the topographic image only, with only a slight cloudiness and edge enhancement visible on the magnetic force gradient image, regions (c) and (d). This image was collected at a liftheight of 5nm. Below this height, the van der Waals and capillary forces that comprise a topographic image were apparent in the magnetic images, and both were very similar. Above 5nm, the cluster effect was still observable but lateral resolution diminished.

This is interesting as it seems to suggest that the mutual interaction of the particles can generate a sufficient anisotropy barrier to overcome these particles superparamagnetic behaviour at room temperature. Due to the spacing between the cores being a minimum of ~20nm, the interaction must be dipolar. The strongest

interaction between the tip and the sample occur when the magnetic moments of both are aligned. In this case, the tip moment was aligned vertically downward. A vertically magnetised particle would therefore produce the strongest response, and an in-plane magnetisation the weakest. A group of interacting clusters is more likely to produce an in-plane magnetisation which would account for this, and this would make it more difficult for the field of the tip to align the moments. An isolated particle would be more easily aligned by the tip and should therefore show up as a stronger interaction. This assumes that the local field is sufficient to overcome the anisotropy barrier in the particles, and that the tip field strength is sufficient to align the particles, even an isolated particle. Computer modelling was performed to analyse the validity of these statements and the model.

7.5 The Dipolar Model

The particles are nominally 10nm iron cores, therefore they should be single domain, as the minimum domain size is typically of the order of 50nm. They are also superparamagnetic at room temperature as the anisotropy energy for such a particle will be lower than for a larger multi-domain sample. Because of this, they were treated as simple dipoles and the particle's anisotropy energy was neglected. The surrounding polymer shell is at least 10nm thick, so the interaction should be dipolar only.

The initial supposition was that the dipole interaction of the particles when they are arranged in clusters was strong enough to prevent the particles from aligning with the tip as it passed over, as long as the tip was above a certain height. Particles with appreciable nearest neighbour spacing will experience a weaker dipole interaction and will be more easily aligned by the tip, which should therefore feel a greater force gradient. The edge effect was probably caused by the in-plane alignment of the moments in the clusters, which would produce a different interaction with the tip depending on the how the tip's magnetisation related to the different magnetisation at each cluster edge, figure 7.13. The model ignores the effect of van der Waals forces, which are responsible for topographic AFM interactions, and capillary forces, which occur due to a layer of adsorbed moisture that can bridge the tip and sample in

ambient AFM. Both forces only come into effect at tip sample separations of a few nanometers, although this may vary slightly for different samples, so if the separation is kept over a few nanometres the assumption is valid.[16]

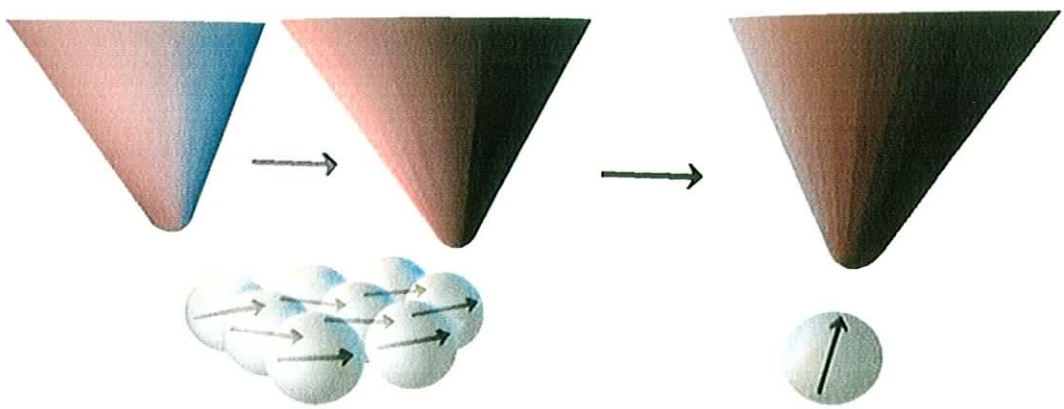

Figure 7.13: Tip motion over sample, demonstrating a potential origin of the edge effect seen in the MFM image in figure 7.9.On one side of the cluster the tip interacts with a dipole 'tail', and on the other side with a dipole 'head', producing a different response on the two sides.

7.5.1 Finite Element Analysis: Two-Dimensional Calculations

The model was first tested using Quickfield 4.0 from Tera Analysis, a fast 2D finite element analysis package. The model was constructed using the built-in model editor which allowed the system to be constructed on the correct length scale. An example of this is shown in figure 7.14. The particles were modelled as an iron core, as iron oxide particle data was not available, and the polymer shell was treated as a non-magnetic layer with permeability equal to that of vacuum. A non-magnetic substrate with permeability between that of iron and vacuum was used to simulate the Formvar coated silicon substrate. The tip was treated as magnetised iron. It was determined experimentally by magnetometry[17] that the tip's magnetisation was 400,000 A/m and the coercivity was 37,500 A/m and these values were used in the simulation.

Cluster sizes of 1 to 5 particles were chosen, as this seemed to typify the range of sizes found in figure 7.12. The choice of tip size was somewhat arbitrary, a balance between having a conveniently solvable system while maintaining accuracy. Different tip sizes were tested. It was found that smaller tips interacted too locally with the

system, but once the tip was above a certain size the response became more long range and showed little variation. A size at the lower limit of this size range was chosen, approximately 200nm by 70nm, figure 7.14.

Although the iron cores of the particles were superparamagnetic at the measurement temperature, Quickfield does not allow a material to be specifically described as superparamagnetic, therefore an approximation of this effect is required. A superparamagnetic material has zero coercivity and a magnetisation that never saturates, as shown in figure 7.15.

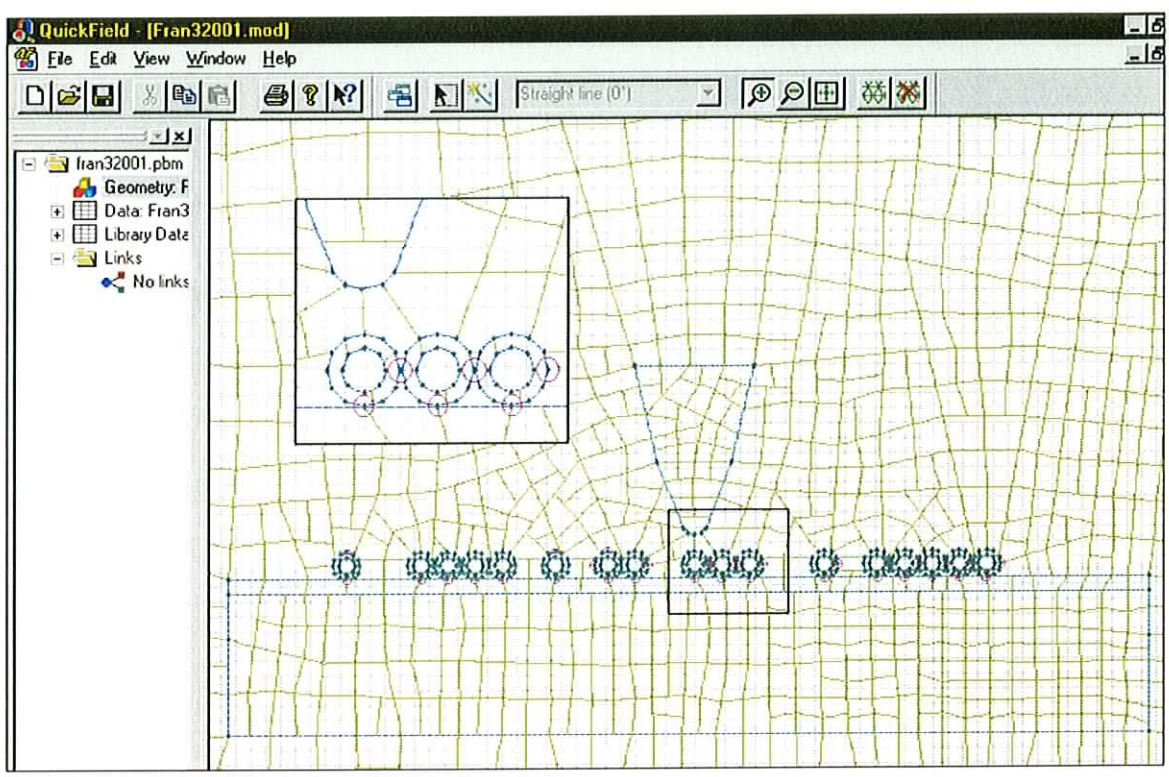

Figure 7.14: The Quickfield model editor. The inset shows the particles and tip in greater detail.

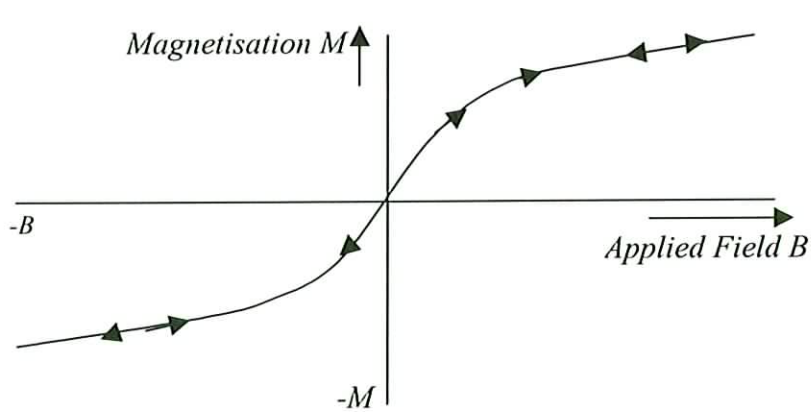

Figure 7.15: Magnetisation curve of a superparamagnetic material.

In Quickfield's solver description, the magnetisation of a material is controlled by its coercivity, and if a material is given zero coercivity it is treated as a non-magnetic metal, therefore in order to simulate superparamagnetism, the particles were given a large coercivity. This at first seems counter intuitive, but it does simulate the non-saturating magnetisation, which is probably the most important aspect of superparamagnetism for this model. Both high and low coercivity systems were simulated to verify this.

The force gradient was calculated at each point by placing the tip at a distance of ±z from the equilibrium position and using the following expression:

$$\frac{\partial F_Z}{\partial Z} = \frac{F_{Z1} - F_{Z2}}{Z_1 - Z_2} \qquad \text{Eq. 7.2}$$

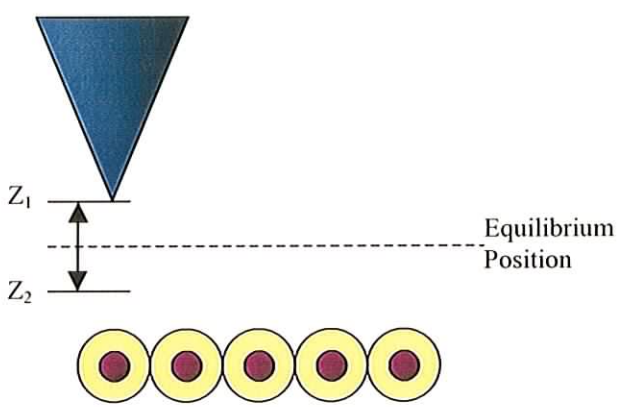

Figure 7.16: Tip positions at which force measurements were made.

where F_Z is the z component of the force felt by the tip and Z is the height above the sample. To perform its calculations, Quickfield calculated the vector magnetic potential, from which B and H can be calculated. The force is then calculated from

$$\vec{F} = \frac{1}{2}\oint\left[\vec{H}\left(\hat{n}\cdot\vec{B}\right) + \vec{B}\left(\hat{n}\cdot\vec{H}\right) - \hat{n}\left(\vec{H}\cdot\vec{B}\right)\right]ds \qquad \text{Eq. 7.3}$$

where $\hat{n}$ is a unit vector normal to the surface of the volume being integrated. The tip was moved in steps across the surface and data collected at each point.

7.5.2 Results

An image of the model used is shown in figure 7.14. It consists of a mixed set of particles, consisting of three single particles and clusters of particles ranging is size from two to five particles. These sit on top of a substrate, which has a thin layer on top to simulate the effect of the polymer. The tip was generated and its magnetisation was set to the measured value. The force at heights ranging from 4 to 11nm was measured as the tip was moved over the particles. This is shown in figures 7.17 and 7.18 for the low and high sample coercivities respectively.

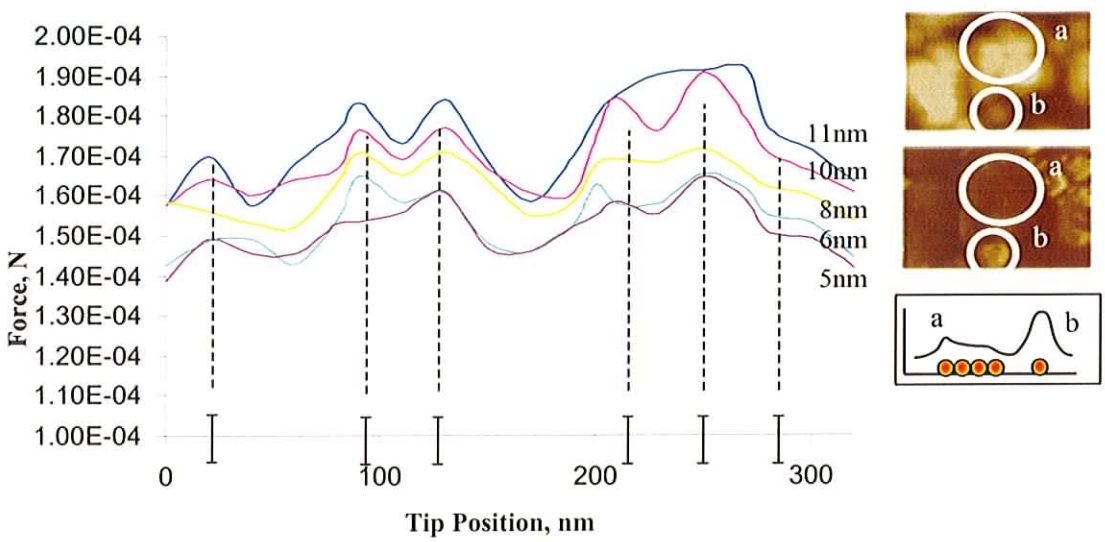

Figure 7.17: Tip sample force curves taken with low sample coercivity (700A/m). The inset shows the expected response from figure 7.12. The bars on the force curve x-axis indicate the particle positions.

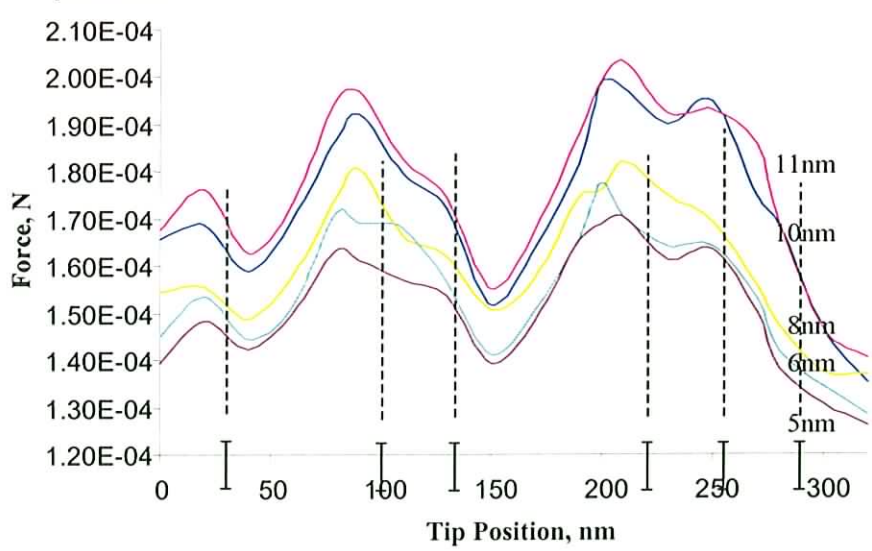

Figure 7.18: Tip sample force curves taken with high sample coercivity (70,000 A/m). The bars on the x-axis indicate the particle positions.

From these plots the force derivative can be estimated, at various equilibrium heights and oscillation amplitudes. Some relevant examples are shown in figures 7.19 and 7.20.

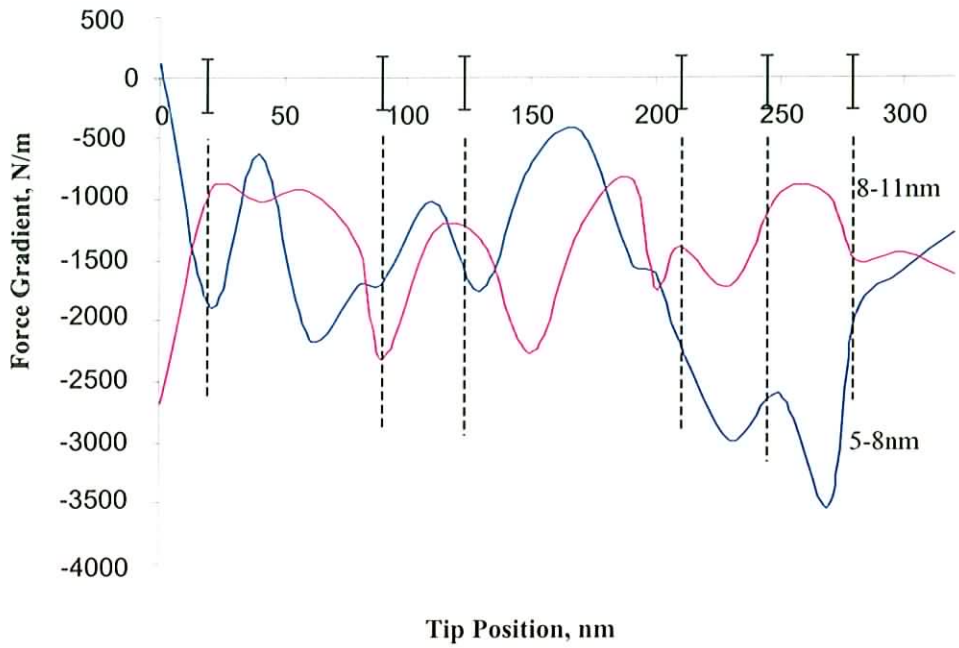

Figure 7.19: Force gradients taken from figure 7.16 (low coercivity). The purple and blue lines represent the gradients between 8 to 11nm and 5 to 8nm respectively. The bars on the x-axis indicate the particle positions.

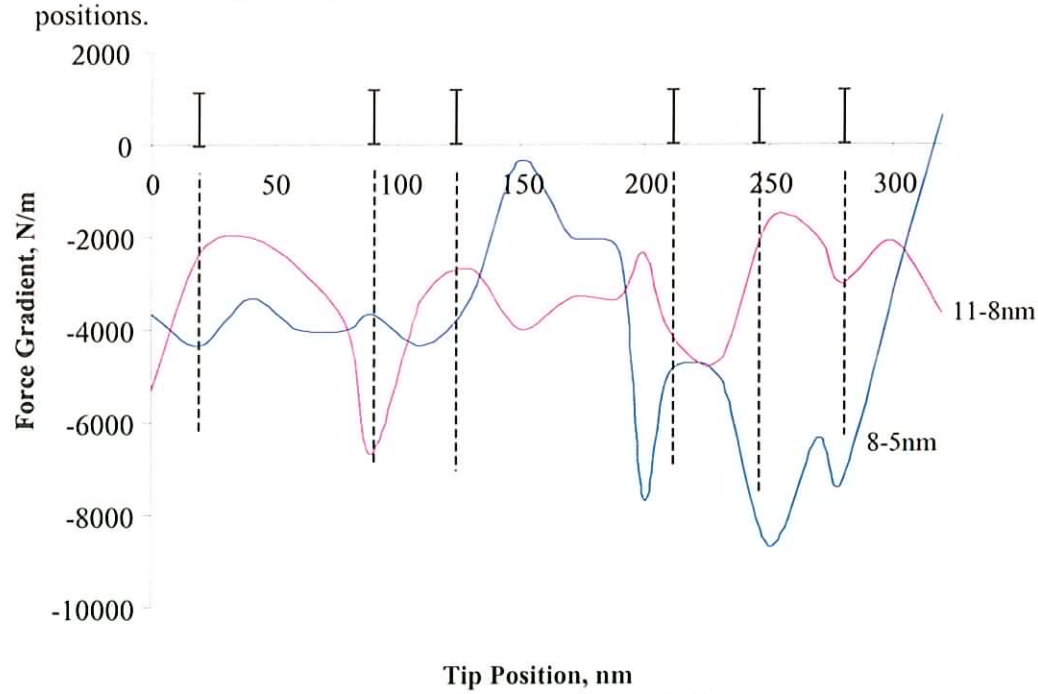

Figure 7.20: Force gradients taken from figure 7.17 (high coercivity). The purple and blue lines represent the gradients between 8 to 11nm and 5 to 8nm respectively. The bars on the x-axis indicate the particle positions.

Figures 7.19 and 7.20 most closely resemble the expected profile between 8 to 5nm, with a loss of resolution between 8 and 11nm. The high sample coercivity data in 7.19 has the closest similarity to the measured data, as do the curves corresponding to closer tip-particle separations. It is possible to make some generalisations based on these plots:

(i) The edge effects seen around the clusters were apparent in this model, and were best observed at closer tip-sample separations.

(ii) The distance dependence effects were noticeable except at close range, where the program was not able to simulate the effects of van der Waals forces and the capillary forces that arise due to moisture bridging the tip-sample gap

(iii) A larger force gradient over the single or isolated particles with respect to that over the clusters of particles, which would be expected from 8.1, was not seen.

(iv) The calculated forces and consequently force gradients are orders of magnitude larger than expected, with typical experimental values in the sub-nano-Newton range.[16]

Many variations on this idea were tried, such as varying material parameters, substrate parameters, tip size, etc. While these had an effect on the magnitude and shape of the curves they were unable to make the interaction greater over a single particle. The closest agreement came at small tip oscillation amplitudes. The principle of this model is therefore probably correct, but some extension to it is needed to give more quantitative agreement. Possible omissions were the inability of Quickfield to accurately simulate a superparamagnetic material or possibly the two dimensional character of the model. In order to investigate this, custom software had to be written, as Quickfield would not allow it.

7.5.3 The Three-Dimensional Model Extension.

In order to investigate the new model and to more accurately represent the system it was necessary to write a simulation from the ground up, and the C++ programming language was chosen, using the Borland C++ Builder IDE. The code is shown in

Appendix 2. Because of its use of Borland's proprietary vcl libraries, which are an abstraction layer to simplify access to the windows API and allow visual development of the user interface, it will not compile with another complier without modification. The model is simpler than the Quickfield version, in that the particles are treated as simple point dipoles, and the tip as an array of dipoles with fixed spacing in the form of a rounded pyramid. The program was created in consultation with Dr Coen Swüste of TU Eindhoven, and performs its calculations in the following way

1 The tip dipoles are initialised to a fixed value m_z and orientated vertically downwards. These values are presumed to be constant during the experiment, and the program does not attempt to alter them.

2 The particles are initialised at x, y and z coordinates to a state of in-plane magnetisation in a certain arbitrary direction, i.e. m_z=0, m_y=0 and m_z=m, where m_i represents the magnetisation in the i direction. The particle may also be initialised into a completely random orientation with x, y and z freedom, but it was determined that this had no effect on the program output and the in-plane configuration was chosen for convenience. It was also observed that the particles obtain an in-plane orientation in the absence of the tip.

3 The H-field that the tip would generate at each of the x, y and z coordinates assigned to the particles is calculated from the following equations:

$$H_x = \frac{3(m_x dx + m_y dy + m_z dz)dx - m_x r^2}{r^5} \qquad \text{Eq. 7.4}$$

$$H_y = \frac{3(m_x dx + m_y dy + m_z dz)dy - m_y r^2}{r^5} \qquad \text{Eq. 7.5}$$

$$H_z = \frac{3(m_x dx + m_y dy + m_z dz)dz - m_z r^2}{r^5} \qquad \text{Eq. 7.6}$$

4 The H field components calculated in step 3 are used to generate the sample magnetisation in accordance with the Langevin function

$$M = M_s\left[\coth\left(\frac{\mu H}{kT}\right) - \left(\frac{kT}{\mu H}\right)\right] \qquad \text{Eq. 7.7}$$

where μ is the particle dipole moment, k is the boltzman constant and T the temperature.

5 The H field that these moments exert on each other is calculated for each particle by summing the individual vector contributions together. This is added to the existing field caused by the tip.

6 The sample magnetisation is recalculated with the new H field values. The magnetic energy of the system is calculated from

$$E = \vec{H} \cdot \vec{M} \qquad \text{Eq. 7.8}$$

7 Steps 5 and 6 are repeated and the energy is compared to that of the previous calculation. These steps are iterated until the energy variation decreases to a predefined limit.

8 The force is then calculated from

$$F = \frac{m_1 m_2}{\mu r^2} \qquad \text{Eq. 7.9}$$

where m_1 and m_2 are dipole moments. This is performed at two heights and the force gradient calculated as previously. The calculation stage then exits.

The output of the calculations is drawn to the screen. A screenshot is shown in figure 7.21. An explanation of the geometry is given in Appendix B. On the vertical image the start and finish positions of rectangular scan may be defined using mouse clicks. The program begins at the initial point, and calculates the force gradient by calculating the force at two heights, determined by the user, and using equation 7.1. This step is repeated at intervals across the rectangle and the output is directed to a text file which may be plotted using, for example, Matlab.

The simulation allows the user to vary the following parameters:

(i) The number of particles in the cluster, ranging from a single particle to a 10 by 10 cluster, with independent control of the x and y number of particles.

(ii) The spacing between particles can also be varied, again with independent control of x and y spacing.

(iii) In addition to using a regular array of particles, a user defined map may be used to generate irregular arrays, which is a more accurate reflection of the image shown in figure 7.12.

(iv) The tip magnetisation, the saturation magnetisation and dipole moment of the particles and the temperature can be varied.

These parameters were varied, is some cases using information obtained from experimental sources, and the results compared to the MFM measurements.

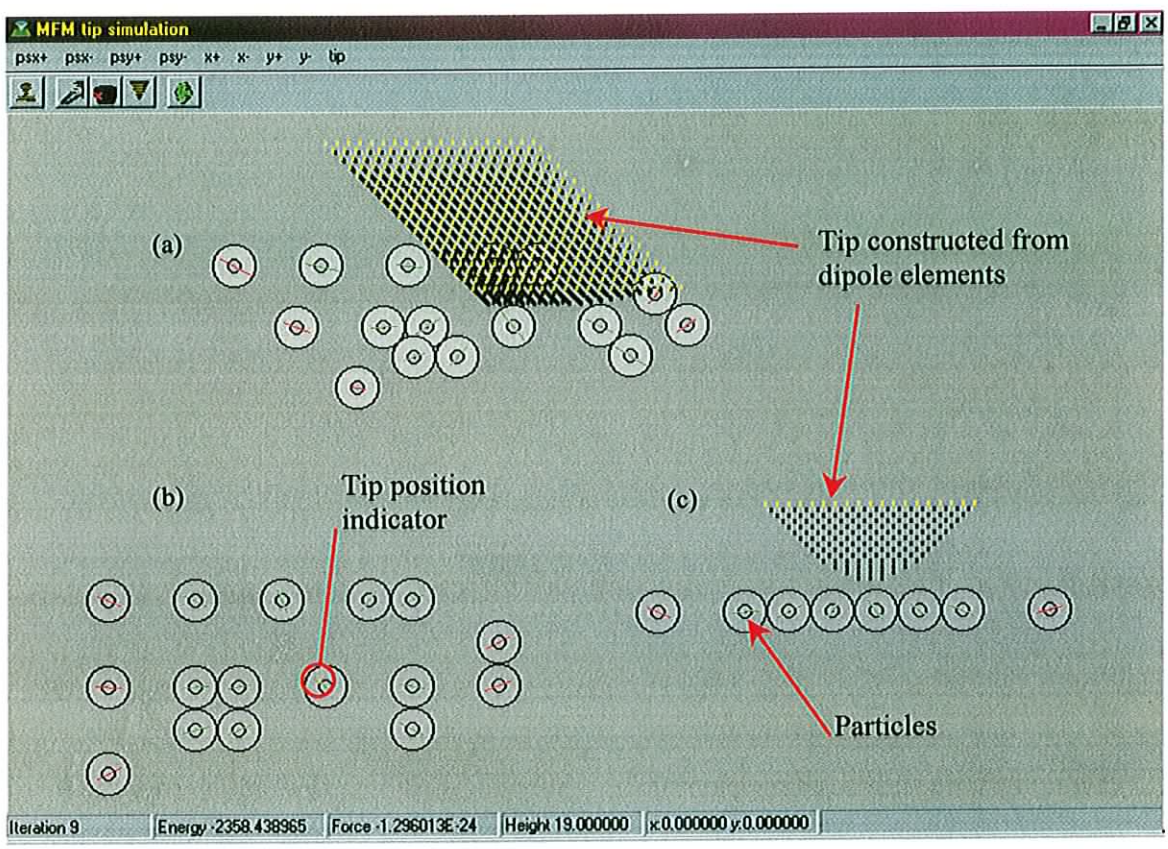

Figure 7.21: Screen shot of 3D calculation program. Regions a, b and c represent 3D, plan and side views respectively. The tip is omitted from the plan view and represented as a dot for clarity. Various calculated quantities can be seen in the status bar.

7.5.4 Results

The user defined map approach was used initially, for reasons stated above. An arrangement of a 2x2 cluster, a single particle and a 1x2 cluster was chosen, as it should show the contrast between single particles and 1- and 2-d clusters. The lift height was set to 5nm with an oscillation amplitude of ±1nm, yielding an equilibrium position of 5nm. The quantity μ, the magnetic dipole moment was taken from Park, et. al.,[18] to be 6.15×10^{-19}, where magnetic hysteresis measurements were fitted to the Langevin function to estimate μ for two interacting iron particles. Although the Mössbauer study suggested that the particles in this case were iron oxide, not iron, it is the closest indicator to a possible value. It seems in general that μ may be four or five orders of magnitude greater than the atomic value.[19] The tip magnetisation was set to 400,000A/m. This agrees reasonably with magnetisations used in calculations of other ferromagnetic materials.[20] The temperature was set to 298K for the purposes of the Langevin function. The tip shape was rounded with a radius approximating 25nm, which matched the tip specifications. The particle saturation magnetisation was then varied and force gradient images were obtained. The particle anisotropy, which takes the form of a constant applied magnetic field of random orientation for each particle, was set to zero, for reasons that will be explained in the discussion.

Figure 7.22 shows the results of these simulations. The force gradients were of the order of 10^{-3}N/m. As the particle's saturation magnetisation is varied from 1×10^{6}A/m to 1×10^{9}A/m the isolated particles response becomes prominent in the images as the particles in the clusters start to interact more strongly and become more difficult to align. At weaker values all particles can be aligned with equal ease and the clusters are therefore more responsive due to their higher particle density. These images are quantitatively similar to the MFM images, although the resolution is noticeably less. There is also a 'noise' in the images, which appears to be caused by a slight instability in the calculation of the energy minimum as M_s for the particle becomes appreciably greater than M_s for the tip. Closer investigation of this effect seemed to show that the noise was not random, as several repeat calculations revealed that it was really a selection of recurring values. It may be that as the particle M_s increases beyond that of the tip several low energy orientations become possible and the program has difficulty

picking the correct one. The underlying trend of the image is still clearly visible though.

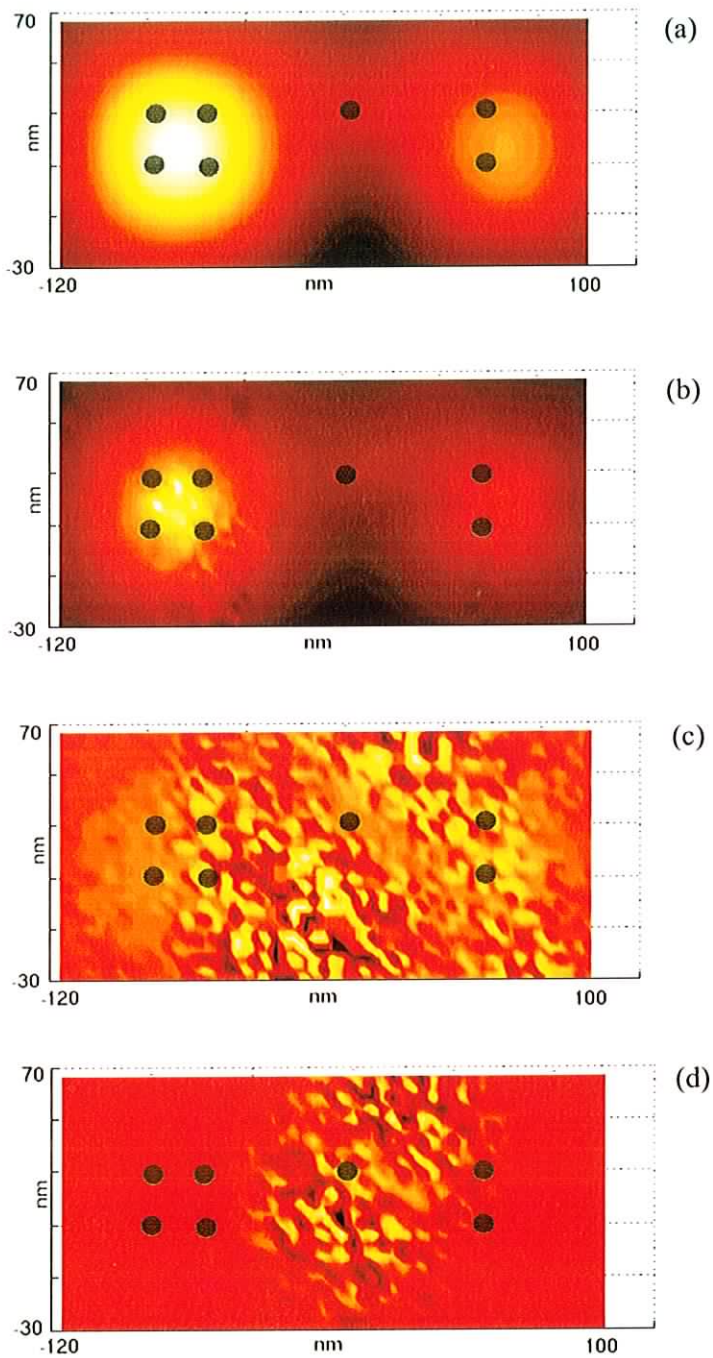

Figure 7.22: Simulations of the interaction of an MFM tip and a sample of particles. M_s for the tip is $4x10^5$ A/m. The images represent particle M_s of (a) $1x10^6$A/m, (b) $1x10^7$A/m (c)$1x10^8$A/m, and (d)$1x10^9$A/m. This shows the increasing prominence of the single particle, although the instrument resolution is hampered by 'noise'. The particle positions are indicated by dots.

To enhance these features, some images were smoothed by averaging for each point over all nearest neighbours. The results of this are shown for figure 7.22(c) and 7.22(d), in figures 7.23(a) and (b) respectively. Although smoothing is never really desirable as there is some information loss, in this case, in conjunction with 7.22 (a) and (b), the increasing prominence of the single particle with increasing M_s can be more clearly seen.

A slight edge effect is also visible around the edges of the clusters, consistent with expectations, although this is again swamped by the noise at higher particle M_s.

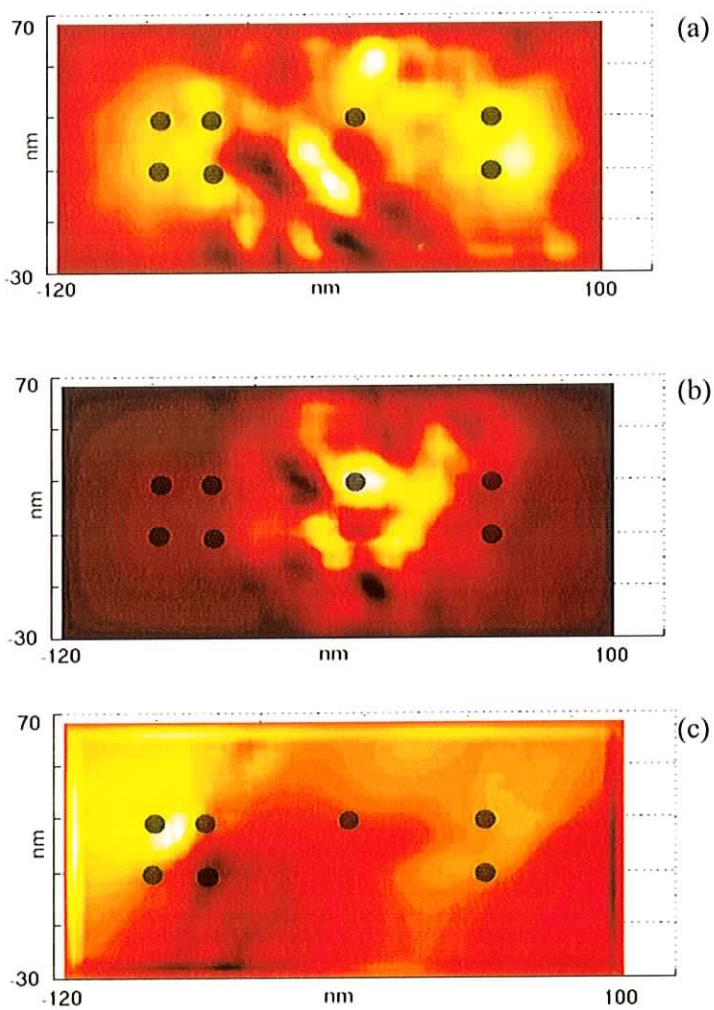

Figure 7.23: Processed images from figure 7.22. (a) and (b) are smoothed versions of 7.22(c) and (d) respectively. (a) shows the interactions over the cluster and isolated particle becoming comparable while (b) shows the single particle response. (c) is a differentiated copy of 7.22(b), showing a changing gradient over the cluster edges, running diagonally, consistent with an 'edge effect' of the type mentioned in the text.

This can be seen more clearly by differentiating figure 7.22(b). The result is shown in figure 7.23(c), which demonstrates a gradient change over the cluster edges, running diagonally top left to bottom right. which would be consistent with the presence of an 'edge effect'. This cannot be seen anywhere else on the image.

To determine the effect on instrument resolution, the tip radius was reduced to 10nm, although this is an impractical value for commercial tips at present. There was more lateral contrast in these images, shown in figure 7.24, This compares more favourably with the resolution of the MFM image in figure 7.12, and is unexpected given the tip specifications. This might suggest that the tip struck the surface, causing the formation of a sharper apex.

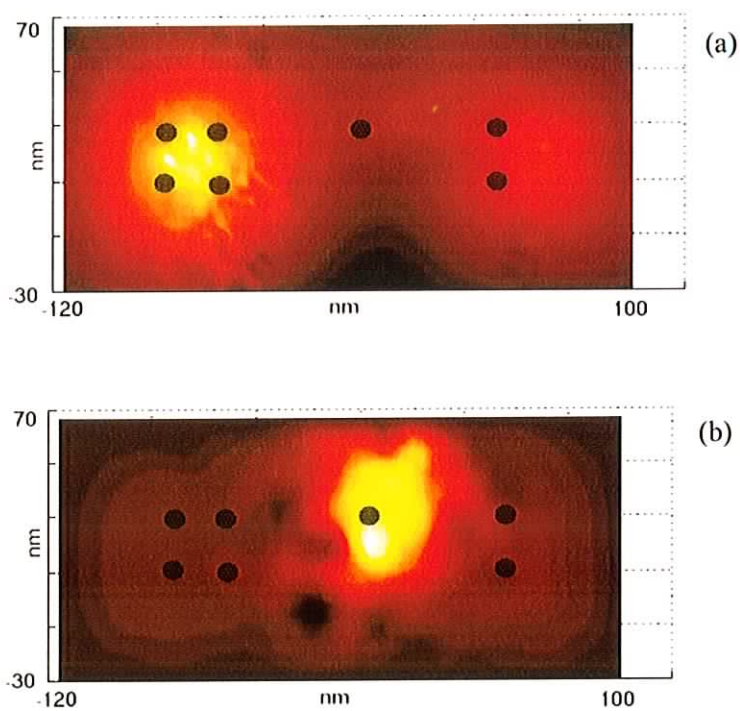

Figure 7.24: Images simulating a 10nm diameter tip. Tip M_s is again $4x10^5$A/m with particle M_s (a) $1x10^7$ A/m, which corresponds to figure 7.23(a) and (b) $1x10^9$ A/m, a smoother image corresponding to 7.23(b). Images show slightly enhanced resolution in comparison to those taken with the 25nm radius tip.

7.5.5 Discussion

Although this model is relatively simple the calculated images bear a close resemblance to the magnetic force gradient images. The model has some large limitations, however. It makes some arbitrary assumptions about the particle properties and those that need to be considered or neglected. There is no consideration of the internal structure of the particle. Although this is very important in determining the exact behaviour of a particle and the origin of the unusual properties, the MFM responds to dipolar forces which are relatively long range and is incapable in its current form of imaging internal structure. This in itself does not justify the absence of internal effect considerations, but the single domain superparamagnetic character and the presence of the polymer shell, which limits inter-particle interactions to dipolar, probably does. A comparison with the annealed cobalt particles would have been interesting, as direct particle to particle contact would be possible, which might have allowed exchange interactions to play a role. Due to the unavailability of tips with sufficiently small radius however, it wasn't possible.

The anisotropy field was set to zero in the calculations presented here. In principle, the Langevin function is only valid under conditions of low anisotropy. Calculations were initially carried out with fields of 1 to 10A/m. It was found that this variation had little effect on the generated images, and higher anisotropy seemed to increase the program instability. Setting the anisotropy to zero also had no effect on the generated images, but slightly reduced the instability. For that reason, images generated with zero anisotropy are presented here. It was noted that increasing the anisotropy tended to reduce the tips ability to align the isolated particle, making the images in 7.22(d), 7.23(b) and 7.24(b) more difficult to obtain. This would be expected, as increasing the anisotropy reduces the superparamagnetic behaviour of the particles. In addition, it would be expected that if the external field is larger than the anisotropy field, which, if the tip can align a superparamagnetic particle, it should be, then it may be assumed, at least for particles close to the tip, that the internal anisotropy has little significance. In reality, of course, the system is dynamic, and superparamagnetism itself is a time dependant quality and it is possible that the anisotropy would affect its response. This model is static however, so this consideration can be neglected.

The final impression is that the model used is very simple, while the system being modelled is so complex that consensus on a complete theoretical model, backed up by first principles calculations, does not yet exist. Despite this the model does give very good agreement with figure 7.12. This is perhaps the best justification for the assumptions used, and is possible due to the long range effects of the MFM and the polymer shell around the particles.

7.6 Summary

This chapter has demonstrated the application of a variety of instruments to Iron and Cobalt colloidal nanoparticle systems. AFM studies demonstrated that size distributions of the particles had an influence on the way they stacked together, with a smaller size distribution resulting in ordered arrangements.

Mössbauer spectroscopy of Iron particles indicated that they were composed of two different iron oxides and that no elemental iron was present, contrary to expectations. As iron oxide is normally antiferromagnetic, it is interesting that these particles are magnetic. XPS of cobalt particles suggested that the surface cobalt is neither pure cobalt nor cobalt oxide. This may be due to an unusual bonding configuration between the surface cobalt, the oxide coating and the polymer shell.

Magnetisation measurements performed using a SQUID magnetometer demonstrated that the Cobalt particles were superparamagnetic at room temperature and that the blocking temperature occurs somewhere between 150K and 200K. Optical magnetic measurements were unsuccessful, possibly because there wasn't enough material present to generate a measurable signal. The optical measurements did not seem to be sensitive enough to discriminate signal from background noise, but this will probably improve in the future. Dual AFM/MFM studies demonstrated an unusual effect in particle films, with a stronger response over isolated particles rather that clusters. It was speculated that this may be due to a pinning of the cluster particles' magnetic moments in the plane of the clusters. Simulations carried out using a dipolar model seemed to confirm this, as long as the particles saturation magnetisation, M_s, was sufficiently large, approximately 1×10^9A/m. This is somewhat large compared to typical values, but not unreasonable.

7.7 References

[1] e.g. R. Eisberg, R. Resnick, Quantum Physics Of Atoms, Molecules, Solids, Nuclei, and Particles, 2nd edition John Wiley & Sons, 1985

[2] H. Zijlstra, in: E. P. Wohlfarth (Ed.), Ferromagnetic Materials, Vol. 3, North-Holland, Amsterdam, 1982, pp. 37 105.

[3] L. Néel, J. de Phys. et le Rad., **15**, 225, (1954)

[4] J. L. Dormann, D. Fiorani, E. Tronc, J. Magn. Magn. Mater. **202**, 251 (1999)

[5] R. H. Kodama, J. Magn. Magn. Mater **200** 359 (1999)

[6] S. Sun, C.B. Murray, J. App. Phys., **85**, 4325, (1999)

[7] M. Tischer, O. Hjortstam, D. Arvanitis, J. Hunter Dunn, F. May, K. Baberschke, J. Trygg, J. M. Wills, B. Jahansson, O. Eriksson, Phys. Rev. Lett, **75**, 1602, (1995)

[8] D. Kechrakos, K. N. Trohidou, Phys Rev B, **58**, 12169 (1998),

[9] M. A. Zauska-Kotur, Phys. Rev. B., **54**, 1064, (1996)

[10] K. Nakamura, H. Hasegawa, T. Oguchi, K. Sueoka, K. Hayakawa, K. Mukasa, Phys. Rev. B., **56**, 3218, (1997)

[11] D. Schmeißer, O. Böhme, A. Yfantis, T. Heller, D. R. Batchelor, I. Lundstrom, A. Lloyd Spetz, Phys. Rev. Lett., 83, 380, (1999)

[12] S. Yamamuro, K. Sumiyama, T. Kamiyama, K. Suzuki, J. App. Phys., **86**, 5726 (1999)

[13] H. Ibach, H. Lüth, Solid State Phys., Springer Verlag, (1991)

[14] R. Michellotto, H. Fukuda, M. Ohtsu, Langmuir, **11** , 3333, (1995)

[15] first published, Ordeningen magnetische eigenschappen van colloïdale izjerdeeltjes met polymeercoating, J.M.Sturm, 1999.

[16] T. Stifter, O. Marti, B. Bhushan, Phys. Rev. B., **62**, 13667, (2000)

[17] *personal communication, Kees Flipse, magnetisation experiments performed in University of Utrecht.*

[18] Y. Park, S. Adenwalla, G.P. Felcher, S. D. Bader, Phys.Rev. B., **52**, 12779, 1995

[19] M.F. Hansen, S. Mørup, J. Mag. Mag. Mater.,**184**, 262, (1998)

[20] M. Kleiber, F. Kümmerlen, M. Löhndorf, A. Wadas, D. Weiss, R. Wiesendanger, Phys. Rev. B. **58**, 5563, (1998)

Chapter 8

Conclusions

8.1 General Review

Low dimensional structures are playing an increasing role in materials science research and the electronics industry, as they can display novel optical, magnetic, and electrical properties.

This work has concentrated on the optical and magnetic properties of quantum wires and dots. The principle aim was to conduct this examination using a variety of optical techniques, backed up by other complimentary techniques.

The controlled deposition of indium onto Si(111) and Si(100) surfaces produces apparent wire type structures, which are only a few atoms wide, making them ideal quantum wire candidate systems. Uncertainty about the physical structure of the wires prompted an STM investigation, and the one-dimensional character was probed using RAS.

Iron and cobalt nanoparticles were also studied with a variety of techniques. Principally, the aim was to investigate if optical magnetometry techniques could be used to study the magnetic layers of superparamagnetic articles. These were backed up by other, non-optical measurements such as MFM and SQUID. The MFM measurements were supported by dipolar model calculations.

8.2 Indium on Silicon

Indium on silicon was studied using RAS and STM. The RAS was constructed locally, with a design following that of Lou, et. al.,[1] and optimised for compactness. Most components were off the shelf, such as mirrors and the PEM. The monochromator was also selected as one of the most compact available. Both photomultiplier tube and photodiode techniques were investigated as detectors, the pm tube being selected due to electronic problems with the photodiode amplifier. The

instrument was used to investigate electron confinement in the wires. The physical structure was investigated using STM.

The study of the Si(111)-4x1-In surface helped to shed light on some unanswered questions about the reconstruction. Seemingly contradictory experimental data had led to the emergence of two conflicting models for the surface atomic configuration. The STM demonstrated a considerable structural resemblance to a calculated charge density image[2] for Bunk's hypothesised model of the surface, adding weight to its validity as the correct model. Aside from Bunk's own SXRD work[3], this is the first direct observation of this structure to date. The RAS study gave a strong indication of electron confinement along the apparent In chains, showing strong anisotropy at 1.9eV. Photoemission and inverse photoemission studies from Abukawa, et. al.,[4] and Hill, et. al.,[5] indicate states that may be involved in this transition.

RAS and STM were also applied to the Si(100)-4x3-In system. The STM images again seemed to show chains and provided support for Bunk's proposed model of the system.[6] The system had a weaker RAS response than Si(111)-4x1-In, with a magnitude of ~3 x 10^{-3} at approximately 2.1eV.

In general, Si(111)-4x1-In has proved to be a very interesting and much studied system. Recently, G. Le Lay,[7] et. al., performed low temperature photoemission, which seemed to suggest a Fermi to Luttinger liquid transformation. Had time and resources permitted, it would have been interesting to apply the RAS to the low temperature system to investigate what effects the apparent transition to a truly one dimensional system would have on the optical response, and at what temperature this occurs.

8.3 Magnetic Nanoparticles

Cobalt nanoparticles with well controlled regularity and size distributions were obtained on HOPG substrates from IBM, and iron particles of various sizes and size distributions were obtained from the University of Utrecht in a decaline solution. SQUID measurements demonstrated the transition from ferromagnetic to superparamagnetic behaviour, but in the time permitting, they were only applied to a

single sample of cobalt particles. The optical magnetometry techniques unfortunately did not prove as successful at measuring the magnetic nanoparticles as was hoped. While the techniques are still both useful and powerful they were not suited to these systems in their present forms. Perhaps stronger magnetic fields or more sensitive signal detection and isolation will in the future allow better application to superparamagnetic systems.

The AFM/MFM combinations revealed an unusual effect on a nanoparticle sample. There was a stronger response from isolated particles, and for regions where the AFM image shows particle clusters the response was much smaller, with only a slight response around the edges of the clusters. It was hypothesised that particle interactions within the clusters might be pinning the cluster magnetic moments in-plane, allowing the tip to align the isolated particles only. This was investigated using a dipolar model. The model was investigated with limited success using two-dimensional finite element analysis. A fully three-dimensional model was implemented in C++, which proved more successful in validating the proposed model.

8.4 The Future

There has been a lot of work on low dimensional systems in recent years, but there is still a lot that is not understood, and technological advances provide an impetus for this research to continue.

Quantum wire materials will be needed if molecular electronic devices are to be realised. Real one-dimensional metals are difficult to find, and the evidence of quantum confinement found here, in addition to the work by Le Lay and colleagues, suggest that the Si(111)-4x1-In systems are excellent candidates for further research into the behaviour of one-dimensional metals. Although it is unlikely that they could be used for practical applications, they are nevertheless valuable as test systems, increasing the knowledge and understanding of such systems that will be required when nanotechnology reaches maturity.

Quasi zero-dimensional particles are more abundant and easier to produce, although they can be more difficult to deal with theoretically due to their size. The MFM study showed that particle interactions could be crucial in determining the behaviour of a particle array. Measurements conducted on samples with different

particle sizes, varied spacing and particle density would help to characterise this behaviour.

There is, therefore, much work, both experimental and theoretical, remaining to be done on nanoparticle systems. Experiments such as those detailed in this work demonstrate the behaviour and properties, but successful integration into nanoelectronic or spintronic devices will require further investigation and understanding of nanoparticle properties, and how to control these properties by varying particle size and composition, which is not a trivial procedure. They will then need to be integrated with nanowire materials to form a functioning device. Improving production techniques for producing different particle shapes, particles composed of alloys and those with dissimilar metal coatings, and wires, will ensure continued interest in this field.

8.5 References

[1] J. S. Luo, J. M. Olson, K. A. Bertness, M. E. Raikh, E. V. Tsiper, J. Vac. Sci. Technol. B **12**, 2552 (1994)

[2] J. Nakamura, S. Watanabe, M. Aono, Phys. Rev. B, 63, 193307, (2001)

[3] O. Bunk, G. Falkenberg, J. H. Zeysing, L. Lottermoser, R. L. Johnson, M. Nielsen, F. Berg-Rassmussen, J. Baker, R. Feidenhans'l, Phys. Rev. B, 59, 12228, 1999

[4] T. Abukawa, M. Sasaki, F. Hisamatsu, T. Goto, T. Kinoshita, A. Kakizaki, S. Kono, Surf. Sci. 325 33 (1995)

[5] I. G. Hill, A. B. McLean, Phys. Rev. B. **56**, 15725, (1997)

[6] O. Bunk, G. Falkenberg, L. Seehofer, J. H. Zeysing, R. L. Johnson, M. Neilsen, R. Feidenhans'l, E. Landemark, App. Surf. Sci, 123/124, 104, (1998)

[7] G. Le Lay, S. Hasegawa, V.Y. Aristov, L. Giovanelli, S. Takeda, H. Enriquez, V. Derycke, P. Soukiassian, R. Belkhou, A. Taleb-Ibrahimi, *to be published.*

Appendix A

Components Suppliers and Parts

Lock-in Amplifier
EG&G 5210

EG&G Ltd.
Sorbus House
Mulberry Business Park
Wokingham
Berks.
RG41 2GY
United Kingdom

Low Strain Bakeable Viewport
PVP-275

EPI Europe
147 Chorley New Road
Horwich
Bolton
BL6 5QE
Greater Manchester
UK

Monochromator
Digikrom CM110

Elliot Scientific Ltd.
Gladstone Place
36-38 Upper Marlborough Road
St. Albans
Herts
AL1 3US
UK

Photodetectors
R955 photomultipler tube and S1227-66BQ photodiodes

Hamamatsu Photonics
Lough Point
2 Gladbeck Way
Windmill Hill
Enfield
Middlesex
EN2 7JA
UK

Mirrors
25.4 mm diameter, focal lengths 150, 200, 250 and 500 mm

Coherent Ealing Europe Ltd.
Greyciane Road
Watford
WD2 4PW
UK

Lamp
L2194-02 with C4262-01 power supply, E2419 Housing and C4251 High Voltage Starter

Hamamatsu Photonics
Lough Point
2 Gladbeck Way
Windmill Hill
Enfield
Middlesex
EN2 7JA
UK

Polarisers
Model PBS10M Glan Taylor polarisers

Halbo Optics
83 Haltwhistle Road
South Woodham Ferrers
Chelmsford
CM3 5ZA
UK

PhotoElastic Modulator
Hinds PEM 90 with FS 50 optical head.

The Roditi International Corp. Ltd.
Carrington House,
130 Regent Street
London W1R 6BR
UNITED KINGDOM

Quickfield
Tera Analysis Ltd
Knasterhovvej 21,
DK-5700 Svendborg, Denmark
Phone: +45 6354 0080
Fax: +45 6254 2331

Appendix B

C++ Code for MFM Simulations.

Code to simulate the MFM tip-sample interaction was written using Borland C++ Builder 4.0 Professional Edition. This appendix shows only the code relevant to the simulation, as the full code for graphics, UI etc. is quite large and not necessary to understand the program. The GUI was created using the Rapid Application Development environment provided in C++ Builder and the code is dependent on its vcl libraries. The source code will therefore not compile with other C++ compilers.

The diagram in figure 9.1 gives an indication of the quantities used in the program. In practise, each tip element block is represented by a point in the program, separated from adjacent points by the dimensions *ddx*, *ddy* and *ddx*. These separations are varied to simulate a rounded tip, changing when the number of points along a side of the tip is equal to the quantity waist. The height between the bottom of the tip and plane through the centre of the particles is represented by *h*, while *w* and *d* represent the x and y separation between particles.

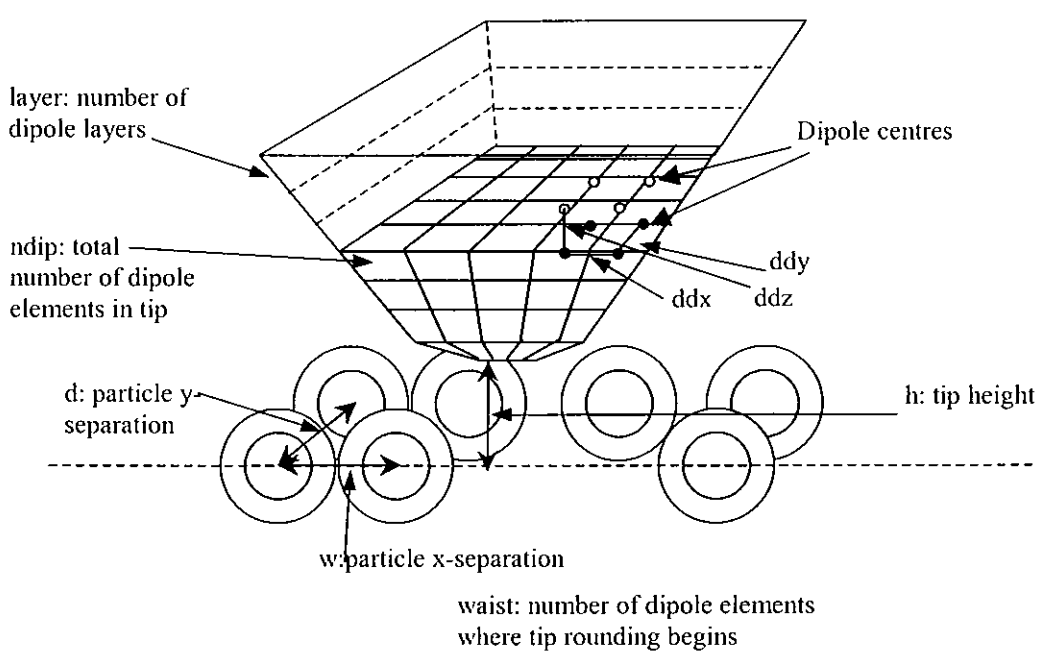

Figure 9.1: An indication of the geometry used in the program and the variables used to control certain key features.

```
__fastcall TForm1::TForm1(TComponent* Owner)
        : TForm(Owner)
{       layer=14; h=15; w=0; ddx=8;ddy=8;ddz=4
        L=50; a=30;b=30; d=0;

         if((fp=fopen("config.mfm","r"))!=NULL)
         {
          fread(str1, sizeof str1, 1, fp);
          filecounter=atoi(str1);
        fclose(fp);
        }
        else
        {filecounter=0;}
       //Initial Conditions
        Form1->tipmag=1E6;
        Form1->maxmag=1E6;
        Form1->mu=6.15E-19;
        Form1->mur=(1/(4*M_PI));
        Form1->T=298;
        Form1->flatness=0;
        Form1->Waist=4;
        Form1->amplitude=2;
        Form1->Hani=20;
        for(int i=0;i<6;i++)
         { for(int j=0;j<10;j++)
           { Form1->usermap[i][j]=map[i][j];
           }
         }
         if(cont==0){for (j=0;j<nsy1;j++){
              for  (i=0;i<nsx1;i++)

              {
                  Particle[i][j]=new TParticle ;
                    }
              }
              for (i=0;i<nn;i++)
              {
                    Tipelement[i]= new TTip;
                    }
             cont++;}
       cltop=RGB(0,0,0);
       cltip=RGB(233,252,3);
       clspinup=RGB(0,255,0);
       clspindown=RGB(255,0,0);
       anisotropy();
       drawscene();

}

void __fastcall TForm1::drawscene ()
```

```
{   cleardevice();
    InitSpins();
    Init_Tip();
    Fill_Hdip_Tip();
    Set_Random();
    E=1.0E12; teller=0;
    do
    {
        E0=E; teller++;
        Calc_M(0);
        E=Calc_E();
        sprintf(str,"Iteration %d", teller);
        StatusBar1->Panels->Items[0]->Text=str;
        sprintf(str,"Energy %e", E);
        StatusBar1->Panels->Items[1]->Text=str;
        Ediffabs=(E0-E);
        if(Ediffabs<0.0) Ediffabs=-Ediffabs;
        if (E<0.0) Eabs=-E;
    } while (((Ediffabs>Form1->criteria*Eabs) && (teller<1000)));
    Force();
    DrawSpins(nsx,nsy);
    drawtip();
    drawvertical(w-ddx/2, d-ddy/2, 0.0, w-ddx/2, d-dy/2, 0.0, vertoffsetx,
                 vertoffsety, 1);
}

void __fastcall TForm1::cleardevice()
{   Image1->Canvas->Brush->Color=RGB(150,150,150);
    Image1->Canvas->Pen->Color=RGB(191,191,191);
    Image1->Canvas->Rectangle(0,0,
                              GetSystemMetrics(SM_CXFULLSCREEN),
                              GetSystemMetrics(SM_CYFULLSCREEN)
                              );
    Image1->Canvas->Pen->Color=RGB(0,0,0);
}

void __fastcall TForm1::InitSpins()
{
for (j=0;j<ax;j++)
    { for  (i=0;i<ay;i++)
        {if(map[j][i]==1)
            {Particle[j][i]->x=((-0.5*(10)+i)*a);
             Particle[j][i]->y=((-0.5*(4)+j)*b);}
        }
    }
}

void __fastcall TForm1::Init_Tip()
{   int i,j,k,h1,c=0;
    float x,y,z,n;
```

```
    ndip=-1;
    z=h;
    n=Form1->Waist;
    for (i=Form1->flatness;i<=layer;i++)
    {   if (i<n)c=i; else c=n;
            h1=i+c;
            for (j=0;j<=h1;j++)
            {   for (k=0;k<=h1;k++)
                {
                x=((-0.5*(h1-1)+j-1)*ddx)+w;
                y=((-0.5*(h1-1)+k-1)*ddy)+d;
                ndip++;
                Tipelement[ndip]->x=x;
                Tipelement[ndip]->y=y;
                Tipelement[ndip]->z=z;
                Tipelement[ndip]->mz=Form1->tipmag;
                if(((k==0)&&(j==0))&&(i==layer))tipdim=ndip;
                }
            }
        z+=ddz;
        }
    }
}

void __fastcall TForm1::Fill_Hdip_Tip()
{
    int i,j,k;
    float hx,hy,hz,Hx,Hy,Hz,x,y;
    {   for (k=0;k<ay;k++)
        {
            for (i=0;i<ax;i++)
            {   x=Particle[i][k]->x;
                y=Particle[i][k]->y;
                Hx=0.0; Hy=0.0, Hz=0.0;
                for (j=1;j<=ndip;j++)
                {
                    H_calc(x,y,0.0,
                            Tipelement[j]->x,Tipelement[j]->y,Tipelement[j]->z,
                            0.0,0.0,Tipelement[j]->mz,hx,hy,hz);
                    Hx+=hx; Hy+=hy; Hz+=hz;
                }
            Particle[i][k]->hsx=Hx+Particle[i][k]->xani;
            Particle[i][k]->hsy=Hy+Particle[i][k]->yani;
            Particle[i][k]->hsz=Hz+Particle[i][k]->zani;
            }
        }
    }
}

void __fastcall TForm1::Set_Random()
```

```
{
int i,j;
float fi,fk;
for (i=0;i<ax;i++)
    {   for (j=0;j<ay;j++)
        {fi=2.0*M_PI*random(1000)/1000.0;
        fk= 2.0*M_PI*random(1000)/1000.0;
        Particle[i][j]->msx=cos(fi)*cos(fk)*Form1->maxmag;
        Particle[i][j]->msy=sin(fi)*cos(fk)*Form1->maxmag;
        Particle[i][j]->msz=sin(fk)*Form1->maxmag;
        Particle[i][j]->ms=Form1->maxmag;
        }
    }
}

void __fastcall TForm1::DrawSpins(int nsx, int nsy)
{
    for (int j=0; j<ax;j++)
        {for (int i=0; i<ay; i++)
            {if(map[j][i]==1)
                {DrawArrow(Particle[j][i]->x,Particle[j][i]->y,
                        Particle[j][i]->msx, Particle[j][i]->msy,-Particle[j][i]->msz,
                        Particle[j][i]->ms);
            }
        }
    }
}
void __fastcall TForm1::DrawArrow(int x, int y, float ex, float ey, float ez, float l)
{
 float x1,y1,x4,y4,z1,z4,t1,t2;
 float e,cf,sf,sfz,cfcd,sfsd,sfcd,cfsd;
 e=sqrt(ex*ex+ey*ey+ez*ez);
 cf=ex/e;
 sf=ey/e;
 sfz=ez/e;
 l=(l/Form1->maxmag)*20;
 if (l>20)l=20;
 t1=(l*cf/2.0);
 t2=(l*sf/2.0);
 cfcd=cf*cd; sfsd=sf*sd; sfcd=sf*cd; cfsd=cf*sd;
 x1=x+t1; y1=y+t2; z1=(l*sfz/2.0);
 x4=(x-t1);
 y4=(y-t2);
 z4=(-(l*sfz/2.0));
 l=0.25*l;
 Image1->Canvas->Pen->Width=3;
 Image1->Canvas->Pen->Color=RGB(0,0,0);
 drawobject(x,y,0,x,y,0,mainoffsetx,mainoffsety,0);
 drawvertical(x,y,0,x,y,0,vertoffsetx,vertoffsety,0 );
 drawhorizontal(x,y,0,x,y,0,horizoffsetx,horizoffsety,0 );
```

```
 if (z4>=z1){Image1->Canvas->Pen->Color=clspinup;
                Image1->Canvas->Pen->Width=1; }
 else {Image1->Canvas->Pen->Color=clspindown;
 Image1->Canvas->Pen>Width=1;}
 drawobject(x1,y1,z1,x4,y4,z4,mainoffsetx,mainoffsety,1);
 drawvertical(x1,y1,z1,x4,y4,z4,vertoffsetx,vertoffsety,1);
 drawhorizontal(x1,y1,z1,x4,y4,z4,horizoffsetx,horizoffsety,1);
}

void TForm1::anisotropy()
{int i,j;
float fi, fk;
for (i=0;i<ax;i++)
    {
    for (j=0;j<ay;j++)
        if(map[i][j]==1)
        {fi=2.0*M_PI*random(1000)/1000.0;
        fk= 2.0*M_PI*random(1000)/1000.0;
        Particle[i][j]->xani= cos(fi)*cos(fk)*Form1->Hani;
        Particle[i][j]->yani= cos(fi)*cos(fk)* Form1->Hani;
        Particle[i][j]->zani= cos(fi)*cos(fk)* Form1->Hani;
        }
    }
}

void __fastcall TForm1::Calc_M(int e)
{
int h,i,j,k;
float x,y,hx,hy,hz,mx; //,my,mz
float Hx,Hy,Hz,Hxx,Hyy,Hzz,H;
H=Hx=Hy=Hz=0;
for (k=0;k<ay;k++)
    {for (i=0;i<ax;i++)
        {if (map[i][k]==1)
            {Hx=Particle[i][k]->hsx;//hdipx[i][k];
            Hy=Particle[i][k]->hsy;//hdipy[i][k];
            Hz=Particle[i][k]->hsz;//hdipz[i][k];
            x=Particle[i][k]->x; y=Particle[i][k]->y;
            for (j=0;j<ay;j++)
                {for (h=0;h<ax;h++) if ((h!=i)||(j!=k))
                    {
                    if(map[h][j]==1)
                        {
                        H_calc(Particle[i][k]->x,Particle[i][k]->y,0.0,
                               Particle[h][j]->x,Particle[h][j]->y,0.0,
                               Particle[h][j]->msx,
                               Particle[h][j]->msy,
                               Particle[h][j]->msz,
                               hx,hy,hz);
                        Hx+=hx; Hy+=hy; Hz+=hz;
```

```
                        }
                    }
                }
                Particle[i][k]->hsx=Hx;
                Particle[i][k]->hsy=Hy;
                Particle[i][k]->hsz=Hz;
                if (e==0)
                    {Hxx= Hx+Particle[i][k]->xani;
                    Hyy= Hy+Particle[i][k]->yani;
                    Hzz= Hz+Particle[i][k]->zani;
                    H=sqrt(Hxx*Hxx+Hyy*Hyy+Hzz*Hzz);
                    Particle[i][k]->hs=H;
                    yx=(Form1->mu*(H))/(kboltz*Form1->T);
                    Particle[i][k]->msx=Form1->maxmag*Langevin(yx)
                    *(Hxx/(sqrt(H*H-Hzz*Hzz)));
                    Particle[i][k]->msy=Form1->maxmag*Langevin(yx)
                    *(Hyy/(sqrt(H*H-Hzz*Hzz)));
                    Particle[i][k]->msz=Form1->maxmag*Langevin(yx)
                    *(Hzz/H);
                    Particle[i][k]->ms=sqrt(Particle[i][k]->msx*Particle[i][k]->msx+
                                            Particle[i][k]->msy*Particle[i][k]->msy+
                                            Particle[i][k]->msz*Particle[i][k]->msz);
                }
            }
        }
    }
}

float __fastcall TForm1::Calc_E()
{
int i,j;
double E=0.0;
Calc_M(1);
for (j=0;j<=ay;j++)
    {for (i=0;i<=ax;i++)
        {if(map[i][j]==1)
            {E-=(Particle[i][j]->msx*Particle[i][j]->hsx+
                Particle[i][j]->msy*Particle[i][j]->hsy+
                Particle[i][j]->msz+Particle[i][j]->hsz)/1e70;}
            }
        }
    }
return E;
}

void __fastcall TForm1::H_calc(float x, float y, float z, float x0, float y0, float z0,
                    float mx, float my, float mz, float &Hx, float &Hy, float &Hz)
{float dx,dz,dy,r2,r5,t;
 dx=(x-x0)*1E-9; dy=(y-y0)*1E-9; dz=(z-z0)*1E-9;
 r2=dx*dx+dy*dy+dz*dz; r5=r2*r2*sqrt(r2);
```

```
  t=3.0*(mx*dx+my*dy+mz*dz);
  Hx=((t*dx-mx*r2)/r5);
  Hy=((t*dy-my*r2)/r5);
  Hz=((t*dz-mz*r2)/r5);
}

float __fastcall TForm1::Langevin(float y)
{   float p,e2y;
    double  y2=y*y ;
    if (y<0.5) {p=y*(0.3333333333+y2*(-0.02222222222+y2*(0.002116402116
                +y2*(-0.0002116402116+y2*0.00002137779916)))); }
        else
            if (y<20.0) {e2y=exp(-2.0*y); p=(1.0+e2y)/(1.0-e2y)-1.0/y;}
             else
                {p=1.0-1.0/y;}
return p;
}
double __fastcall TForm1::Force()
{   double sqr2,mm,m1,v,vt,r3,r2,r1,r, f=0, F=0;
    r3= (5e-9)*(5e-9)*(5e-9);
    v=(4/3)*M_PI*r3;
    vt=ddx*ddy*ddz*1e-27;
    int i,j,k;
    for(k=0;k<=ndip;k++)
    {   for ( i=0;i<ax;i++)
        {   for (j=0;j<ay;j++)
            if(map[i][j]==1)
                {r2=((((Particle[i][j]->x)-(Tipelement[k]->x))*1E-9)
                    *(((Particle[i][j]->x)-(Tipelement[k]->x))*1E-9)
                    + (((Particle[i][j]->y)-(Tipelement[k]->y))*1E-9)
                    *(((Particle[i][j]->y)-(Tipelement[k]->y))*1E-9)
                    +(((Particle[i][j]->z)-(Tipelement[k]->z))*1E-9)
                    *(((Particle[i][j]->z)-(Tipelement[k]->z))*1E-9));
                    mm=((Particle[i][j]->msx*v)*(Tipelement[k]->mx*vt)
                    + (Particle[i][j]->msy*v)*(Tipelement[k]->my*vt)
                    + (Particle[i][j]->msz*v)*(tipmag*vt));
                    if ((Form1->mur*r2)!=0)f=mm/((1e-7)*r2);
                    r1= (((Particle[i][j]->z)-(Tipelement[k]->z))*1E-9);
                    sqr2=sqrt( r2);
                    if (sqr2!=0){r=r1/ sqr2;
                    F+=(f*r);}
                    }
                }
            }
    sprintf(str,"Force %eF", F);
    StatusBar1->Panels->Items[2]->Text=str;
    return F;
}
```

Appendix C

Simple Matlab Scripts for Data Smoothing and Differentiation

Image differentiation.

This script differentiates an force gradient surface of the type produced by the MFM simulation program. It does this by obtaining x and y vectors, tangential to the surface at an point p, and finding the slope of the resultant. 55 x 25 is the standard data matrix size produced by the program.

```
z3=zeros(55,25);
R=0;
for n=2:54
    for m=2:24
        R = (z2(n+1,m)-z2(n-1,m)+z2(n,m+1)-z2(n,m-
            1))/2.8284;
        z3(n,m) = R;
    end
end
surf(z3,'facecolor','interp','edgecolor','none')
```

Image Smoothing.

This smoothes an image by averaging over the height of each nearest neighbours.

```
z2=zeros(55,25);
t=0;
av=0;
for n=2:54
    for m=2:24
        t=0;
        for i=n-1:n+1
            for k=m-1:m+1
                t=t+z1(i,k);
            end
        end
        av=t/9;
        z2(n,m)=av;
    end
end
z1=z2;
surf(z2,'facecolor','interp','edgecolor','none')
```

Appendix D: LabVIEW Program for RAS Instrument Control

This appendix demonstrates the LabVIEW software written to control the RAS spectrometer. The program shown here sets parameters for the lock-in amplifier, monochromator and PEM controller, reads AC and DC signals from the lock-in and represents the AC, DC and RAS on screen.

The main program is contained inside a sequence loop, which ensures correct sequential execution. All variables and datatypes outside the loop are program settings or data access terminals.

'Set energy range' determines the initial and final energies that are scanned, and step is the magnitude of each incremental step between them. 'Monochromator', 'PEM' and 'Lockin' are integers representing the serial ports that the devices are attached to. 'AC in/out', 'DC in/out' and 'RAS in/out' return the respective numerical values of these quantities as the instrument is scanning. They are useful for diagnosing problems and are otherwise not used

Frame 0/7

This frame generates an array of values, beginning at the initial photon energy the monochromator is set to, and incrementing in values of the selected step size until it reaches the final value. This will alter be converted into Angstroms and used to control the monochromator.

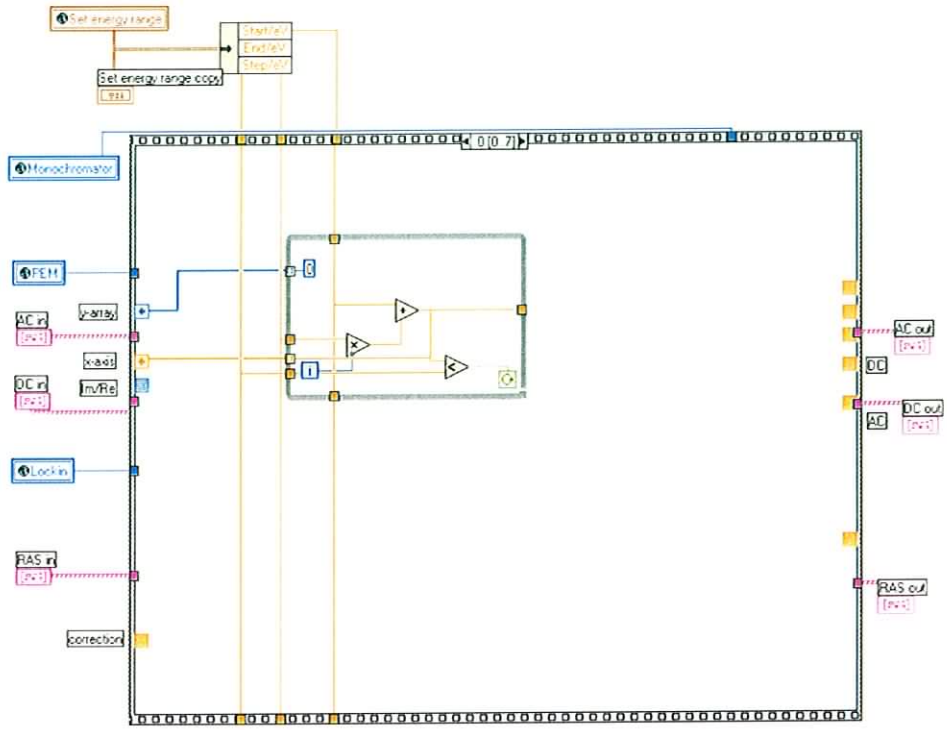

Frame 1/7

The 'Real/Imaginary' global variable is used to switch the lock-in amplifier into *f* or *2f* mode (see Chapter 4), thereby selecting between the real and imaginary parts of the RAS response.

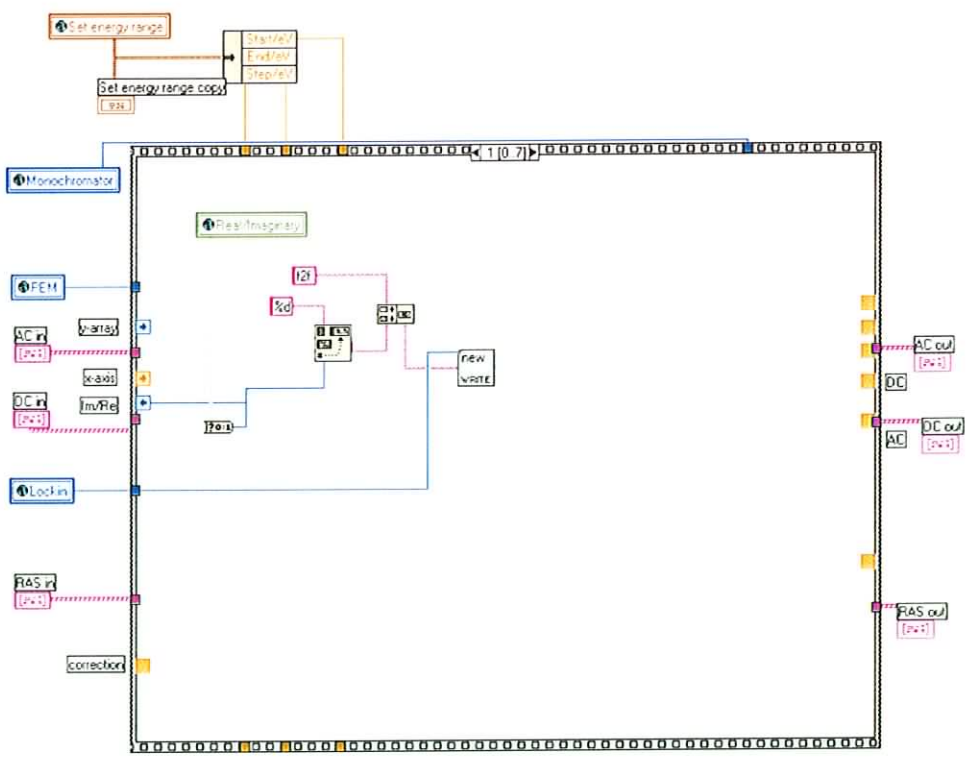

Frame 2/7

This frame sets the monochromator to the starting energy, and waits for a certain delay time, in this case 1.5 seconds, before moving to the next frame. This gives the instrument sufficient settling time at the new energy.

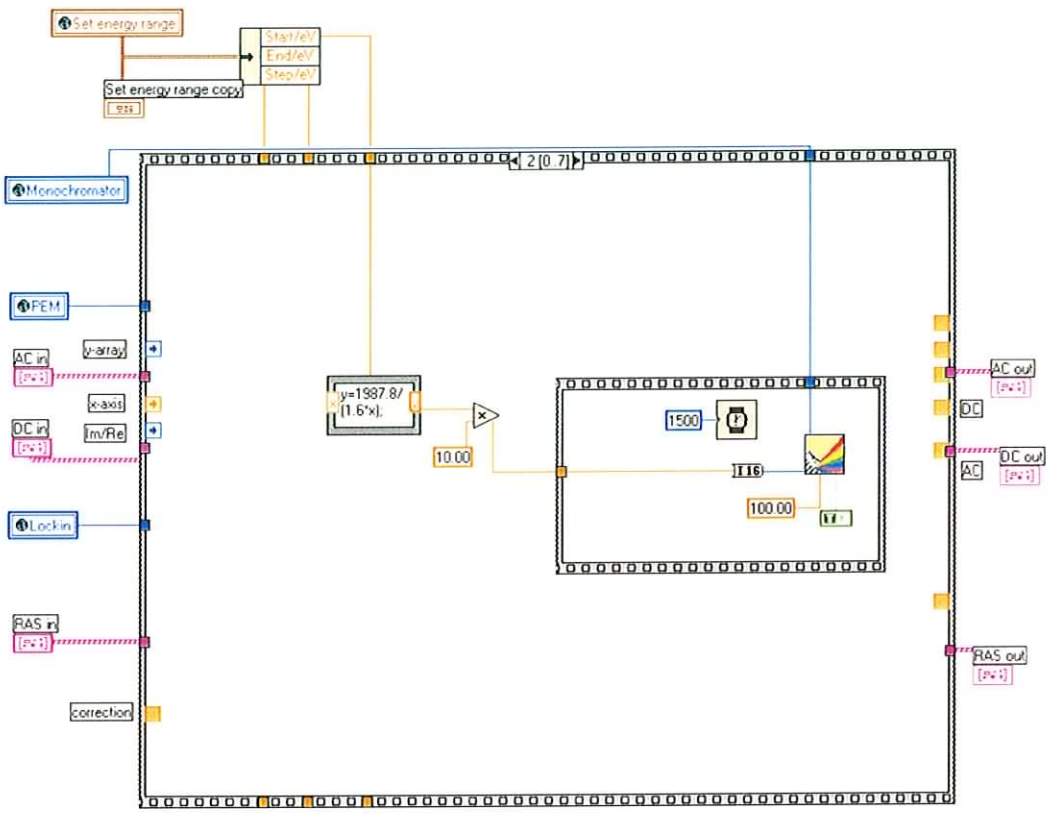

Frame 3/7.

This sets retardation of the PEM. Depending on the vaule of the 'Real/Imaginary' global, this will be set to 0.486 or 0.584, for real or imaginary operation respectively. The empty frames of the case structure are also shown. It is used in this case to ensure correct execution order, in a similar way to a sequence loop.

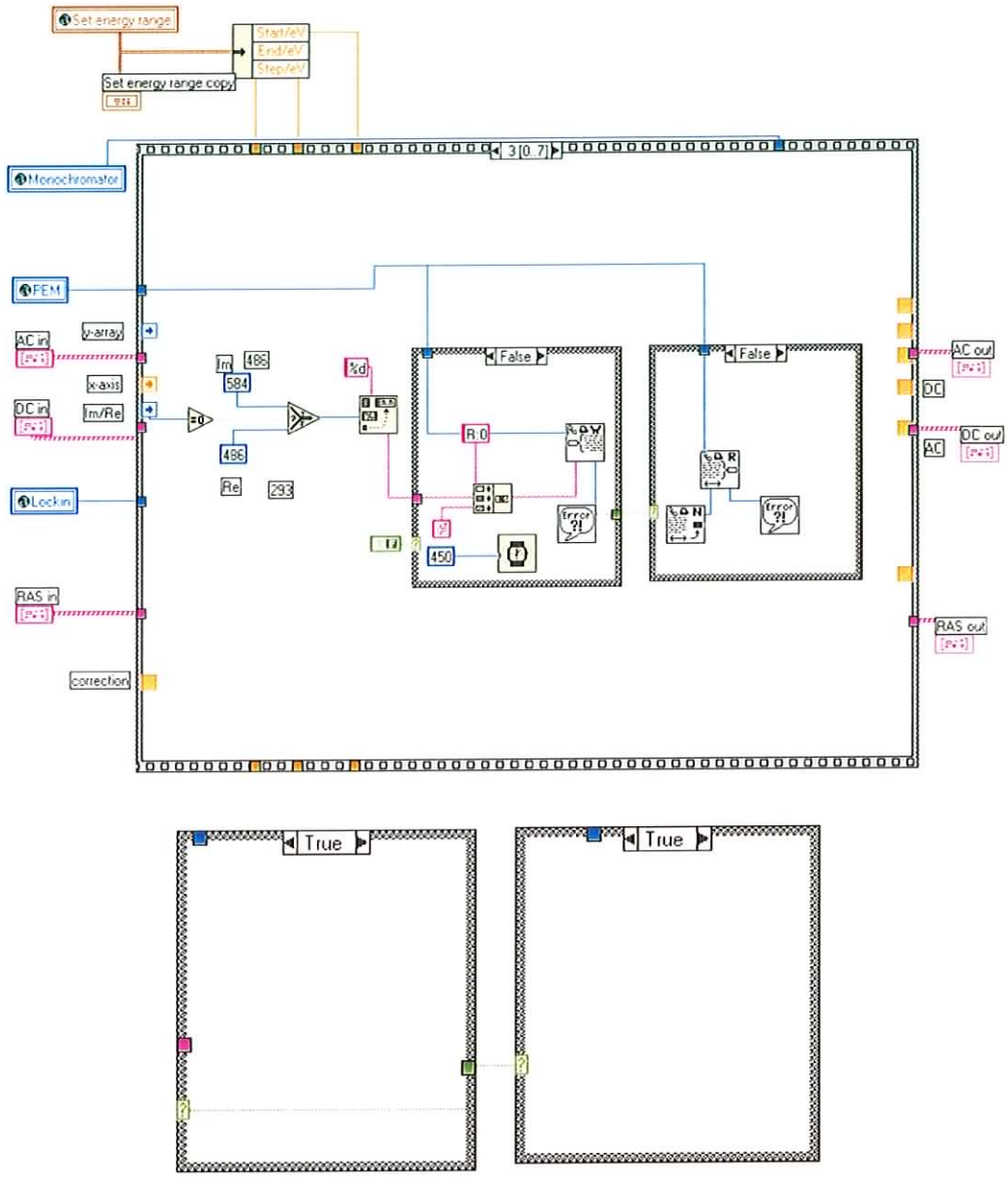

Frame 4/7

This frame determines of a window correction is required, from the value of the 'Corrected/Uncorrected' global variable. If a correction is required, a previously saved correction file, whose path is determined by the 'File locations' variable, is loaded. If not, an identically sized array with each element set to zero is used, as the program always expects to perform a correction.

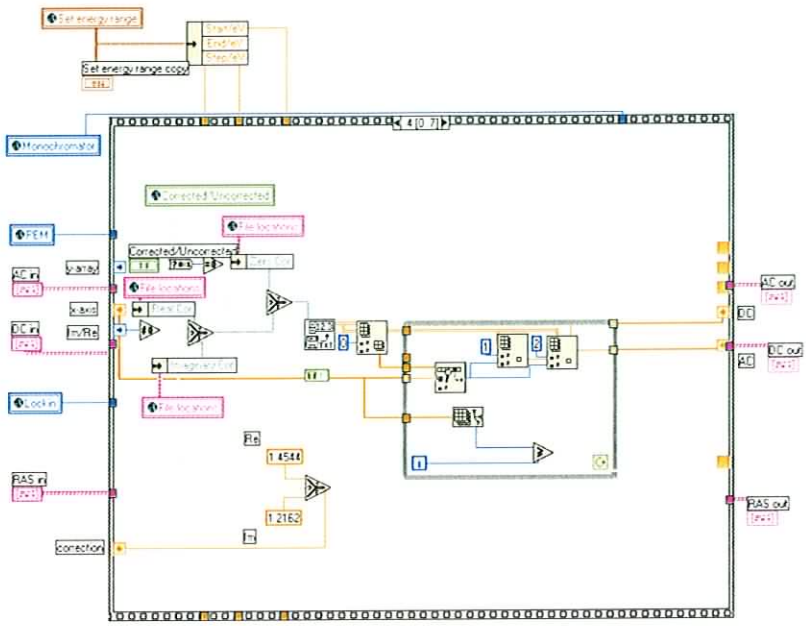

Frame 5/7

This frame presents the user with a dialog box, confirming that the scan can begin. This gives time for any last minute experimental adjustments

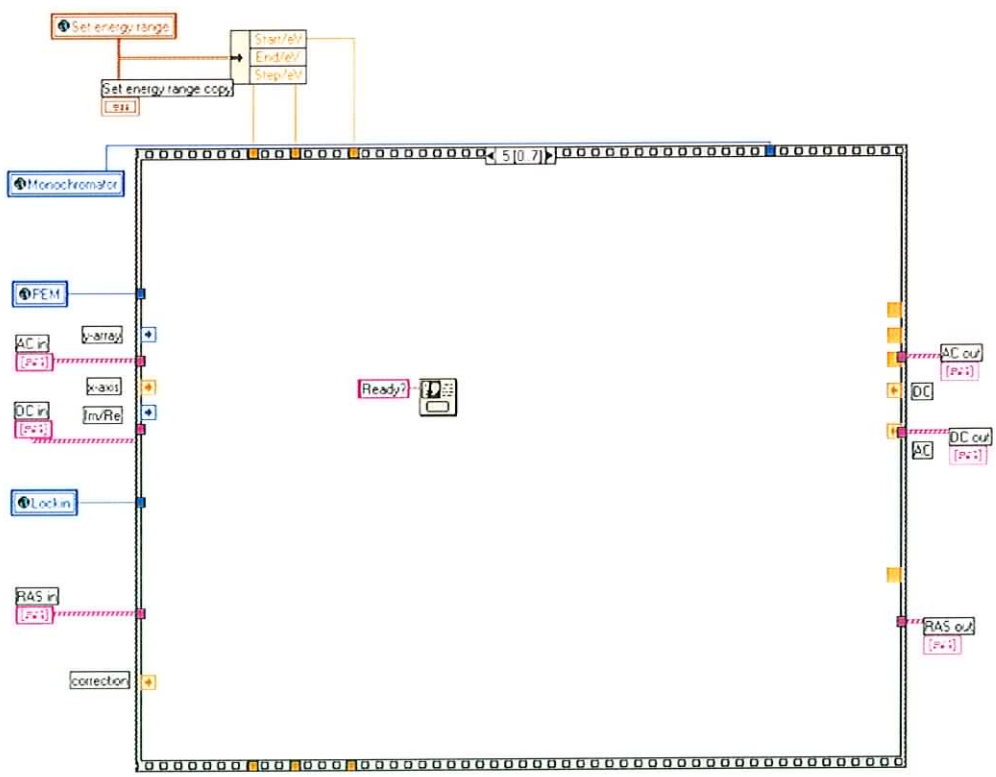

Frame 6/7

This frame contains the main data gathering section of the program. It is contained in a sequence structure within a while loop, which executes as long as the current photon energy is less that the final energy value.

The frames of this sequence structure will be shown individually and explained. Frame 0/5 sets the PM tube voltage, and therefore its gain, to a value determined by the 'Photomultiplier Voltage' variable.

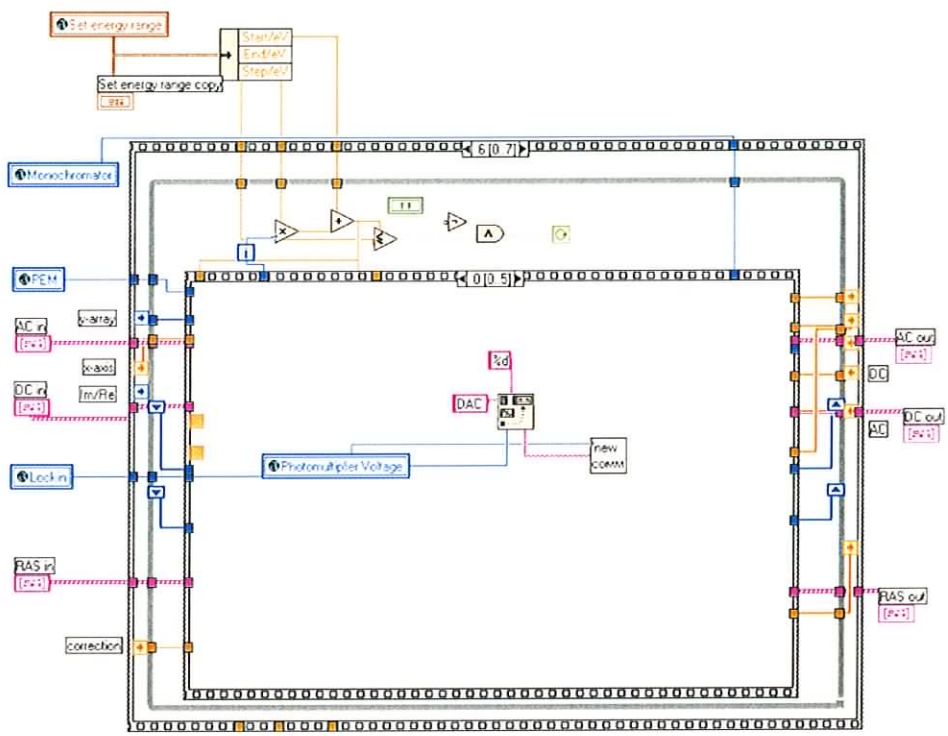

Frame 6/7, SubFrame 1/5

This sets the PEM's wavelength of peak retardation. On the first loop increment, this has already been set and this frame will have no effect.

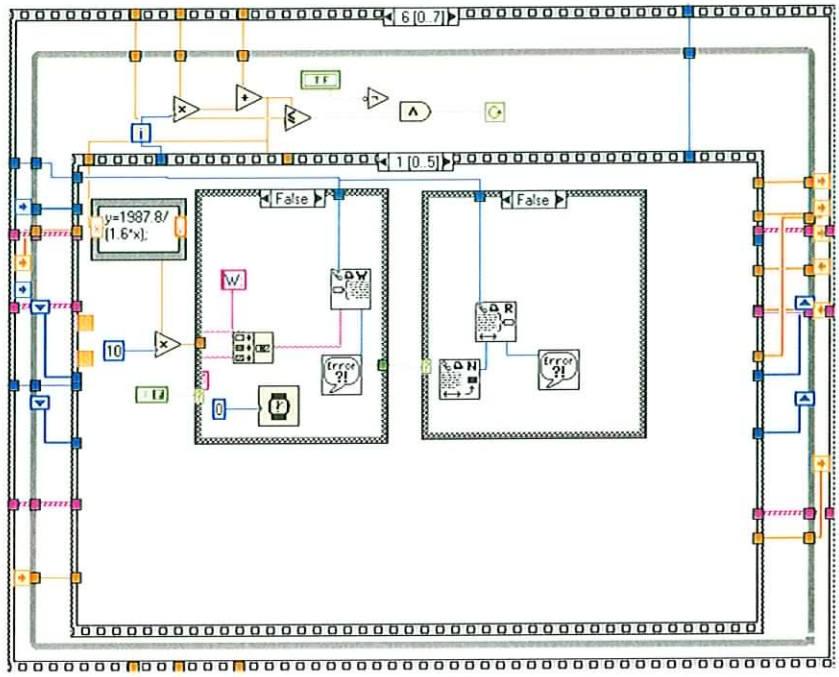

Frame 6/7, SubFrame 2/5

This sets the monochromator photon energy. As with frame 2/5, on the first iteration this has no effect.

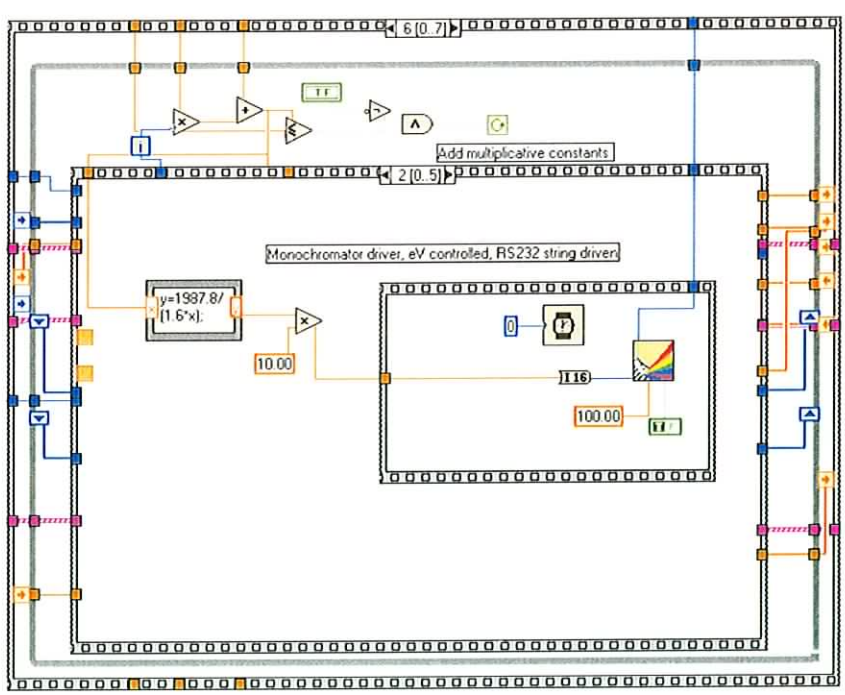

Frame 6/7, SubFrame 3/5

This sends the 'mag' command to the lock-in amplifier, which reads the magnitude of the AC signal and sends it to a sequence local for later use.

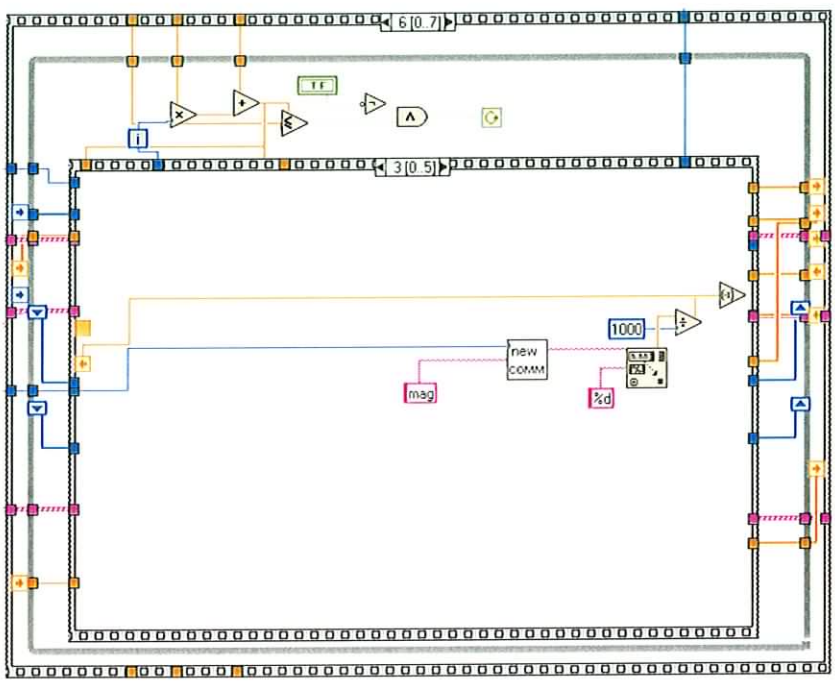

Frame 6/7, SubFrame 4/5

This sends the 'acd1' command to the lock-in, which reads the DC voltage at the first analogue to digital converter (ADC). This is again sent to a sequence local.

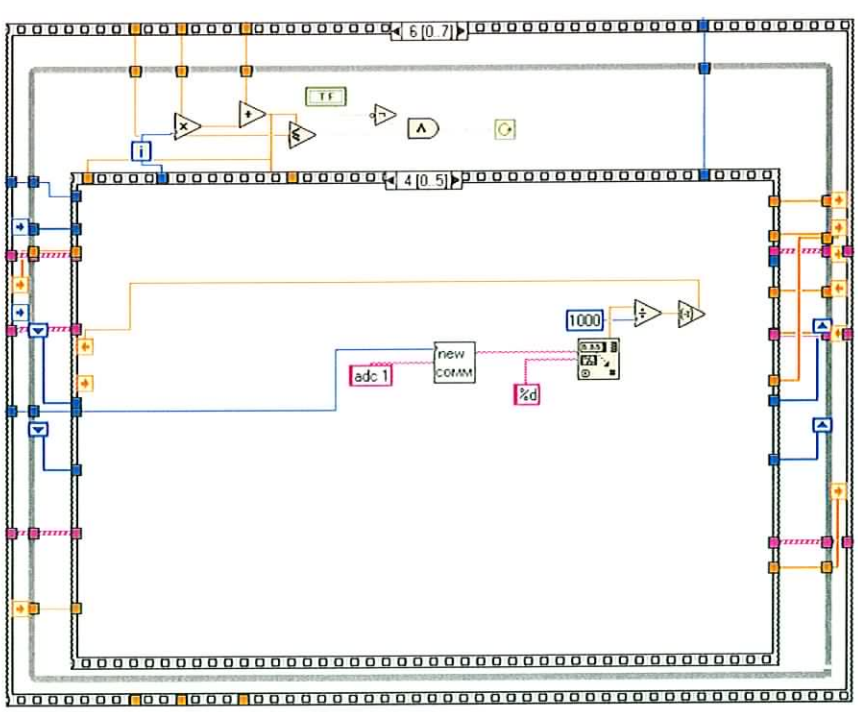

Frame 6/7, SubFrame 5/5

This frame takes the 'AC' and 'DC' values from the sequence locals, subtracts the correction, which will again be zero if no correction is required, and divides the 'AC' by the 'DC' to obtain the 'RAS value. The 'AC', 'DC' and 'RAS' values are graphed on screen against photon energy in the graphical outputs 'AC signal', 'DC signal' and 'RAS signal' respectively.

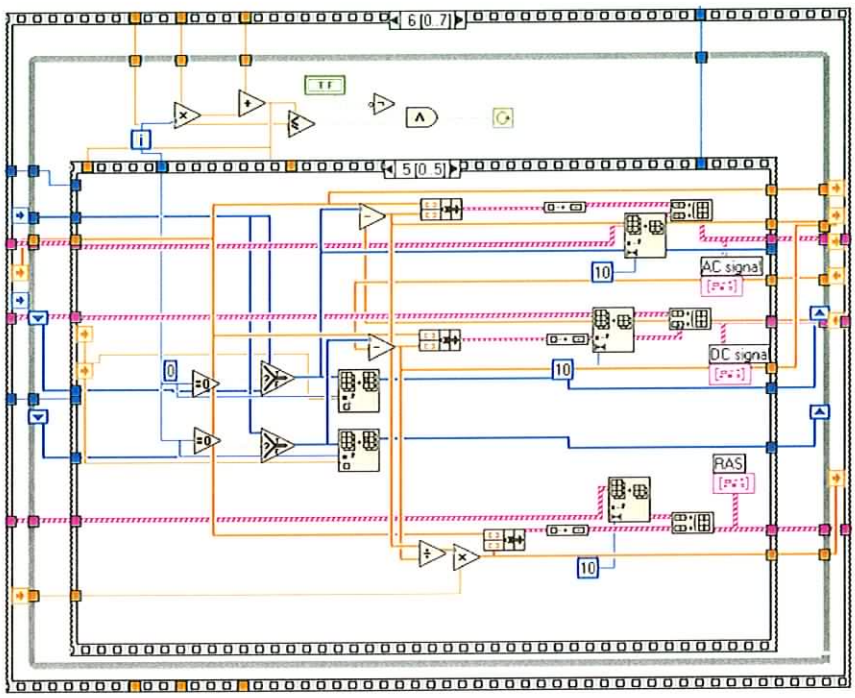

Frame 7/7

This frame asks the user to save the collected data as an ASCII file.

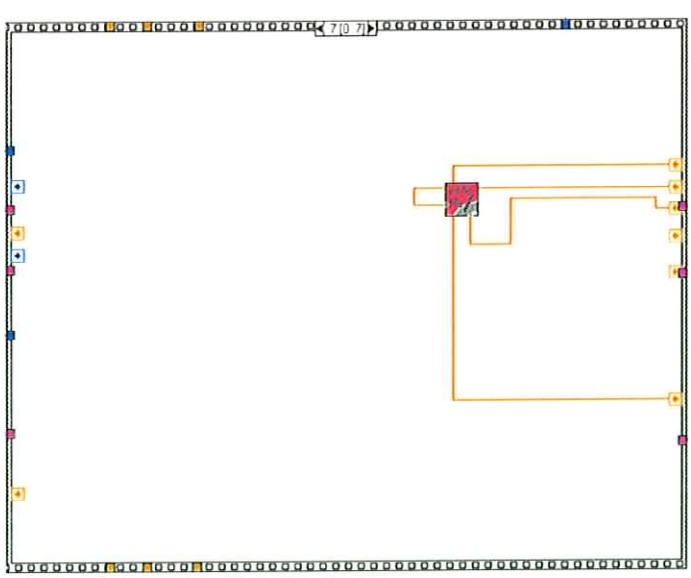

Monochromator Sub VI

The 'monochromator' sub VI is a driver that controls communication between the computer and the monochromator. It is encased within a case structure. The 'False' case contains a more general routing for communicating with the monochromator which is not shown. It cannot be accessed during the programs normal use and is intended for diagnosing problems only.

Frame 1

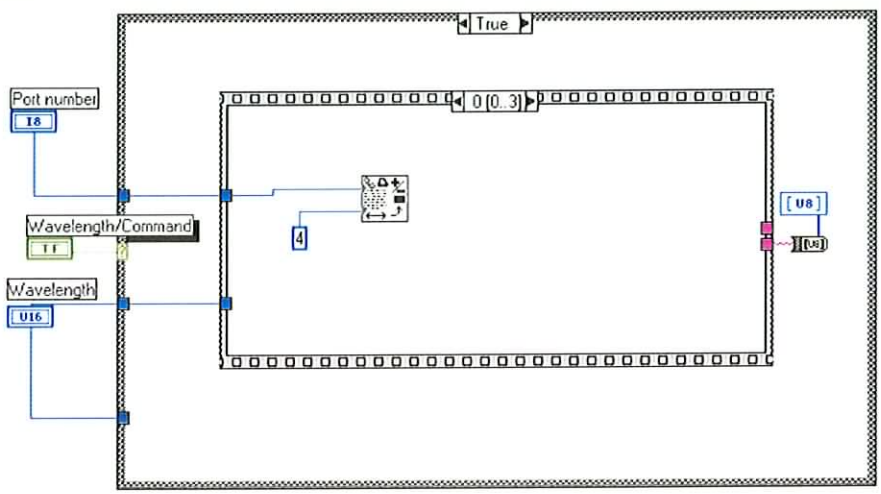

Frame 2

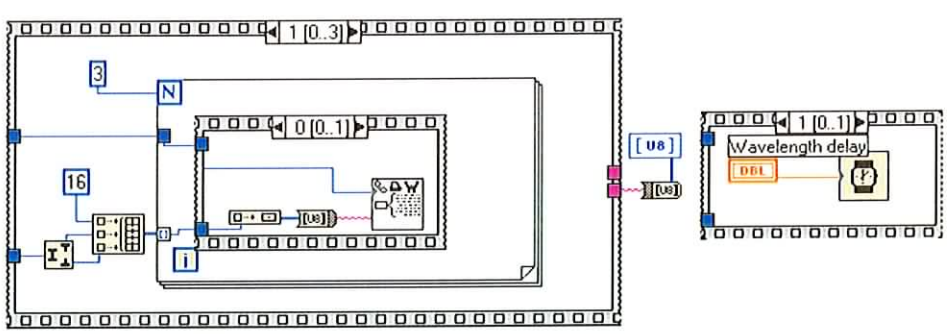

Frame 3

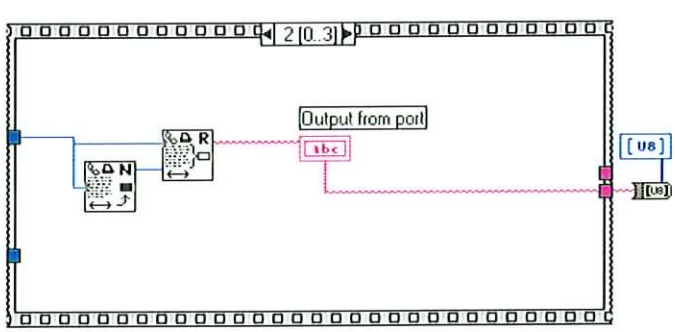

Frame 4

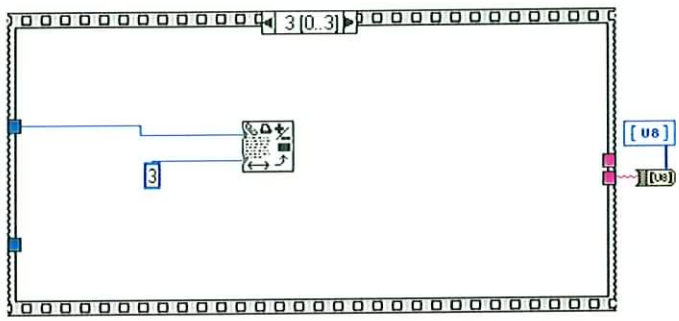

New Comm

This sub vi controls communication with the lock-in amplifier. Some portions of the code are taken from EG&G's original driver, with modifications.

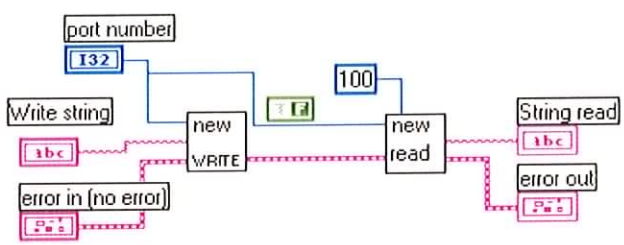

New Write

New write sends strings to the serial port. Any bits remaining at the port are read first, then the string is written. The case labelled "True" is not shown, as it contains only a direct connection for the error structures. This is required to ensure that the program doesn't crash if there is the problem with the port.

Frame 1

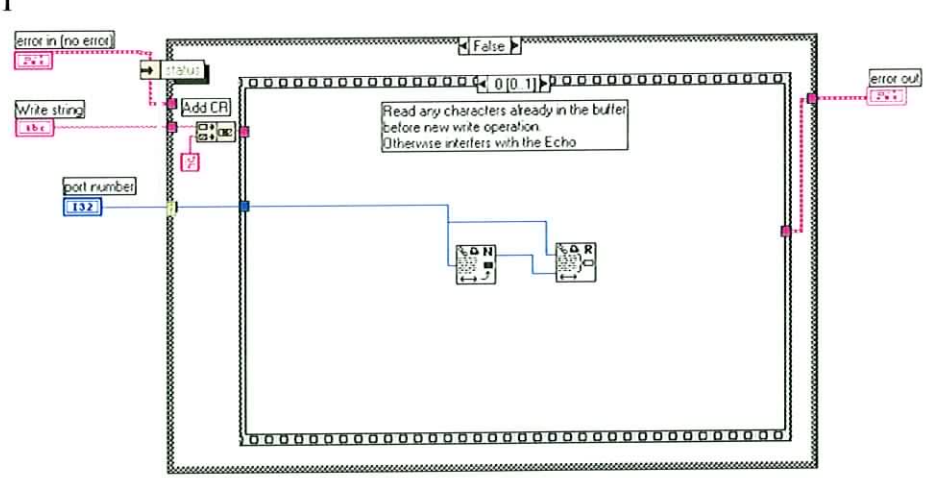

Frame 2

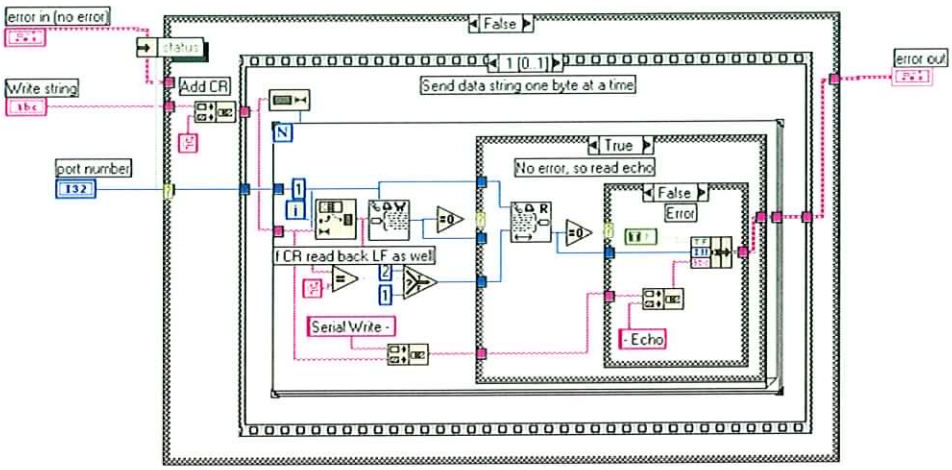

New Read

New Read reads back a string from the serial port. Again the "True" case is omitted.

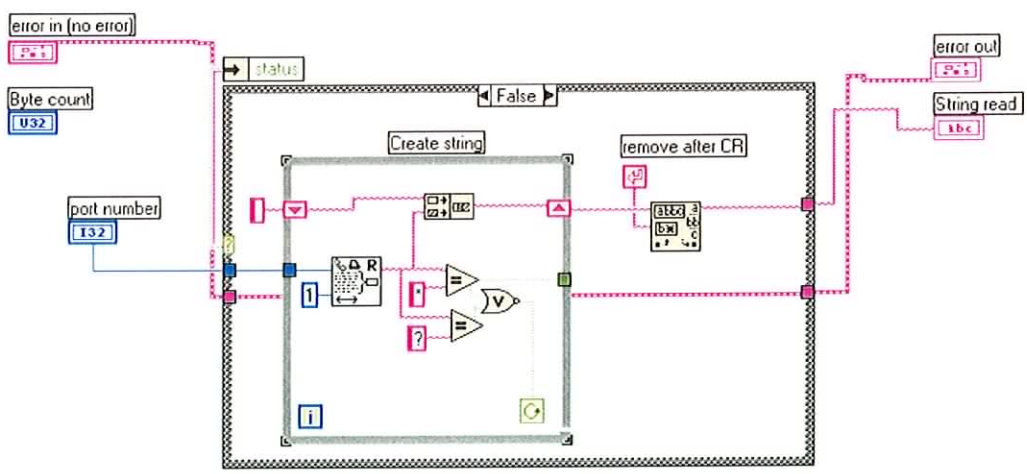

Publications List

Papers

F Pedreschi, JD O'Mahony, P Weightman, JR Power, Evidence of electron confinement in the single-domain, (4x1)-In superstructure on vicinal Si(111)Appl Phys Lett **73**: (15) 2152-2154 1998

F Pedreschi, JD O'Mahony, D. Carty, A. Caffolla, Atomic Resolution STM and STS of the Si(111)-4x1In surface, in preparation

F Pedreschi, JD O'Mahony, JM. Sturm, CFJ Flipse, MFM of Colloidal Iron Particle Films, in preparation

Posters

F Pedreschi, JD O'Mahony, Optical Probes for Monitoring Semiconductor Growth Processes, DIT International Postgraduate Conference, Nov 1998.

F Pedreschi, JD O'Mahony, P Koeller, D. Bruls, CFJ Flipse, Magnetic Properties of Colloidal Metal Nanoparticles, SPM Conference, TU Eindhoven, The Netherlands, November 1999

Presentations

F Pedreschi, Reflectance Anisotropy Spectroscopy and its Applications, Optical Characterisation and Spectroscopy Conference, DIT, Dublin 2002